Automated Construction of Macromodels from Frequency Data for Simulation of Distributed Interconnect Networks

A Thesis
Presented to
The Academic Faculty

by

Sung-Hwan Min

In Partial Fulfillment
of the Requirements for the Degree
Doctor of Philosophy

School of Electrical and Computer Engineering
Georgia Institute of Technology
April 2004

Copyright © 2004 by Sung-Hwan Min

Automated Construction of Macromodels from Frequency Data for Simulation of Distributed Interconnect Networks

Approved by:

Madhavan Swaminathan, Advisor

Sung Kyu Lim

Andrew F. Peterson

C. P. Wong

Abhijit Chatterjee

Date Approved: April 2, 2004

Dedicated to

my father, Byung-Gi Min,

my mother, Hae-Chul Oh,

my father-in-law, Se-Dong Kim

my mother-in-law, Kwang-Sun Choi

my wife, Hyo-Jeong Kim

and

my son, William Kyungjun Min

for their support support and love

ACKNOWLEDGEMENTS

First of all, I would like to thank my advisor, Professor Madhavan Swaminathan, who is an outstanding scientist and mentor, for his advice during my graduate studies. I would like to thank to the Ph.D. committee: Professor Abhijit Chatterjee, Professor Andrew F. Peterson, Professor Sung Kyu Lim, and Professor C. P. Wong. I sincerely appreciate their time and effort in serving on my committee. I would also like to thank my high school teacher, Mr. Nak Myong Sung, and Professor Sung Ho Cho and Professor Hyun Chul Shin during my undergraduate studies at Hanyang University, Ansan, Korea.

I would like to extend special thanks to all current and graduated members of the EPSILON group. Especially, I would like to mention Sidharth Dalmia, Nanju Na, Sungjun Chun, Lixi Wan, Erdem Matoglu, Jifeng Mao, Woopoung Kim, Vinu Govind, Prathap Muthana, Rohan Mandrekar, Jinwoo Choi, Bhyrav Mutnury, Amit Bavisi, Sujeet Vaidya, Tae Hong Kim, Di Qian, Krishna Srinivasan and Souvik Mukherjee.

I would like to thank Dr. Seock Hee Lee at Samsung, Dr. Wendem Beyene at Rambus, Mr. Rahul Shringarpure, Dr. Shubha Kadambe and Dr. Peter Petreof at HRL, and Dr. Gustavsen Bjrn for their support and encouragement for my graduate studies.

I would like to thank my dear friends, Seob-No Lee, Dong-Sung Kim and Ki-Taek Kim for their friendship and encouragement.

Finally, I would like to thank my parents, Byung-Gi Min and Hae-Chul Oh, my parents-in-law, Se-Dong Kim and Kwang-Sun Choi, bothers, Hwan-Gi Min and Sung-Up Min, my wife, Hyo-Jeong Kim, and my boy, William Kyungjun Min for their support, love, and encouragement.

TABLE OF CONTENTS

DEDICATION . . . . . **iii**

ACKNOWLEDGEMENTS . . . . . **iv**

LIST OF TABLES . . . . . **ix**

LIST OF FIGURES . . . . . **x**

CHAPTER I INTRODUCTION **1**

1.1 Macromodels 2

1.2 Types of Macromodels 4

1.2.1 Scalable Macromodels 4

1.2.2 Passive Macromodels 6

1.2.3 Broadband Macromodels 7

1.2.4 Non-linear Macromodels 8

1.3 Properties of Macromodels 9

1.3.1 Real Coefficients 10

1.3.2 Causality 10

1.3.3 Stability 10

1.3.4 Passivity 11

1.4 Issues in the Construction of Macromodels 11

1.4.1 Scalable Macromodels 12

1.4.2 Passive Macromodels 13

1.4.3 Broadband Macromodels 14

1.4.4 Model Order Reduction 16

1.5 Numerical Approximation 18

1.5.1 Least Squares Approximation 18

1.5.2 Vector Fitting 21

1.5.3 Multiport Approximation 22

1.6 Proposed Research and Dissertation Outline 25

CHAPTER II SCALABLE MACROMODELS **31**

2.1 Orthogonal Polynomials 32

2.1.1 Test Case: Power plane pair 36

2.2 Scalable Macromodels 38

2.2.1 Test Case: Power plane pair with two design parameters . . . 39

2.3 Selective Sampling 41

2.3.1 Test Case 1: Frequency response of a power plane pair 43

2.3.2 Test Case 2: Power plane pair with two design parameters . . 45

2.4 Embedded Inductors 47

2.4.1 Scalable Macromodels from Electromagnetic Simulation . . . 49

2.4.2 Scalable Macromodels from Measurements 52

2.5 Summary 59

CHAPTER III PASSIVE MACROMODELS **61**

3.1 Filters 61

3.2 Properties of Filters 63

3.3 Multiport Passivity Formulae 65

3.4 Enforcing Passivity 68

3.5 Discussion of Multiport Passivity Formulae 69

3.5.1 Residue Matrix $[\eta]$ 69

3.5.2 Overlapping Real Poles 73

3.5.3 Limitations of Multiport Passivity Formulae 75

3.6 Network Synthesis 75

3.7 Summary 77

CHAPTER IV BROADBAND MACROMODELS **80**

4.1 Ill-conditioned Matrix Problem 80

4.2 Limitations of Least Squares Approximation 81

4.2.1 Low Order System 82

4.2.2 High Order System 83

4.3 Band Division 87
4.4 Band Interactions 90
4.4.1 Selector 91
4.4.2 Subband Reordering 94
4.4.3 Subband Dilation 95
4.4.4 Pole Replacement 95
4.5 Illustrative Example 99
4.6 Test Cases 101
4.6.1 Test Case 1: Frequency response from a known transfer function (low-order system) 101
4.6.2 Test Case 2: Frequency response from a known transfer function (high-order system) 105
4.6.3 Test Case 3: One-port lossy transmission line 106
4.7 Automated Construction 107
4.8 Multiport Construction 109
4.9 Model Order Reduction 110
4.9.1 Test Case: Frequency response from a power distribution network 111
4.10 Broadband Efficient Macromodeling Program 113
4.11 Summary 114
CHAPTER V EXAMPLES AND TEST CASES 117
5.1 Test Case 1: Four-port lossy coupled transmission line 117
5.2 Test Case 2: Four-port transmission line data from measurement . . 121
5.3 Test Case 3: Four-port power plane pair with decoupling capacitors 123
5.4 Test Case 4: Power distribution network from Rambus 128
5.5 Test Case 5: Fourteen-port power distribution network for INC board (Intelligent Network Communicator) from the Packaging Research Center 136
5.6 Test Case 6: 32-bit bus from HRL 140
5.7 Summary 144

CHAPTER VI CONCLUSION AND FUTURE WORK **145**

VITA **161**

LIST OF TABLES

Table 1 Recurrence relations of orthogonal polynomials [65] 34

Table 2 Embedded rectangular spiral inductors 51

Table 3 Embedded circular spiral inductors 57

Table 4 Poles and residues of a known transfer function - Low order system 82

Table 5 Poles and residues of a known transfer function - High order system 86

Table 6 Without using selectors 102

Table 7 Using selectors (before) 105

Table 8 Using selectors (after) 105

Table 9 Output of model order reduction (MOR) 111

Table 10 Location of 14 ports 139

LIST OF FIGURES

Figure 1 Passive devices 2

Figure 2 Macromodel 3

Figure 3 Embedded spiral inductors having many design parameters 5

Figure 4 Cross section of the inductor on a laminate substrate 6

Figure 5 Violation of passivity for an interconnect [32] 7

Figure 6 Frequency response of a lossy coupled transmission line 8

Figure 7 Non-linear macromodel 9

Figure 8 Passivity violations: (a) indirect compensation [49] and (b) direct compensation [46] 15

Figure 9 Minimum eigenvalue tracking method vs. the order NS 17

Figure 10 Frequency response of the power series expansion [38] 33

Figure 11 Frequency responses of orthogonal polynomials: (a) Legendre polynomials, (b) Chebyshev I polynomials and (c) Chebyshev II polynomials 35

Figure 12 Power plane pair 36

Figure 13 Power series expansion and orthogonal polynomials 37

Figure 14 Comparison between the original response and the response of Chebyshev II polynomials 38

Figure 15 Frequency response of a power plain pair with two design parameters 41

Figure 16 Performance of the scalable macromodel having width of 1.750in and thickness of 1.8mil 42

Figure 17 Selective sampling 43

Figure 18 Frequency samples of two groups $G1$ and $G2$ 44

Figure 19 Maximum deviation between two frequency responses vs. the number of iterations 45

Figure 20 Comparison between the original response and the response of rational functions 46

Figure 21 Maximum deviation between two frequency responses vs. the number of iterations 47

Figure 22 Frequency response of power plane pair with two design parameters 48

Figure 23 Performance of the scalable macromodel having width=1.750in and thickness=1.8mil 48

Figure 24 Embedded rectangular spiral inductor: (a) cross section and (b) top view 50

Figure 25 Maximum deviation between two frequency responses vs. number of iterations 52

Figure 26 Frequency response of embedded inductors with two design parameters 53

Figure 27 Performance of the scalable macromodel having inner diameter of 60mil and number of turns of 2 53

Figure 28 Cross-section of the test vehicle 54

Figure 29 Top view of the inductor 56

Figure 30 Maximum deviation between two frequency responses vs. number of iterations 58

Figure 31 Frequency response of embedded inductors with two design parameters 58

Figure 32 Performance of the scalable macromodel having inner diameter of 64mil and number of turns of 1 59

Figure 33 Frequency response for a low pass filter: (a) real part of a real pole for a fixed residue and (b) real part of a real residue for a fixed pole 64

Figure 34 Frequency response for a band pass filter: (a) varying p_r for fixed coefficients p_i, α, β, (b) varying p_i for fixed coefficients p_r, α, β, (b) varying α for fixed coefficients β, p_r, p_i, and (b) varying β for fixed coefficients α, p_r, p_i 65

Figure 35 Enforcing passivity using multiport passivity formulae 69

Figure 36 Unstable circuit 70

Figure 37 Values of the electrical elements 76

Figure 38 Electrical network configurations for the macromodel using admittance parameters 77

Figure 39 (a) Self-admittance YAA and (b) trans-admittance YBA realizations 78

Figure 40 Performance of LSA for $LP = 1$ and $BP = 2$: (a) the RMS error of the deviation vs. the order NS and (b) the original frequency response (solid line) of the known transfer function, the frequency response (dotted line) of the rational function of order $NS = 4$ and $DS = 5$, and the deviation (dashed line) 84

Figure 41 Performance of LSA for $LP = 1$ and $BP = 2$: (a) comparison of pole distributions and (b) comparison of residue distributions . . . 85

Figure 42 Performance of LSA for $LP = 3$ and $BP = 8$: (a) the root-mean-square error of the deviation vs. the order NS and (b) the original frequency response (solid line) of the known transfer function, the frequency response (dotted line) of the rational function of the order NS of 14, and the deviation (dashed line) 88

Figure 43 Performance of LSA for $LP = 3$ and $BP = 8$: (a) comparison of pole distributions and (b) comparison of residue distributions . . . 89

Figure 44 Band division: (a) 10 uniform subbands and (b) 5 non-uniform subbands (subbands 1, 2, 3: non-overlapping, subbands 4, 5: overlapping) 90

Figure 45 (a) Frequency subband and (b) selectors 93

Figure 46 Subband reordering 95

Figure 47 Subband dilation 96

Figure 48 Pole replacement 97

Figure 49 Illustration of the band division and subband reordering methods . 99

Figure 50 The magnitude comparison between the original data and the response of macromodels without using selectors (Solid line: Original, Dashed line: Macromodels, Dotted line: Deviation): (a) the first subband, (b) the first and second subbands and (c) the entire frequency band 103

Figure 51 The magnitude comparison between the original data and the response of macromodels with filters (solid: original, dash: macromodel, dot: deviation): (a) the first subband, (b) the first and second subbands and (c) the entire frequency band 104

Figure 52 Performance of LSA for $LP = 3$ and $BP = 8$: the original frequency response (solid line) of the known transfer function, the frequency response (dotted line) of the macromodel, and the deviation (dashed line) 106

Figure 53 Passive macromodel without using the pole replacement method ($NS = 4$ and $DS = 5$ in each subband, number of iterations of the local pole replacement method = 0, number of iterations of the global pole replacement method = 0, number of complex conjugate poles = 30 and number of real poles = 1) 107

Figure 54 Passive macromodel using the pole replacement method ($NS = 4$ and $DS = 5$ in each subband, number of iterations of the local pole replacement method = 50, number of iterations of the global pole replacement method = 100, number of complex conjugate poles = 66 and number of real poles = 4) 108

Figure 55 A flow chart for detecting the subbands 109

Figure 56 Frequency response after removing spurious filters: original data (bold solid), response of the macromodel with 0 percent MOR (solid), response of the macromodel with 1 percent MOR (dot), response of the macromodel with 5 percent MOR (dash) and response of the macromodel with 10 percent MOR (dash dot) 112

Figure 57 Circuit simulated 113

Figure 58 Time-domain simulation 114

Figure 59 Flow chart of BEMP 115

Figure 60 Lossy coupled transmission line 118

Figure 61 Comparison of the real part of Y14 (admittance) 118

Figure 62 Comparison of the imaginary part of Y14 (admittance) 119

Figure 63 Comparison of four eigenvalues vs. frequency between original data and the frequency response calculated from the macromodel 120

Figure 64 Circuit simulated 120

Figure 65 Time-domain simulation of the non-passive macromodel 121

Figure 66 Time-domain comparison between a lossy coupled transmission line and the passive macromodel 122

Figure 67 Comparison of real part real of admittance parameter Y11 122

Figure 68 Comparison of imaginary part of admittance parameter Y12 123

Figure 69 Circuit simulated 124

Figure 70 Time-domain waveform 124

Figure 71 A power plane pair with decoupling capacitors 125

Figure 72 Comparison of real part of admittance parameters for a power plane with decoupling capacitors 126

Figure 73 Comparison of imaginary part of admittance parameters for a power plane with decoupling capacitors 126

Figure 74 Circuit simulated 127

Figure 75 Time-domain simulation of a power plane pair with decoupling capacitors 127

Figure 76 Yellowstone test vehicle from Rambus 128

Figure 77 Cross section of the board 129

Figure 78 Top view of the test vehicle 130

Figure 79 Comparison of admittance parameters: (a) real of Y22, (b) imaginary of Y22, (c) real of Y23 and (d) imaginary of Y23 132

Figure 80 Admittance parameters (Y11, Y12, Y22) generated from the constructed macromodel: (a) from DC to 10MHz and (b) from 5GHz to 15GHz 133

Figure 81 Comparison of three eigenvalues vs. frequency between original data and the frequency response calculated from the macromodel 134

Figure 82 Circuit simulated 135

Figure 83 Time-domain simulation for measuring power supply noise 135

Figure 84 INC board from Packaging Research Center 136

Figure 85 Cross section of the INC board 137

Figure 86 Layout of the layers (a) signal layer, (b) ground plane layer and (c) power plane layer 138

Figure 87 Comparison of admittance parameters: (a) magnitude of Y(1,1), (b) magnitude of Y(1,12), (c) magnitude of Y(12,1) and (d) magnitude of Y(12,12) 139

Figure 88 Time-domain simulation for evaluating the performance of the power distribution network with decoupling capacitors and embedded capacitors: (a) voltage at port 2 and (b) voltage at port 6 141

Figure 89 (a) Layout of Delta-Sigma modulator from HRL and (b) layout of 32-bit bus 142

Figure 90 Comparison of admittance parameter Y(1,9) 143

Figure 91 Circuit simulated 143

Figure 92 Crosstalk between ports 1 and 9 144

Figure 93 Evolution of BEMP 147

CHAPTER I

INTRODUCTION

The rapidly changing world is in constant pursuit of portable, cheap, power efficient, reliable, high-speed analog/digital electronics, which requires not only higher-level integration of active and passive devices but also faster clock speed in the system. Using deep sub-micron and multilayer packaging technologies, the feature size of both transistors and interconnects has been reduced up to the material and process limitations of integration [1]-[8]. At the same time, the clock speed has been increased well above the multi-GHz frequency range in order to perform many functions within a small time interval.

As the complexity of interconnects and packages increases and the rise and fall time of the signal decreases, the previously neglected electromagnetic effects of distributed passive devices, which lead to signal and power integrity issues, are becoming an important factor in determining the performance of gigahertz systems [9]-[12]. Some examples of distributed passive devices are inductors, capacitors, lossy coupled transmission lines, and power distribution networks, as shown in Figure 1.

The electromagnetic behavior of interconnects and passive devices can be extracted using an electromagnetic simulation or from measurements. This behavior is available as frequency dependent data that represent scattering, admittance or impedance parameters. This information can be represented as a black box, which captures the behavior of the passive structure at the input/output ports. This black box representation is called a macromodel in this dissertation. For successful integration of the electromagnetic behavior of distributed networks into circuit simulators for design and analysis of gigahertz systems, it is important to investigate the properties

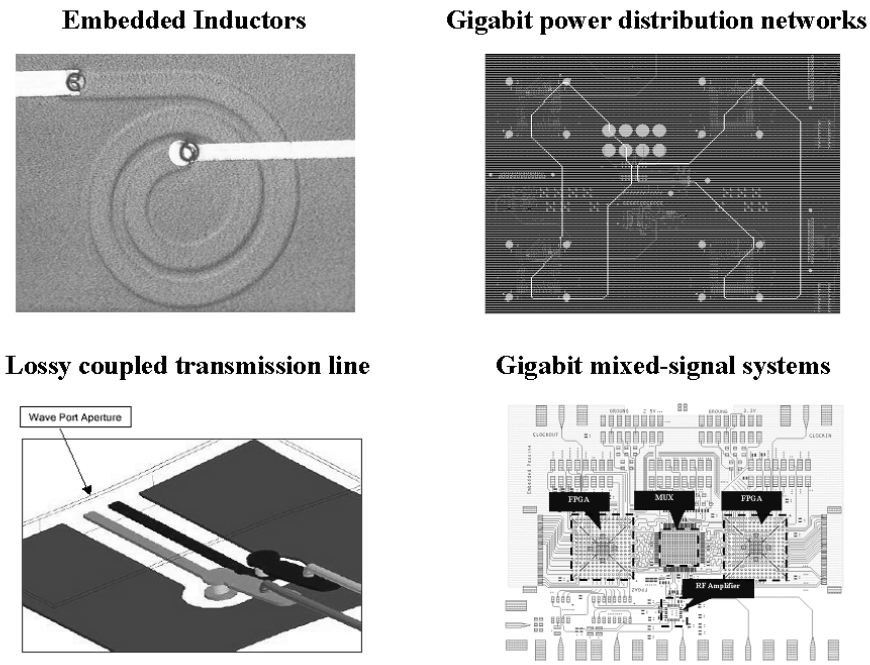

Figure 1: Passive devices

of the macromodel and to propose efficient methods for representing the frequency response of distributed networks as a macromodel, which is the focus of this dissertation.

1.1 Macromodels

There has been an increasing demand for integrating the electromagnetic behavior of passive structures into conventional computer-aided design (CAD) tools so that designers can take into account the electromagnetic effects during the design and analysis of multi-GHz electronic systems [13]-[15]. The CAD tools include non-linear circuit simulators, which solve the modified nodal analysis (MNA) matrix equations [16], or electromagnetic simulators, which solve Maxwell's equations [17]. Two major methodologies for integrating the electromagnetic behavior into CAD tools have been studied by various authors in the past [18], [19]. One methodology is to integrate lumped and/or non-linear circuits into electromagnetic simulators based on the Finite-Difference Time-Domain (FDTD) method [20], Transmission Line Matrix

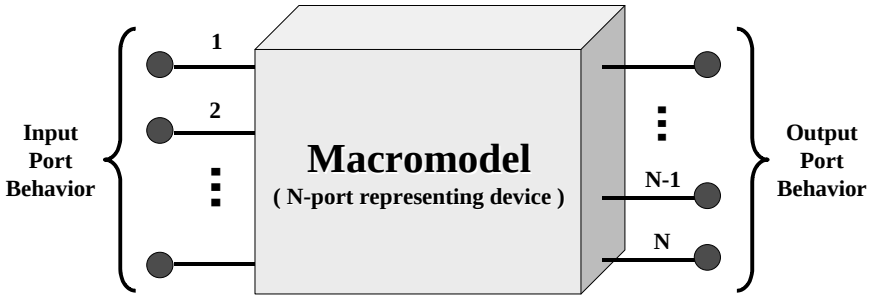

Figure 2: Macromodel

(TLM) method [21], or Partial Element Equivalent Circuit (PEEC) method [22]. This requires solving a large number of unknowns, but provides detailed information of the electromagnetic behavior of the structure. The other prominent methodology is to integrate the electromagnetic behavior of passive devices at the input/output ports into circuit simulators [23]-[47]. This black box representation that captures the electromagnetic behavior at the input/output ports is called a macromodel, as shown in Figure 2. The macromodel can be a two port or a multiport device, as shown in Figure 2.

The macromodel can be constructed using two methods. One method is to construct the macromodel from the moments that are the characteristics of the circuit. In [23]-[32], explicit or implicit moment-matching techniques have been used to construct the macromodel by generating and matching the moments using Pade approximation. The other method is to capture the frequency dependent data using a macromodel after extracting the port behavior of the circuit either from an electromagnetic simulator or from measurements. In [33]-[47], the macromodel has been constructed by capturing measured or simulated frequency data using least squares approximation [33]-[41] and vector fitting [42]-[47]. In either case, the purpose of the macromodel is to replace the electromagnetic behavior of the circuit with a reduced equivalent model that not only preserves the characteristics of the original passive circuit at the input/output ports but also captures the electromagnetic behavior as

accurately as possible.

1.2 Types of Macromodels

Based on the application, the macromodel can be categorized as follows: 1) Scalable macromodels for implementing design libraries, 2) Passive macromodels for time-domain simulation of circuits, 3) Broadband macromodels that capture the dynamic response of structures over a broad frequency range, and 4) Non-linear macromodels for the representation of active devices.

1.2.1 Scalable Macromodels

The demand for portable wireless devices requires higher-levels of integration at low cost. This has led to the integration of electrical components, such as resistors, capacitors, and inductors, into the silicon or packaging substrate [1]. Off-chip components currently being used require a large amount of real estate and consume large levels of electrical power with high manufacturing cost. On the other hand, embedded passive components in multilayer configurations reduce the physical size of components, reduce the manufacturing cost, and provide a good alternative to discrete surface mount components for high-density integration. Hence, research programs are underway for replacing off-chip passive components with embedded passive components using multilayer technologies at the chip, package, and board levels [56], [57], [58]. Specifically, embedded inductors have been investigated for achieving useful values of inductance and quality factor by changing the layout dimension and topology using multilayer technologies [52], [53], [58]. As an example, Figure 3 shows the top view of an one-port embedded spiral inductor with design parameters such as the conductor width (W), conductor spacing (S), inner diameter distance (D), width of bridge (B), via diameter distance (V), and number of turns (N).

In addition, Figure 4 shows the cross-section of the embedded inductor with additional design and material parameters such as the dielectric thickness (T), copper

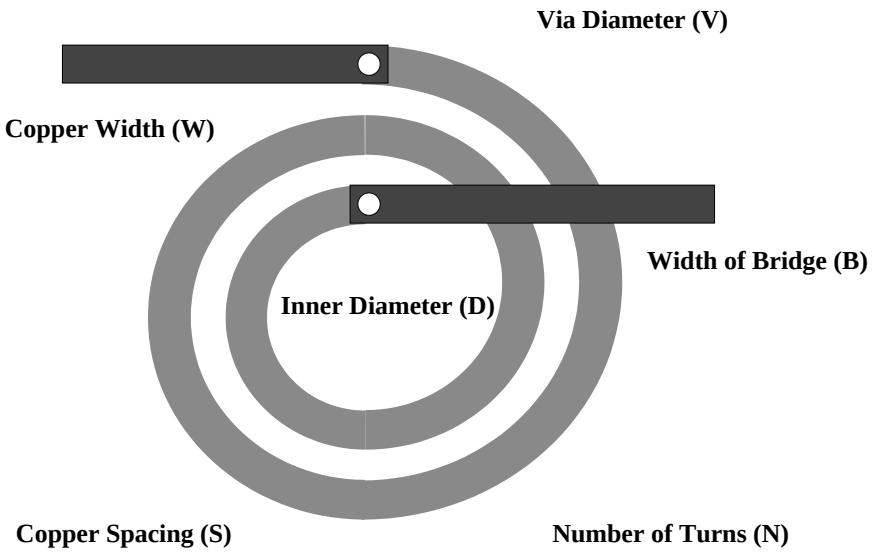

Figure 3: Embedded spiral inductors having many design parameters

thickness (C), dielectric constant (E), and loss tangent (L). These additional parameters are varied depending on the multilayer packging technology used. In Figure 4, the spiral embedded inductor is on the first layer and the bridge connecting the inner port to electrical ground is on the second layer. The electrical response of the inductor shown in Figures 3 and 4 is dictated by the parasitics of the structure. Hence, an electromagnetic simulator is required for extracting the frequency response of the structure.

Often times, RF designers need to optimize the layout of the inductor and choose the materials for different applications. This can be a cumbersome task due to the complexity of the structure, leading to long simulation times based on the grid size used. Instead, the structure can be parameterized by mapping the parameters to the electrical response at the input/output ports. This is called a scalable macromodel since the electrical response can be obtained by either scaling the physical dimensions of the device or varying the electrical parameters of the materials used. The scalable macromodel is useful in developing design libraries for RF passive devices.

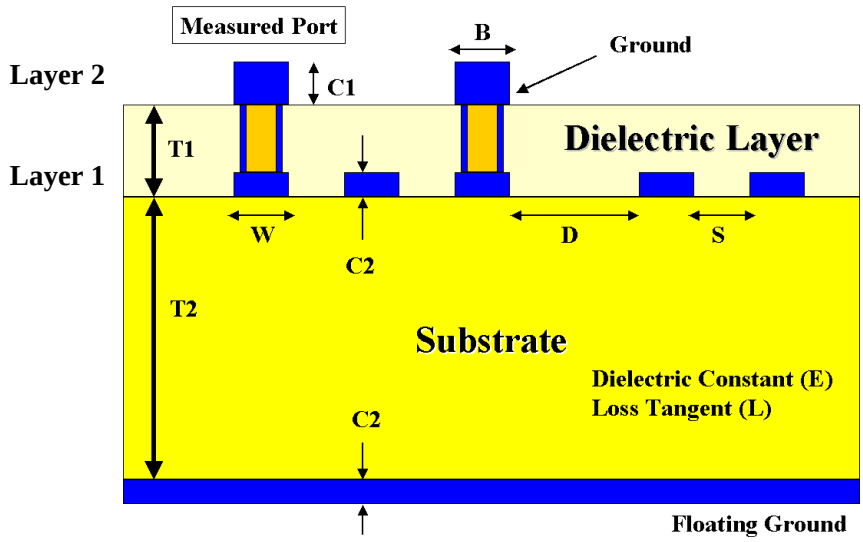

Figure 4: Cross section of the inductor on a laminate substrate

1.2.2 Passive Macromodels

Unlike scalable macromodels, the macromodel that enables the integration of the frequency response of passive devices or interconnect networks into time-domain simulators such as SPICE (Simulation Program with Integrated Circuit Emphasis) is called a passive macromodel in this dissertation. Hence, passive macromodels provide for frequency to time translation within the framework of a time-domain simulator.

Since distributed interconnect networks are inherently passive, the macromodel has to satisfy the stability and passivity conditions for enabling time-domain simulation. If a macromodel does not satisfy the stability and passivity conditions, the macromodel combined with a stable circuit can generate an unstable time-domain response and can behave as an amplifier or an oscillator during time-domain simulation [19], [32], [46]. In Figure 5, when a two-port non-passive macromodel of an interconnect was terminated with a 50 Ω resistor, an oscillating time-domain waveform was produced during transient simulation in SPICE [32], which is non-physical. Hence, the macromodel needs to satisfy the stability and passivity conditions. It is

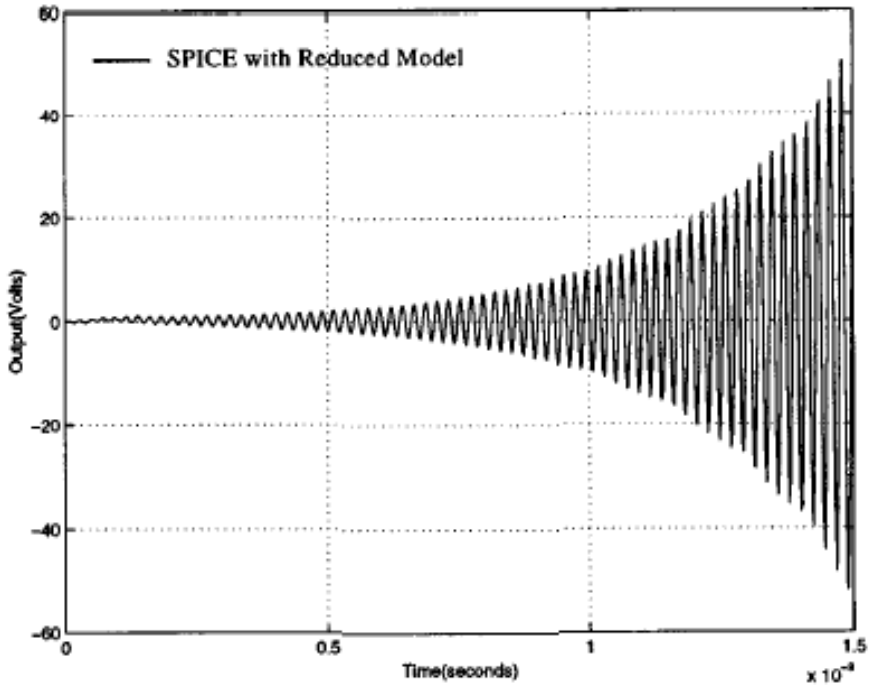

Figure 5: Violation of passivity for an interconnect [32]

important to note that the scalable macromodel can be embedded into time-domain simulators by parameterizing the passive macromodel.

In this dissertation, the passive macromodel is limited to low order systems to differentiate it from the broadband macromodel, which is the topic of the next section.

1.2.3 Broadband Macromodels

Realistic distributed interconnect networks operating over a broad frequency range often contain hundreds of resonant peaks and the amplitude variation of the frequency response can be large. As an example, Figure 6 shows the admittance parameter (Y14) of a lossy coupled transmission line, which is representative of a distributed network over a broad frequency range. The representation of the frequency response in Figure 6 requires a high order macromodel with hundreds of resonant poles. This can be a cumbersome task due to the large amplitude variation and the broad frequency range to be covered, and can lead to numerical problems. Hence, ensuring accuracy along

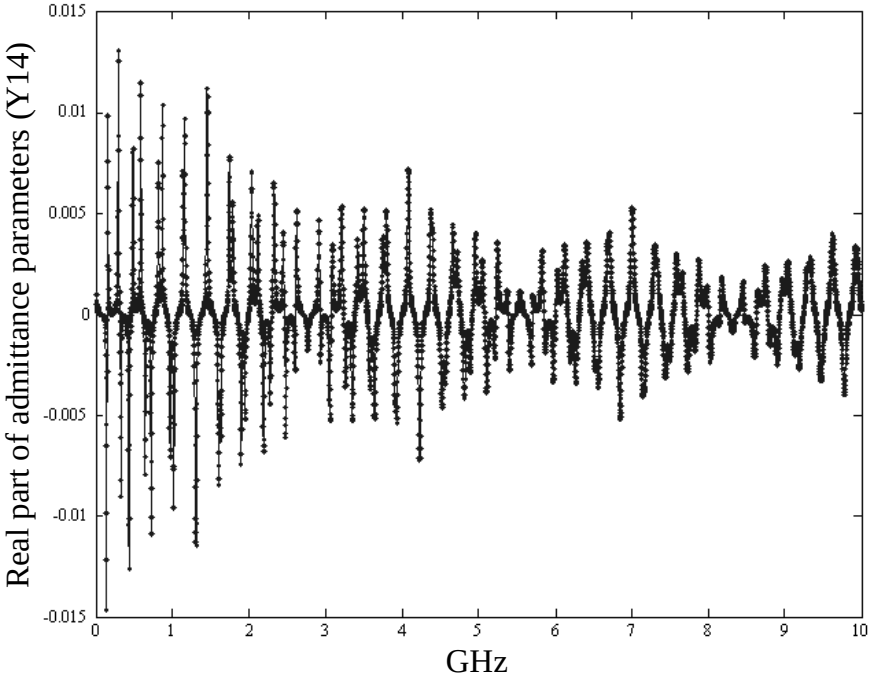

Figure 6: Frequency response of a lossy coupled transmission line

with stability and passivity over a broad frequency range becomes a challenge.

In this dissertation, the broadband macromodel is a passive macromodel for high order systems. This macromodel is suitable for representing the parasitic behavior of distributed interconnect networks in time-domain simulators for passive devices supporting fast rise and fall time.

1.2.4 Non-linear Macromodels

Simulation of interconnect networks requires accurate models of non-linear devices at the input/output ports. Since simulation of transistor level circuits can be cumbersome, the non-linear circuits can be represented using a macromodel. This is shown in Figure 7, where the static and dynamic relationship between the output current and output voltage can be captured using a non-linear macromodel [70]. The non-linear macromodel is a black box representation of the transistor circuit, as shown in Figure 7. Though the non-linear macromodel is important for the simulation of accurate

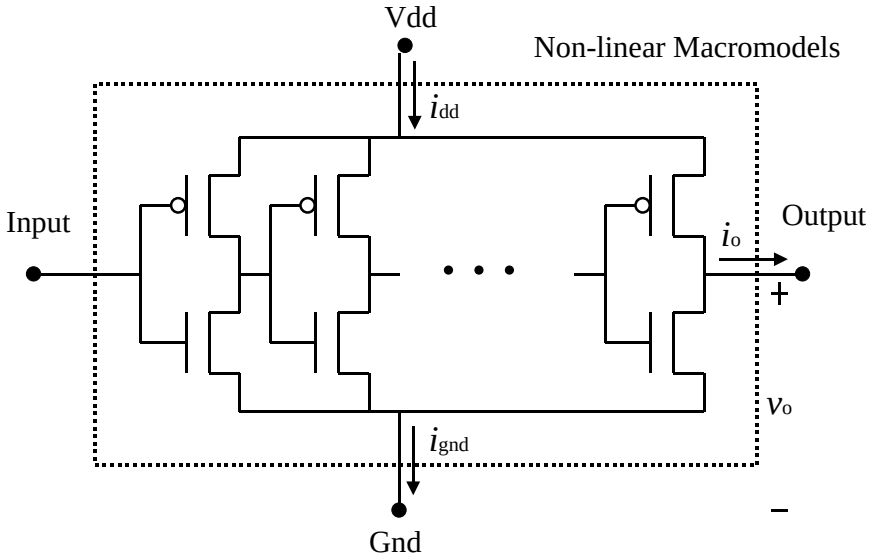

Figure 7: Non-linear macromodel

waveforms on interconnect structures, this dissertation is limited to the generation of macromodels for passive devices.

1.3 Properties of Macromodels

The basis for the construction of the macromodel is a rational function, which is defined by Webster's dictionary as "a quotient of two polynomial functions", where the polynomial is defined as "a mathematical expression of one or more algebraic terms, each of which consists of a constant multiplied by one or more variables raised to a nonnegative integral power." Using the rational function, the frequency response $H(s)$ of any linear time-invariant passive network can be represented as:

$$H(s) = \frac{\sum_{ns=0}^{NS} a_{ns} s^{ns}}{\sum_{ds=0}^{DS} b_{ds} s^{ds}} \tag{1.1}$$

where $s = j\omega$, ω is the angular frequency in radians per second. In Equation (1.1), $H(s)$ can be scattering, admittance, or impedance parameters generated from an electromagnetic simulation or measurements. The goal of solving Equation (1.1) is to represent the frequency response $H(s)$ as a rational function by computing the orders

NS and DS and the coefficients a_{ns} and b_{ds} of the numerator and denominator, respectively.

1.3.1 Real Coefficients

Since any time-domain waveform $f(t)$ is real, constraints need to be enforced on the coefficients of the rational function. If the Fourier transform of $f(t)$ is defined as $F(s)$, the Fourier transform of $f^*(t)$ is $F^*(-s)$, where $*$ is the complex conjugate operator [67]. Since $f(t)$ is real, $F(s) = F^*(-s)$. For enabling time-domain simulation, the rational function therefore has to satisfy the constraint $H(s) = H^*(-s)$ in Equation (1.1), which requires real coefficients for the rational function.

1.3.2 Causality

The causality condition requires that if a physical device having two ports has a finite length, the signal launched at one port appears at the other port after a finite time interval. If the causality condition is violated, a spurious time-domain waveform can result prior to the finite travel time of the signal. As the rise and fall time of the signal decreases, the electrical length of interconnects becomes comparable to the wavelength at the maximum operating frequency of the device [9]. Therefore, delay and causality become important during time-domain simulation since spurious glitches prior to signal arrival can cause the false transition of the circuit.

1.3.3 Stability

The stability condition requires that for a stable system, the output response be bounded for a bounded input excitation [59]. Hence, the rational function representing a stable system has to satisfy the following stability constraints: 1) the poles lie on the left half of the s-plane, where the poles are the roots of the denominator polynomial of the rational function, 2) the rational function does not contain multiple poles along the imaginary axis of the s-plane, and 3) the difference between the numerator

and denominator orders of the rational function does not exceed unity, implying that $|NS - DS| \leq 1$. For time-domain simulation, the rational function has to satisfy the stability condition.

1.3.4 Passivity

The passivity condition requires that a passive circuit does not create energy [19], [32], [46]. The passivity conditions for a multiport network $[G(s = \sigma + j\omega)]$ are twofold, namely, 1) $[G(s^*)] = [G^*(s)]$ for all s, where * is the complex conjugate operator and 2) $[G(s)]$ is a positive real matrix, i.e., the product $z^{*T}[G^T(s^*) + G(s)]z \geq 0$, for all s with $Re(s) > 0$ and any arbitrary vector z. When the rational function matrix $[H(s)]$ is used, these conditions translate into the following passivity constraints: 1) $[H(s)]$ does not contain poles on the right half of the s-plane, 2) $[H(s)]$ does not have multiple poles on the imaginary axis of the s-plane, 3) the coefficients of $[H(s)]$ are all real, and 4) the real part of $[H(s)]$ must be positive semi-definite for all frequencies, implying that the eigenvalues of $Re[H(s)]$ are positive or zero for all frequencies. Among the above constraints, the first and second constraints are included as part of the stability condition and the third constraint is equivalent to the constraint for real coefficients described earlier. Therefore, the passivity condition needs to ensure real coefficients and satisfy the stability condition. In addition, the eigenvalues of the real part of the rational function matrix must be all positive.

1.4 Issues in the Construction of Macromodels

This section discusses several issues that need to be handled during the automated construction of scalable, passive and broadband macromodels.

1.4.1 Scalable Macromodels

During the manufacturing of embedded passive devices, there are several undesirable manufacturing variations due to changes in the mask film resolution, alignment between layer masks, and material processes for embedded passive components. These variations result in physical and electrical variations of design parameters such as thickness and dielectric constant. To alleviate these problems, RF designers prefer to parameterize these variations using design libraries. However, as embedded inductors become complex and the operating frequency increases, it is difficult to capture the distributed parasitic behavior of inductors with many variations.

Over the last decade, macromodeling techniques have been used for building design libraries for embedded passive devices. In [36], the macromodel based on the rational function was successfully applied for capturing the frequency response of embedded inductors using full-wave electromagnetic simulators and measurements. In [54], a methodology using the generalized multidimensional rational function, which provides a mapping between the frequency response and the physical parameters, was developed. This was successfully applied to microwave devices in [54]. Using the multidimensional function, the frequency response can be represented as:

$$S(s, p_1, p_2, p_3, \cdots, p_n) = \frac{P_{num}(s, p_1, p_2, p_3, \cdots, p_n)}{P_{den}(s, p_1, p_2, p_3, \cdots, p_n)} \tag{1.2}$$

where $P_{num}(s, p_1, p_2, p_3, ..., p_n)$ and $P_{den}(s, p_1, p_2, p_3, ..., p_n)$ are arbitrary polynomials of $s = j\omega$ and design parameters $p_1, \cdots, p_n$.

For the construction of design libraries of embedded passive components fabricated using multilayer technology, it is important to construct the scalable macromodel that not only captures the distributed parasitic behavior but also provides a mapping between the frequency response and the design parameters of the device. If the scalable macromodel is constructed using measurements, test vehicles having several embedded inductors with design variations are necessary. If electromagnetic

simulators are used to construct the scalable macromodel, the number of frequency samples required to represent the frequency response becomes an important parameter. As the grid size decreases and the frequency samples increase, the simulation time increases, which limits the construction of design libraries. Hence, there are clear needs for developing adaptive methods that reduce the frequency samples required during the construction of scalable macromodels. It is important to note that if time-domain simulation is not required, there are no constraints to be satisfied during the construction of scalable macromodels except that the frequency response using bandlimited data be accurately interpolated. In this dissertation, the scalable macromodel has been used both for interpolation and extrapolation of frequency data.

1.4.2 Passive Macromodels

For time-domain simulation, a passive macromodel needs to satisfy the conditions of real coefficients, stability, and passivity. The constraint for real coefficients can be satisfied by construction, while the stability condition can be satisfied by ensuring that the poles of the rational function lie on the left half of the complex s-plane. However, satisfying the passivity condition is more difficult since it needs to be guaranteed over infinite frequency bandwidth.

If common poles are used to represent the rational function matrix $[H(s)]$ of a multiport passive circuit, methods developed for guaranteeing passivity of the macromodel can be categorized into two techniques, namely, indirect [32] and direct [46]. In [32], the authors have proposed a method that computes the frequency response of the macromodel, searches the frequency band of violation, and compensates the non-passive macromodel by inserting additional rational functions, as shown in Figure 8(a). In [46], an eigenvalue approach has been discussed, which enforces passivity of the macromodel by directly compensating the poles and residues of the rational function using linearization and constrained minimization through Quadratic

Programming, as shown in Figure 8(b). In Figure 8, the small dotted line is the frequency response of the macromodel and the solid line is the frequency response of the compensated macromodel.

However, both methods, which are based on searching the frequency band of violation, are computationally expensive and use discrete, band-limited frequency samples for enforcing passivity of the macromodel. Hence, the generated macromodel can still violate passivity over continuous frequency and outside the band-limited frequency response since the macromodel is tested at discrete frequency samples, as shown in Figure 8.

Recently, the rational function matrix $[H(s)]$ with non-common poles have been used for representing the passive macromodel for multiport circuits [69]. Using the rational function matrix with non-common poles, a compensation method has been proposed, which can detect the frequency band violating passivity using the associated Hamiltonian matrix [69]. Since the method can detect the frequency bands with passivity violation for continuous frequency and over infinite frequency bandwidth, the passive macromodel can be constructed. This method shows promise but has been tested on relatively simple examples until now.

1.4.3 Broadband Macromodels

For capturing the moments or the frequency response of distributed interconnect networks, several methods have been proposed using Pade approximation [23]-[28], least squares approximation [33]-[41], and vector fitting [42]-[47]. However, the asymptotic waveform evaluation (AWE) method based on Pade approximation has presented instability problems in the past, meaning that the accuracy of the macromodel is sensitive to small changes in the moments during the construction of the macromodel [26]. Similarly, the instability problem has also been discussed when least squares approximation has been used to represent frequency data as a rational function using power

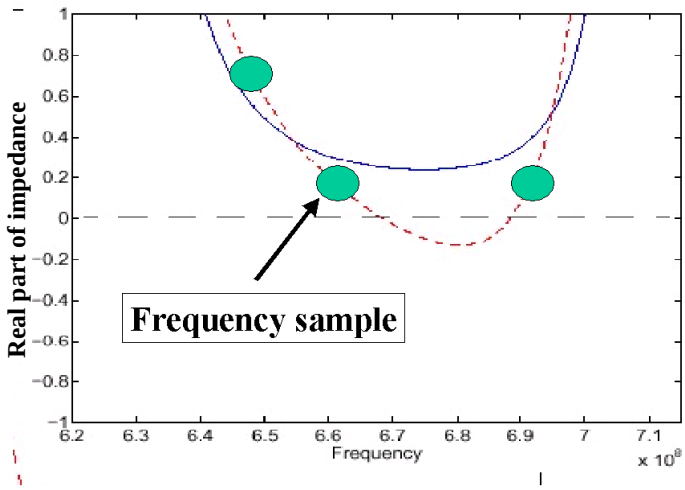

(a)

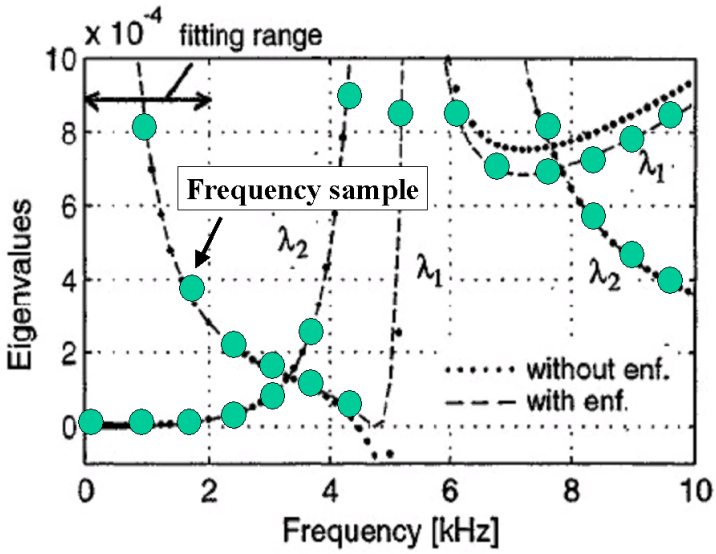

(b)

Figure 8: Passivity violations: (a) indirect compensation [49] and (b) direct compensation [46]

series [38]. This problem can be improved using frequency scaling, which normalizes the frequency term during matrix construction. However, it has been shown that frequency scaling does not result in significant improvement in the approximation beyond 20-30 poles, as illustrated in [39]. Hence, the author in [38] has proposed the Chebyshev polynomial expansion to approximate the frequency response using the orthogonal property of Chebyshev polynomials, which increases the accuracy of the coefficient vectors of the macromodel. However, Chebyshev polynomials need to be converted into the pole-residue representation for integrating the model into circuit simulators [38]. In [45], an iterative method called vector fitting has been proposed for increasing the accuracy of stable poles in the rational function.

However, since the methods presented in [23]-[47] used a single matrix for the construction of the macromodel, they pose a problem for distributed interconnect networks, which often contain hundreds of poles. This is due to the ill-conditioned matrix problem, which often translates to long computational times and large computational memory. Therefore, the ill-conditioned matrix problem arising during the construction of the macromodel still needs to be solved when the frequency response of distributed networks needs to be approximated.

1.4.4 Model Order Reduction

For fast time-domain simulation, the purpose of a passive macromodel is to replace the electromagnetic behavior of the circuit with a reduced order model at the input/output ports. Hence, several methods for reducing the order of passive macromodels have been proposed [23]-[47]. If a macromodel with order $2N$ is reduced, the macromodel cannot capture the N pole pairs present in the frequency response. Therefore, it is important to determine the dominance of poles for reducing the order of the macromodel.

For the construction of scalable, passive, broadband macromodels, the orders

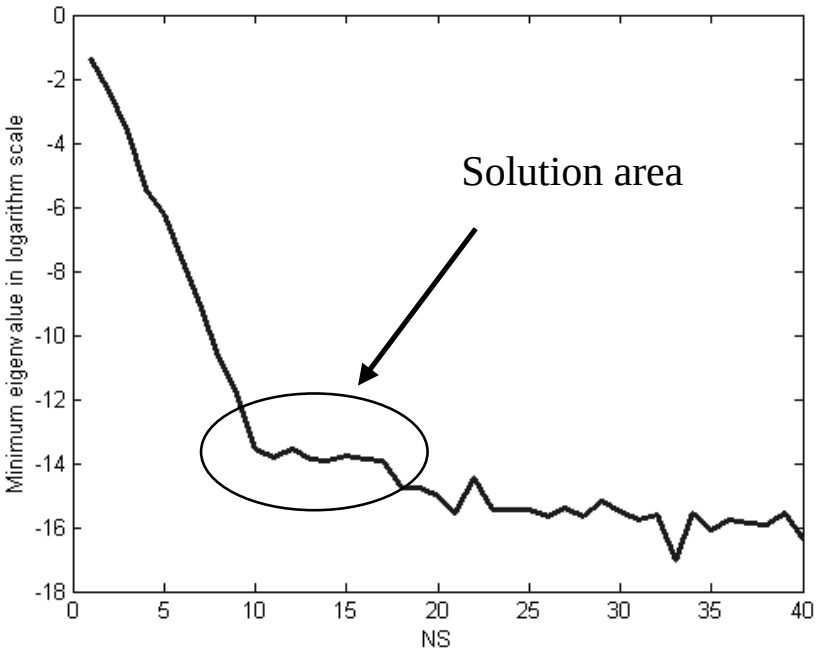

Figure 9: Minimum eigenvalue tracking method vs. the order NS

NS and DS of the rational function in Equation (1.1) need to be estimated. In [48], the order of the rational function has been estimated by using the minimum eigenvalue tracking method, as shown in Figure 9. In Figure 9, the minimum eigenvalue has been plotted as a function of the order NS, which provides the optimum solution area where a non-trivial solution exists. However, this method is limited to low order systems due to the ill-conditioned matrix problem associated with least squares approximation, as discussed later in Chapter 4. Another method for estimating the order of the rational function is to estimate the number of resonant peaks in the frequency response, since an accurate representation for a response with N resonant peaks requires a macromodel with order $2N$ in Equation (1.5). However, this method requires a manual calculation of the number of resonant peaks in the frequency response. Hence, there are clear needs for the automated estimation of the order of scalable, passive, broadband macromodels during the construction of macromodels.

1.5 Numerical Approximation

The rational function in Equation (1.1) can be written in three forms as follows: polynomial form, pole-zero form, and pole-residue form. Equation (1.1) is a polynomial representation using a power series expansion. By computing the roots of the numerator and denominator polynomials of Equation (1.1), the polynomial form can be rewritten in the pole-zero form as:

$$H(s) = k\frac{\prod_{ns}(s-\mu_{ns})}{\prod_{ds}(s-\varphi_{ds})} \tag{1.3}$$

where the complex values φ_{ds} and μ_{ns} are the poles and zeroes of the rational function, respectively. There are two types of roots for the polynomials, real and complex. Based on the constraint for real coefficients of the rational function, the complex roots must always occur in complex conjugate pairs. Hence, the poles and zeroes in Equation (1.3) are real or occur in complex conjugate pairs. In addition, it is assumed that the root is simple and non-overlapping [23]-[47].

Equation (1.1) can also be rewritten in the pole-residue form by computing the roots of the denominator polynomial and its residues as:

$$H(s) = \sum_{ds}\frac{r_{ds}}{s-p_{ds}} + d \tag{1.4}$$

where the complex values p_{ds} are the poles of the rational function and the complex values r_{ds} and d are the residues of the rational function.

1.5.1 Least Squares Approximation

As mentioned earlier, Equation (1.1) cannot be used until the integer orders NS and DS and the real coefficients a_{ns} and b_{ds} are determined. Equation (1.1) can be rewritten in the form:

$$\sum_{ns=0}^{NS} a_{ns}s^{ns} - H(s)\sum_{ds=0}^{DS} b_{ds}s^{ds} = 0 \tag{1.5}$$

For a given $H(s)$ from either measured or simulated data, which represents the frequency response of a one-port network, Equation (1.5) can be written as a matrix equation [48]:

$$[A]\begin{bmatrix} a \\ b \end{bmatrix} = [0] \Leftrightarrow [A]\,[x] = [0] \tag{1.6}$$

where the matrix $[A]$ is given by

$$[A] = \begin{bmatrix} \mathrm{Re}\left\{\sum\limits_{ns=0}^{NS} s_1^{ns}\right\} & -\mathrm{Re}\left\{H(s_1)\sum\limits_{ds=0}^{DS} s_1^{ds}\right\} \\ \mathrm{Im}\left\{\sum\limits_{ns=0}^{NS} s_1^{ns}\right\} & -\mathrm{Im}\left\{H(s_1)\sum\limits_{ds=0}^{DS} s_1^{ds}\right\} \\ \vdots & \vdots \\ \mathrm{Re}\left\{\sum\limits_{ns=0}^{NS} s_k^{ns}\right\} & -\mathrm{Re}\left\{H(s_k)\sum\limits_{ds=0}^{DS} s_k^{ds}\right\} \\ \mathrm{Im}\left\{\sum\limits_{ns=0}^{NS} s_k^{ns}\right\} & -\mathrm{Im}\left\{H(s_k)\sum\limits_{ds=0}^{DS} s_k^{ds}\right\} \end{bmatrix}$$

In Equation (1.6), each row represents a frequency sample in the matrix $[A]$. The vectors $[a]$ and $[b]$ in Equation (1.6) are real coefficient vectors of the numerator and denominator, respectively. After pre-multiplying Equation (1.6) with the transpose of $[A]$, Equation (1.6) becomes:

$$[A]^T\,[A]\,[x] = [0] \tag{1.7}$$

which can be written as an eigenvalue equation [36], [48], [49] in the form:

$$[A]^T\,[A]\,[x] = \lambda_{\min}\,[x] \tag{1.8}$$

where λ_{min} is the minimum eigenvalue of the matrix and the superscript T is the transpose operator. This method for solving Equation (1.8), which was proposed in the past by Choi, et al. [48], is called the eigenvalue method in this dissertation. To solve Equation (1.8), the computation of the real coefficient vector $[x]$, which contains the coefficient vectors $[a]$ and $[b]$ of the rational function, requires the estimation of the integer orders, NS and DS. Once the orders are determined, the eigenvector $[x]$

related to the minimum eigenvalue λ_{min} can be computed. The stability can now be enforced on the denominator coefficient vector $[b]$ of the eigenvector $[x]$ in Equation (1.8) by applying the stability constraints. Using the root finding method [68], the stability constraints have been enforced by computing all the poles of the rational function and retaining only the stable poles. The stable poles can be real or complex conjugate poles, but it has been assumed that the pole is simple or non-overlapping in this formulation.

For computing the residues corresponding to the stable, common, real and complex conjugate poles, the matrix $[A]$ in Equation (1.6) can be reformulated as Equation (1.9) using the pole-residue form in Equation (1.4).

$$\begin{bmatrix} \mathrm{Re}\left\{\sum_m \frac{1}{(s_1-p_m)} & \sum_n \frac{2(s_1-p_{nr})}{(s_1-p_{nr})^2+p_{ni}^2} & \sum_n \frac{-2p_{ni}}{(s_1-p_{nr})^2+p_{ni}^2} & \sum_k \frac{s_1}{(s_1-p_k)} & 1 & 0 & -G(s_1)\right\} \\ \mathrm{Im}\left\{\sum_m \frac{1}{(s_1-p_m)} & \sum_n \frac{2(s_1-p_{nr})}{(s_1-p_{nr})^2+p_{ni}^2} & \sum_n \frac{-2p_{ni}}{(s_1-p_{nr})^2+p_{ni}^2} & \sum_k \frac{s_1}{(s_1-p_k)} & 0 & s_1 & -G(s_1)\right\} \\ & & \vdots & & & & \\ & & \vdots & & & & \\ \mathrm{Re}\left\{\sum_m \frac{1}{(s_t-p_m)} & \sum_n \frac{2(s_t-p_{nr})}{(s_t-p_{nr})^2+p_{ni}^2} & \sum_n \frac{-2p_{ni}}{(s_t-p_{nr})^2+p_{ni}^2} & \sum_k \frac{s_t}{(s_t-p_k)} & 1 & 0 & -G(s_t)\right\} \\ \mathrm{Im}\left\{\sum_m \frac{1}{(s_t-p_m)} & \sum_n \frac{2(s_t-p_{nr})}{(s_{t1}-p_{nr})^2+p_{ni}^2} & \sum_n \frac{-2p_{ni}}{(s_t-p_{nr})^2+p_{ni}^2} & \sum_k \frac{s_t}{(s_t-p_k)} & 0 & s_t & -G(s_t)\right\} \end{bmatrix} \begin{bmatrix} \gamma_1 \\ \vdots \\ \alpha_1 \\ \vdots \\ \beta_1 \\ \vdots \\ \varphi_1 \\ \vdots \\ \delta \\ \eta \\ 1 \end{bmatrix} = \begin{bmatrix} 0 \\ 0 \\ \vdots \\ \vdots \\ 0 \\ 0 \end{bmatrix} \tag{1.9}$$

In Equation (1.9), the residues can be real residues γ_m for real poles p_m, complex conjugate residues $\alpha_n \pm j\beta_n$ for complex conjugate poles $p_{nr} \pm jp_{ni}$, and real residues φ_k for real poles p_k. In addition, Equation (1.9) consists of a constant residue δ, a linear frequency dependent residue η, and the frequency response G. In Equation (1.9), the real and imaginary parts are separated to ensure that the coefficients of rational functions are always real. For a multiport network containing common poles, the residues for each port are constructed independently using Equation (1.9). Equation (1.9) is also used in vector fitting [45] by moving the column vector of the frequency response G into the right side of Equation (1.9).

1.5.2 Vector Fitting

In [36], the coefficients of the rational function in Equation (1.1) have been computed after constructing a linear matrix equation and solving the eigenvalue problem. However, since the power series expansion inherently generates an ill-conditioned matrix, the solution using the eigenvalue method can generate inaccurate poles. Therefore, the method based on the least squares approximation is limited to low order systems having a few poles, which will be discussed in later chapters. One prominent method for overcoming the numerical limitations is an iterative method called vector fitting, which iteratively extracts accurate stable poles of the rational function [45].

The fundamental formulation for vector fitting using the pole-residue form of the rational function can be written as:

$$\left(\sum_{ds=1}^{DS} \frac{r_{ds}}{s - p_{ds}} + d + es\right) = \left(\sum_{ds=1}^{DS} \frac{R_{ds}}{s - p_{ds}} + 1\right) H(s) \tag{1.10}$$

where the residues r_{ds} and R_{ds} are the unknown values to be computed using the given poles p_{ds} of the rational function. The left part of Equation (1.10) also has a constant residue d and a linear frequency dependent residue e, where d and e are the unknown real values. Depending on the application, these two residues are included in the formulation [45].

As an initialization step, the method requires the estimation of the order DS and the stable poles p_{ds} of the rational function in Equation (1.10). Once the initial poles are selected, the method computes the residues using the least squares approximation, as shown in Equation (1.9). For extracting new poles in the subsequent step from the residues R_{ds}, Equation (1.10) can be rewritten in the pole-zero form as:

$$e\frac{\prod_{ds=1}^{DS+1} (s - z_{ds})}{\prod_{ds=1}^{DS} (s - p_{ds})} = \frac{\prod_{ds=1}^{DS} (s - Z_{ds})}{\prod_{ds=1}^{DS} (s - p_{ds})} H(s) \tag{1.11}$$

where z_{ds} and Z_{ds} are the zeroes of the rational function in the left and right side of the

equation, respectively. After cross-multiplying $\prod_{ds=1}^{DS}(s-p_{ds})$ on both sides, Equation (1.11) becomes:

$$e\prod_{ds=1}^{DS+1}(s-z_{ds}) = \prod_{ds=1}^{DS}(s-Z_{ds})H(s) \tag{1.12}$$

Rewriting Equation (1.12), the rational function $H(s)$ can be represented in the pole-zero form as:

$$H(s) = e\frac{\prod_{ds=1}^{DS+1}(s-z_{ds})}{\prod_{ds=1}^{DS}(s-Z_{ds})} \tag{1.13}$$

where the zeros z_{ds} and Z_{ds} in Eq. (1.11) become the zeros and poles of the rational function, respectively, and the poles Z_{ds} are used in the following step. During the iteration process, the unstable poles of Z_{ds} in Equation (1.13) are appropriately modified for satisfying the stability condition. After a few iterations from Equations (1.10) to (1.13), the vector fitting method extracts accurate poles and residues provided that the poles are selected appropriately in the initial step. For faster convergence and extraction of stable poles, the authors in [45] have recommended that the initial stable poles be complex conjugate poles.

1.5.3 Multiport Approximation

This section begins by considering an arbitrary N-port network. In general, any linear time-invariant passive system for a N-port network can be represented as:

$$[H(s)] = \begin{bmatrix} H_{11}(s) & H_{12}(s) & \cdots & H_{1N}(s) \\ H_{21}(s) & H_{22}(s) & \cdots & H_{2N}(s) \\ \vdots & \vdots & \ddots & \vdots \\ H_{N1}(s) & H_{N2}(s) & \cdots & H_{NN}(s) \end{bmatrix} \tag{1.14}$$

where $s = j\omega$, ω is the angular frequency in radians per second. The transfer function matrix $[H(s)]$ can be the scattering function matrix $[S(s)]$ capturing scattering parameters $[S]$, admittance function matrix $[Y(s)]$ capturing admittance parameters $[Y]$, or impedance function matrix $[Z(s)]$ capturing impedance parameters $[Z]$.

If the functions $H_{ij}(s)$ of the transfer function matrix $[H(s)]$ represent a common pole system using rational functions, Equation (1.14) can be written as:

$$[H(s)] = \frac{[Q(s)]}{P(s)} = \frac{\begin{bmatrix} Q_{11}(s) & Q_{12}(s) & \cdots & Q_{1N}(s) \\ Q_{21}(s) & Q_{22}(s) & \cdots & Q_{2N}(s) \\ \vdots & \vdots & \ddots & \vdots \\ Q_{N1}(s) & Q_{N2}(s) & \cdots & Q_{NN}(s) \end{bmatrix}}{P(s)} \tag{1.15}$$

where the common denominator polynomial $P(s)$ is

$$P(s) = \sum_{ds=0}^{DS} b_{ds} s^{ds} = [s]_{DS} \, [b]_{DS}^{T} \tag{1.16}$$

In Equation (1.16), DS is the order of the denominator polynomial, $[s]_{DS}$ is a column vector having elements s^k, $k = 0, 1, ..., DS$, $[b]_{DS}$ is a column vector having $DS + 1$ unknown coefficients for power series, and the superscript T is the transpose operator. Similarly, the numerator polynomial $Q_{ij}(s)$ in Equation (1.15) can be written in matrix form as:

$$Q_{ij}(s) = \sum_{ns_{ij}}^{NS_{ij}} a_{ns_{ij}} s^{ns_{ij}} = [s]_{NS_{ij}} \, [a_{ij}]_{NS_{ij}}^{T} \tag{1.17}$$

where NS_{ij} is the order of the numerator polynomial $Q_{ij}(s)$, $[s]_{NS_{ij}}$ is a column vector having elements s^k, $k = 0, 1, ..., NS_{ij}$, and $[a_{ij}]_{NS_{ij}}$ is a column vector having $NS_{ij} + 1$ unknown coefficients.

For given orders DS and NS_{ij}, one of the goals of this dissertation is to find the denominator coefficient vector $[b]_{DS}$ and the numerator coefficient vectors $[a_{ij}]_{NS_{ij}}$. Along with the assumption that the system has common poles, it is also assumed that the rational function matrix $[H(s)]$ is reciprocal or symmetric, $H_{ij}(s) = H_{ji}(s)$. Hence, only the lower or upper diagonal numerator polynomial functions of the rational function matrix $[H(s)]$ need to be computed.

For computing the coefficients of the common denominator polynomial and the symmetric residue polynomial matrix, Equation (1.14) can be written in the matrix

equation form as:

$$\begin{bmatrix} A_1 \\ \vdots \\ A_m \\ \vdots \\ A_M \end{bmatrix} [x] = [0] \Leftrightarrow [A]\,[x] = [0] \Leftrightarrow [A]^T\,[A]\,[x] = \lambda_{\min}\,[x] \tag{1.18}$$

where M is the number of frequency samples, and the matrix $[A_m]$ and the vector $[x]$ are given by:

$$[A_m] = \begin{bmatrix} [s_m]_{NS_{11}} & [0] & [0] & \cdots & \cdots & \cdots & \cdots & \cdots & [0] & -H_{11}(s_m)\,[s_m]_{DS} \\ [0] & \ddots & \ddots & \ddots & & & & & \vdots & \vdots \\ [0] & \ddots & [s_m]_{NS_{1N}} & [0] & \ddots & & & & \vdots & -H_{1N}(s_m)\,[s_m]_{DS} \\ \vdots & \ddots & [0] & [s_m]_{NS_{22}} & \ddots & \ddots & & & \vdots & -H_{22}(s_m)\,[s_m]_{DS} \\ \vdots & & \ddots & \ddots & \ddots & \ddots & \ddots & & \vdots & \vdots \\ \vdots & & & \ddots & \ddots & [s_m]_{NS_{2N}} & [0] & \ddots & \vdots & -H_{2N}(s_m)\,[s_m]_{DS} \\ \vdots & & & & \ddots & [0] & [s_m]_{NS_{33}} & \ddots & [0] & -H_{33}(s_m)\,[s_m]_{DS} \\ \vdots & & & & & \ddots & \ddots & \ddots & [0] & \vdots \\ [0] & \cdots & \cdots & \cdots & \cdots & \cdots & [0] & [0] & [s_m]_{NS_{NN}} & -H_{NN}(s_m)\,[s_m]_{DS} \end{bmatrix}$$

$$[x] = \begin{bmatrix} [a]_{NS_{11}} & \cdots & [a]_{NS_{1N}} & [a]_{NS_{22}} & \cdots & [a]_{NS_{2N}} & [a]_{NS_{33}} & \cdots & [a]_{NS_{NN}} & [b]_{DS} \end{bmatrix}^T$$

Using the eigenvalue method discussed in Chapter 1, Equation (1.18) can be solved. However, because of the stability condition on the roots (poles) of the denominator polynomial $P(s)$ during the construction of passive macromodels, the unstable poles of the vector $[b]_{DS}$ need to be discarded after using the root finding method in [68]. Due to the unstable poles, the numerator coefficient vectors $[a]_{NS_{ij}}$ need to be modified for computing the residue polynomial matrix $[Q(s)]$. Hence, the matrix $[Q(s)]$ needs to be recalculated using Equation (1.9).

1.6 Proposed Research and Dissertation Outline

The objective of this dissertation is to develop methods for the automated construction of scalable, passive and broadband macromodels that capture the electromagnetic behavior of multiport distributed passive networks. These macromodels should have the required properties such that they can be combined with a larger circuit for simulation in a commercial circuit simulator such as SPICE. As mentioned earlier, the frequency response of the passive networks can be extracted using an electromagnetic simulator or measurements.

The following items have been discussed in various sections of this dissertation:

- **Scalable Macromodel Development**

  1. **Comparison between rational functions using power series and orthogonal polynomials:** A rational function using power series has a large dynamic range in the elements during matrix construction and hence results in an ill-conditioned matrix. After replacing the power series expansion with orthogonal polynomials, the accuracy and efficiency of the rational function is studied.

  2. **Development of scalable macromodels for building design libraries:** For building design libraries, the generalized multidimensional rational function [54] has been reformulated as a multiplication of one-dimensional rational functions. The multidimensional function has been constructed using a power series expansion and orthogonal polynomials. This has been applied to embedded inductors used in packaging. The scalable macromodel is a parameterized model that provides a mapping between the frequency response and electrical response of the device, as mentioned earlier.

3. **Development of the selective sampling method for reducing the number of frequency samples:** Data at discrete frequency samples can be extracted using an electromagnetic simulator. If frequency samples are numerous, this translates into an increase in simulation time. Hence, a selective sampling method has been developed for minimizing the number of frequency samples required.

4. **Application of scalable macromodels derived from electromagnetic simulation and measurements:** To confirm the accuracy of scalable macromodels, one-port embedded rectangular spiral inductors were simulated using an electromagnetic simulator. In addition, one-port embedded circular spiral inductors were fabricated on a specially designed test vehicle using laminate technology. In both cases, the physical parameters were varied to ensure an accurate mapping between the physical and electrical parameters. The scalable macromodels constructed were then tested at intermediate points to check their accuracy.

- **Passive Macromodel Development**

1. **Derivation of multiport passivity formulae:** Using the concept that the summation of passive sub-networks is passive, multiport passivity formulae were analytically derived for the construction of passive macromodels using filter theory and the pole-residue form of the rational function matrix. The properties of multiport passivity formulae have been discussed in this dissertation.

2. **Development of methods for compensating a non-passive macromodel using multiport passivity formulae:** If multiport passivity formulae are violated, passivity needs to be enforced. Negative eigenvalues of the real part of the rational function matrix have been set equal to

zero or changed to a small positive value for enforcing passivity of non-passive macromodels. For completeness, since enforcing passivity using multiport passivity formulae is a sufficient but not necessary condition, the limitations of the passivity enforcement process have been discussed.

3. **Network synthesis:** To enable circuit simulation, the passive macromodel has been synthesized into SPICE net lists using resistors, inductors, capacitors, and controlled sources.

- **Broadband Macromodel Development**

  1. **Development of methods for capturing hundreds of poles:** For capturing large number of poles in the frequency response, methods have been developed based on the concept that a passive system can be represented as a summation of passive sub-systems. These methods include:

     – **Band division**, which divides the entire computational domain into sub-computational domains or subbands for alleviating the ill-conditioned matrix problem

     – **Subband reordering**, which provides a construction sequence for reducing the interaction between subbands

     – **Subband dilation**, which provides local correction in the boundary region between subbands

     – **Pole replacement**, which increases the accuracy of the macromodel by replacing inaccurate poles with accurate poles near the maximum error deviation point

  2. **Development of an automated macromodel construction method:** For automation, it is important to determine the subbands from the frequency response. Each subband can be determined using the frequency range of resonant peaks and nulls in the frequency response. Hence, an

automated method that detects the peaks and nulls has been developed by checking the magnitude of the frequency response. This information is used to represent the frequency response as a collection of subbands.

3. **Development of methods for reducing the macromodel construction time:** For a matrix of size C, the required computation time is $O(\frac{2}{3} \times C^3)$ for LU decomposition. For approximating the poles of common pole systems, the size of the matrix for symmetric N-port networks becomes $N \approx NS \times N^2$, where NS is the order of the macromodel. The solution of such matrices requires computation time of $O(\frac{2}{3} \times NS^3 \times N^6)$. As N increases, the construction time of the macromodel is dominated by the term N, which is the number of ports. Hence, methods for reducing the construction time of the macromodel have been developed using the properties of common pole systems.

4. **Development of methods for reducing the order of the macromodel for saving simulation time in a circuit simulator:** As the order of the macromodel increases, the number of electrical elements during network synthesis increases and therefore the simulation time increases as well. Hence, methods for reducing the order of the macromodel have been developed by limiting the frequency band of interest or the amplitude range. Since the order of the macromodel is reduced after the construction of the macromodel, neither the stability nor passivity condition is violated. Details of the methods developed for reducing the order of the macromodel have been discussed in this dissertation.

5. **Development of a software program for the automated construction of macromodels:** The methods developed in this dissertation have been realized in the Broadband Efficient Macromodeling Program (BEMP)

developed at Georgia Tech, which uses C++ and is executable on a Windows operating system. The details of this software program have been provided in this dissertation.

- **Test Cases**

  The methods discussed in this dissertation have been applied to several test cases that are representative of distributed networks. These test cases include:

  - Interconnect with known transfer function
  - One-port transmission line
  - Four-port lossy transmission line
  - Four-port transmission line data from a vector network analyzer measurement
  - Four-port power plane pair with decoupling capacitors
  - Power distribution network from Rambus
  - Fourteen-port power distribution network for INC (Intelligent Network Communicator) board from Packaging Research Center
  - Thirty-two-port bus from HRL (Hughes Research Labs)

The remainder of this thesis is organized as follows. Chapter 2 presents methods for the construction of scalable macromodels for building design libraries of embedded passive components using the generalized multidimensional rational function. Use of orthogonal polynomials and selective sampling has been presented in Chapter 2. Chapter 3 discusses the pole-residue form of the rational function for representing a linear time-invariant passive network. Analytical formulae for multiport passive circuits based on the pole-residue form of the rational function have been presented for enforcing passivity. In addition, methods for compensating the non-passive macromodels have been discussed and the passive macromodels have been synthesized into

circuit elements for circuit simulation. Chapter 4 presents band division, subband reordering, subband dilation, and pole replacement methods for the construction of broadband macromodels containing a large number of poles. This chapter also discusses methods for reducing the construction time, for estimating the order of the macromodel, and for reducing the order of the macromodel. In Chapter 5, several test cases representative of distributed interconnect networks using the methods developed in this dissertation are presented, followed by the conclusion and future work in Chapter 6.

CHAPTER II

SCALABLE MACROMODELS

The focus of scalable macromodeling is to parameterize interconnect networks as a function of design and material parameters. One application of scalable macromodels is the construction of design libraries for embedded passive devices arising in advanced packaging [54], [55]. To achieve this goal, both orthogonal polynomials [64], [65] and multidimensional rational functions [54] have been discussed in this chapter. The orthogonal polynomials have been used and compared with power series for increasing the accuracy and convergence of scalable macromodels. The multidimensional rational functions provide a mapping between the frequency response and the physical or material parameters of the structure.

Since the scalable macromodels are constructed from frequency dependent data of the device obtained using an electromagnetic tool or from measurements, methods that reduce computation time and increase accuracy are required. For an electromagnetic simulator discretizing Maxwell's equation and computing the frequency response, the frequency samples and grid size in the electromagnetic simulator dictate the computation time. If the frequency response is obtained from a vector network analyzer measurement, the number of embedded passive devices with design variations that must be measured becomes a major challenge for reducing the real estate in the test vehicle. In either case, methods for reducing both the frequency samples and physical variables of the device as well as increasing the accuracy of the scalable macromodel are required. Therefore, a selective sampling method has been developed for minimizing the number of sampling points (frequency and design variables) required for improving both time and accuracy.

Using the cavity resonator model [49] for generating the frequency response of a power plane pair, scalable macromodels have been developed for this structure using orthogonal polynomials and selective sampling. The methods have also been applied for generating scalable macromodels for embedded inductors in organic substrates fabricated using laminate technology developed at the Packaging Research Center [58].

2.1 Orthogonal Polynomials

Consider a function $N(\omega)$ represented as a power series expansion in the form:

$$N(\omega) = \sum_{k} a_k \omega^k \tag{2.1}$$

where ω is a real variable and a_k are complex coefficients. Assuming ω is angular frequency, the frequency response of ω^k as a function of order k is shown in Figure 10. From the figure, it can be noted that as the order k of the power series expansion becomes large, the frequency response does not improve. For example, $\sum_{20} \omega^k$ has a similar response as $\sum_{24} \omega^k$ within the computational domain $0 \leq \omega \leq 1$. Hence, when the order of the power series expansion becomes large, an increase in the number of expansion terms does not improve accuracy [38].

Assuming the function is now represented as a rational function as in Equation (1.1), the problem in Figure 10 can be alleviated using Chebyshev polynomials in the numerator and denominator of the rational function [38]. This is because the orthogonal property of Chebyshev polynomials increases the accuracy of the coefficients in the rational function. Hence, this section compares the performance of several kinds of orthogonal polynomials for approximating the frequency response of the device. It is important to note that the nth term, ω^n, in Equation (2.1) is replaced with the orthogonal polynomial of degree n.

Since the orthogonal polynomials currently available are mainly real-valued expansions [64], [65], the power series expansion of the complex variable 's' needs to

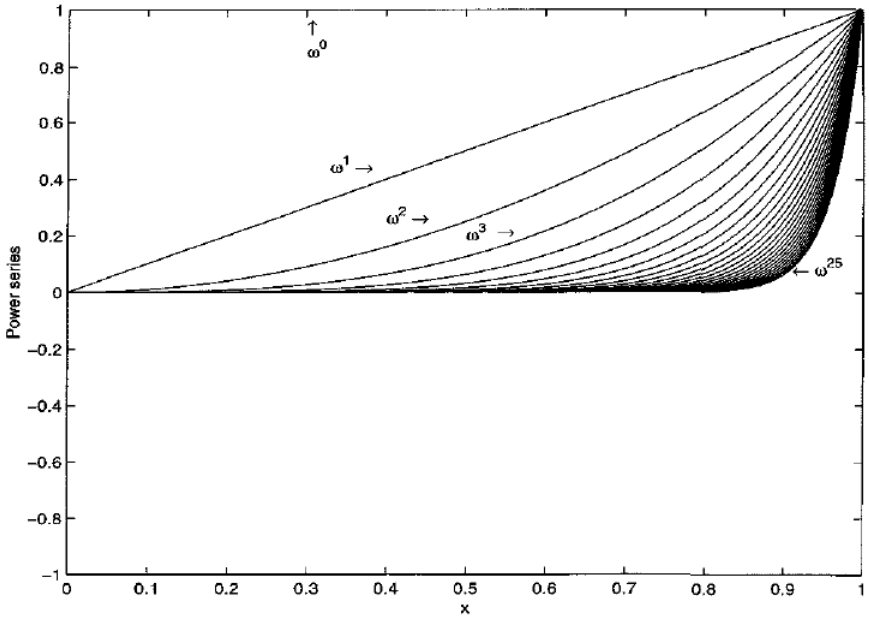

Figure 10: Frequency response of the power series expansion [38]

be converted into the power series expansion of a real variable 'ω'. As an example, consider a power series expansion $N(s)$ having real coefficients written in the form:

$$N(s) = 3 + 2s + 10s^2 + 7s^3 + 5s^4 \tag{2.2}$$

Substituting $s = j\omega$ into Equation (2.2), the power series expansion with variable ω can be written as:

$$N(s = j\omega) = 3 + j2\omega - 10\omega^2 - j7\omega^3 + 5\omega^4 \tag{2.3}$$

In general, the power series expansion of a complex variable s with real (or complex) coefficients in Equation (2.2) can be rewritten as the power series expansion of a real variable ω with complex coefficients, as shown in Equation (2.3). Hence, the rational function with the power series expansion can be represented as:

$$H(s = j\omega) = \frac{\sum_{ns=0}^{NS} a_{ns}\omega^{ns}}{\sum_{ds=0}^{DS} b_{ds}\omega^{ds}} \tag{2.4}$$

Table 1: Recurrence relations of orthogonal polynomials [65]

	ω	$O_0(\omega)$	$O_1(\omega)$	A_n	B_n	C_n
Legendre $L(\omega)$	[-1 1]	1	ω	$\frac{2n+1}{n+1}$	0	$\frac{n}{n+1}$
Chebyshev I $T(\omega)$	[-1 1]	1	ω	2	0	1
Chebyshev II $U(\omega)$	[-1 1]	1	2ω	2	0	1

where the angular frequency ω is real and the coefficients a_{ns} and b_{ds} are complex. The function in Equation (2.3) can be replaced with orthogonal polynomials and rewritten in the form:

$$N(s = j\omega) = 3O_0(\omega) + j2O_1(\omega) - 10O_2(\omega) - j7O_3(\omega) + 5O_4(\omega) \tag{2.5}$$

where $O_n(\omega)$ is the orthogonal polynomial of degree n. Details on several kinds of orthogonal polynomials are available in [64], [65]. In this dissertation, Legendre and Chebyshev I and II polynomials have been implemented. Using recurrence relations, the orthogonal polynomial of degree $n + 1$ can be evaluated as:

$$O_{n+1}(\omega) = (A_n\omega + B_n)O_n(\omega) - C_nO_{n-1}(\omega) \tag{2.6}$$

where the polynomials $O_0(\omega)$ and $O_1(\omega)$ and the coefficients A_n, B_n, C_n are shown in Table 1. It is important to note that since these polynomials preserve the orthogonal property within the range of ω, it is required that the computational domain be mapped into that range. This range is shown in the second column of Table 1. The frequency responses of orthogonal polynomials in the range [-1 1] are shown in Figure 11.

From Equation (2.4), the rational function with orthogonal polynomials can be represented as:

$$H(s = j\omega) = \frac{\sum_{ns=0}^{NS} c_{ns}O_{ns}(\omega)}{\sum_{ds=0}^{DS} d_{ds}O_{ds}(\omega)} \tag{2.7}$$

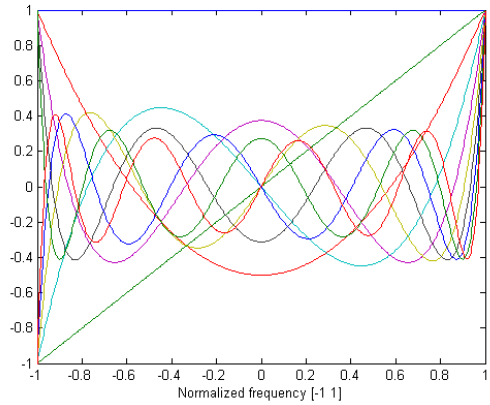

(a)

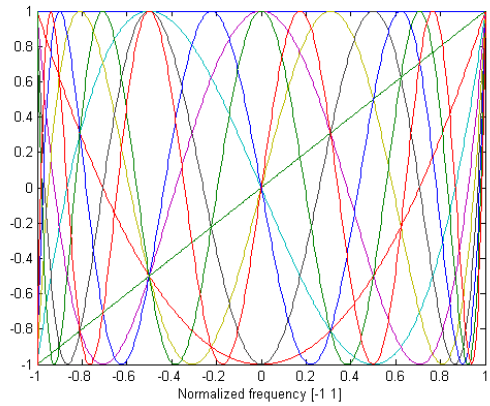

(b)

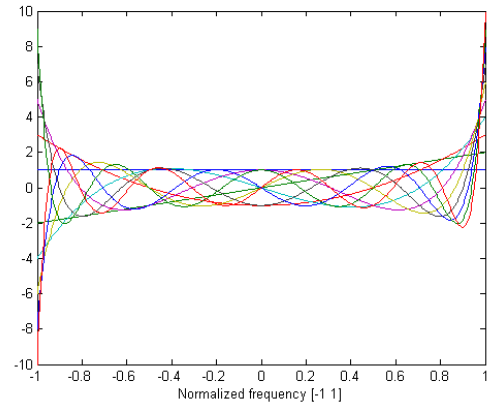

(c)

Figure 11: Frequency responses of orthogonal polynomials: (a) Legendre polynomials, (b) Chebyshev I polynomials and (c) Chebyshev II polynomials

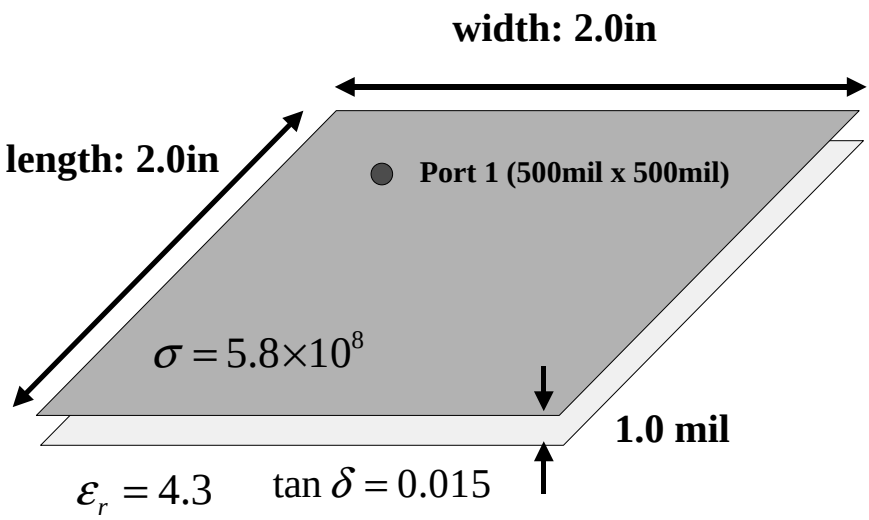

Figure 12: Power plane pair

where $O_n(\omega)$ is the orthogonal polynomial of degree n, which can be generated using Equation (2.6). In Equation (2.7), orders NS, DS and complex coefficients c_{ns}, d_{ds} need to be computed.

2.1.1 Test Case: Power plane pair

For demonstrating the accuracy of the rational function with orthogonal polynomials, consider a 2.0in x 2.0in power plane pair with a 1.0mil thick dielectric (relative permittivity $\epsilon_r = 4.3$ and loss tangent $tan\delta = 0.015$), as shown in Figure 12. It is assumed that both planes are made of copper with conductivity $\sigma = 5.8 \times 10^7$ [S/m].

Using the cavity resonator model with propagating modes $m = 20$ and $n = 20$ [49], a total of 1000 uniformly spaced frequency samples of the impedance parameter at Port 1 (x = 500mil and y = 500mil) was computed from 10.0 MHz to 10.0 GHz. To assess the performance of orthogonal polynomials, $NS = DS$ was assumed and the order was swept from 1 to 50. The frequency response was approximated using the least squares approximation in Equation (1.8) and (1.9), as discussed in Chapter 1. The root-mean-square (RMS) error between the original frequency response and the frequency response of the rational function using the power series expansion and

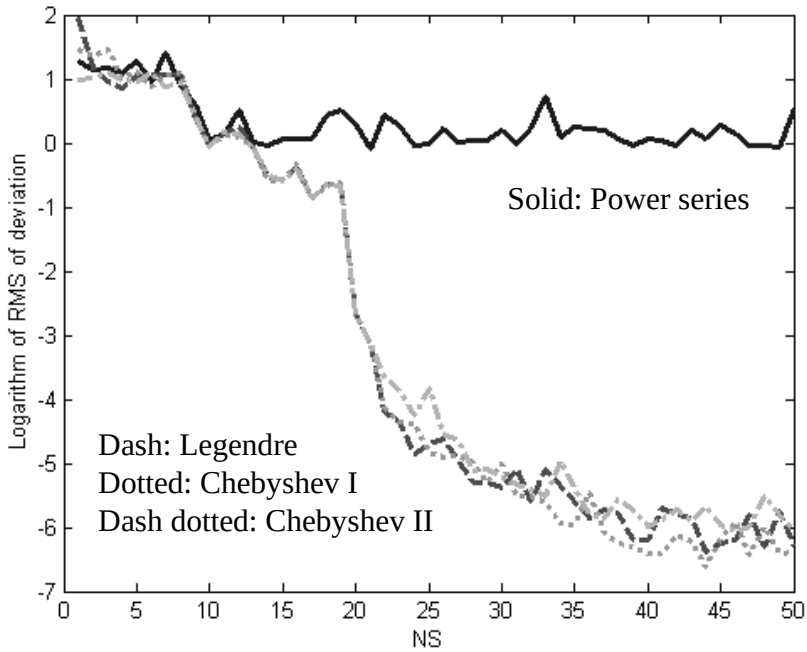

Figure 13: Power series expansion and orthogonal polynomials

orthogonal polynomials are shown in Figure 13. The results demonstrate the accuracy of the rational function approximation using orthogonal polynomials. From Figure 13, the following observation can be derived:

1. The accuracy of the rational function using the power series expansion is not improved beyond the order NS of 10. However, the deviation (RMS error) between the original response and the response of the rational function using orthogonal polynomials continues to decrease until the order $NS = 40$ is reached with the error converging to 10^{-6}. As is obvious, the orthogonal polynomials provide a more accurate approximation than the power series expansion.

2. For order $NS < 13$, the orthogonal polynomials do not provide better accuracy than the power series expansion. This is because polynomials with a low order are used for approximating the frequency response. Hence, estimating the order of the rational function is more important than choosing either the power series

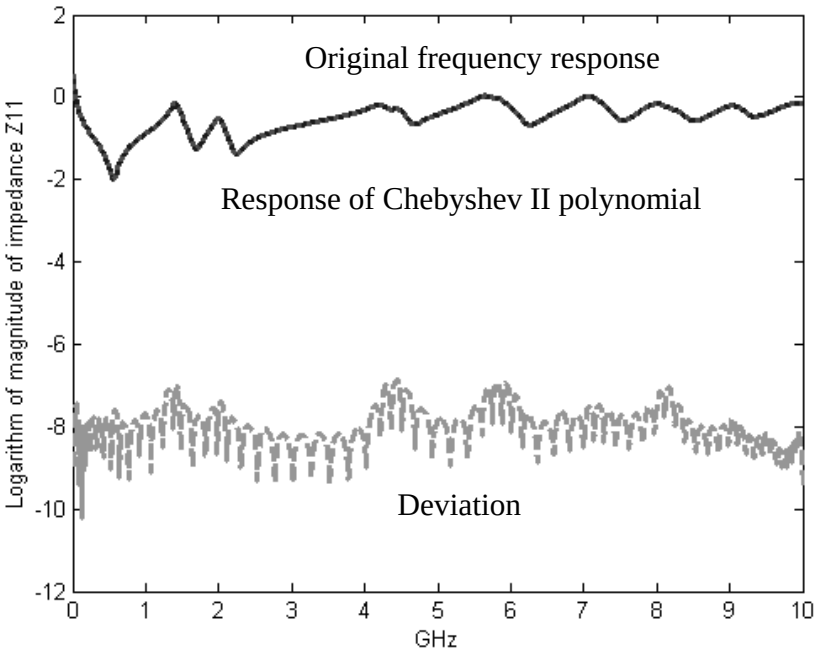

Figure 14: Comparison between the original response and the response of Chebyshev II polynomials

expansion or orthogonal polynomials for increasing the accuracy. The issue on the estimation of orders NS, DS is discussed in Chapter 4.

3. For order $NS > 40$, the orthogonal polynomials converge to an RMS error value of 10^{-6}, meaning that a higher order does not improve the accuracy of the approximation for this example.

For comparison, Figure 14 shows the original frequency response (solid line) of the power plain pair, the frequency response (dotted line) generated from the rational function with order $NS = 50$ using Chebyshev II polynomials, and the deviation (dashed line).

2.2 Scalable Macromodels

Due to the increasing demand for portable wireless devices, the integration of basic electrical components such as resistors, capacitors, and inductors is one of the most

challenging tasks for accomplishing higher levels of integration. These embedded passive components, which have several physical variations in multilayer configurations, have been developed for reducing the physical size and manufacturing cost [1]. For commercializing these devices fabricated using new technologies, it is essential that an electrical model for these devices be available to designers [36]. Hence, design libraries which map the electrical response to the physical (and material) parameters is required, which are the goal of developing the scalable macromodel discussed in this section.

The generalized multidimensional rational function shown in Equation (1.2) can be written as a multiplication of one-dimensional rational functions in the form:

$$H(s, p_1, p_2, \cdots, p_n) = \left(\frac{\sum_{ns=0}^{NS} a(0)_{ns} s^{ns}}{\sum_{ds=0}^{DS} b(0)_{ds} s^{ds}} \right) \left(\frac{\sum_{n1=0}^{N1} a(1)_{n1} p_1^{n1}}{\sum_{d1=0}^{D1} b(1)_{d1} p_1^{d1}} \right) \cdots \left(\frac{\sum_{nn=0}^{NN} a(n)_{nn} p_n^{nn}}{\sum_{dn=0}^{DN} b(n)_{dn} p_n^{dn}} \right) \tag{2.8}$$

where p_k is the kth design parameter of the device. In this dissertation, Equation (2.8) is called a scalable macromodel, which can be used for parameterizing interconnect networks and embedded passive devices. The scalable macromodel provides a mapping between the frequency response and physical or material parameters of the device. The power series expansion in the numerator and denominator of Equation (2.8) can be replaced with orthogonal polynomials discussed in the previous section as:

$$H(s, p_1, p_2, \cdots, p_n) = \left(\frac{\sum_{ns=0}^{NS} a(0)_{ns} O_{ns}(\omega)}{\sum_{ds=0}^{DS} b(0)_{ds} O_{ds}(\omega)} \right) \left(\frac{\sum_{n1=0}^{N1} a(1)_{n1} O_{n1}(p_1)}{\sum_{d1=0}^{D1} b(1)_{d1} O_{d1}(p_1)} \right) \cdots \left(\frac{\sum_{nn=0}^{NN} a(n)_{nn} O_{nn}(p_n)}{\sum_{dn=0}^{DN} b(n)_{dn} O_{dn}(p_n)} \right) \tag{2.9}$$

2.2.1 Test Case: Power plane pair with two design parameters

For demonstrating the methods used for generating scalable macromodels, consider an example of a power plane pair shown in Figure 12. It is assumed here that the data

from 20 different power plane pairs having two design parameters such as the width (1200mil to 2000mil in 200mil increment) and dielectric thickness (1.5mil to 3.0mil in 0.5mil increment) are available along with 50 uniform frequency samples (40.0 MHz to 2.0 GHz) per structure. The frequency response of the 20 different plane pairs with two design parameters was computed using the cavity resonator model in [49].

The scalable macromodel using Chebyshev I polynomials in Table 1 was used. However, since there is no method for estimating the orders NS, DS, $N1$, $D1$, $N2$, $D2$ of the scalable macromodel in the literature, the orders have been swept from 0 to 10 for frequency and from 0 to 5 for two design parameters. It is important to note that the minimum eigenvalue tracking method is only valid for frequency, meaning that it is valid for a single parameter. As a result, the orders $NS = 10$, $DS = 10$, $N1 = 2$, $D1 = 2$, $N2 = 2$, $D2 = 2$ in Equation (2.9), which provide the most accurate approximation, have been used for the construction of the scalable macromodel. The comparison between the original frequency response and the response of the constructed macromodel for 20 plane pairs is shown in Figure 15. As shown in Figure 15, the variations of two design parameters affect the resonant frequency of each plane pair, and therefore makes it difficult to estimate the shape of the frequency response. In Figure 15, the maximum deviation of 10^{-2} calculated as the maximum RMS error between the original data and the scalable macromodel at each frequency point demonstrates the accuracy of the scalable macromodel.

To further evaluate the accuracy of the scalable macromodel at an intermediate design point, the frequency response of the plane pair with width of 1.750in and dielectric thickness of 1.8mil was calculated. The result is shown in Figure 16. The maximum RMS error in Figure 16 occurs at the resonant frequency resulting in an error of 1.0 percent as compared to the original frequency response, which was calculated using the cavity resonator model. This result demonstrates the accuracy

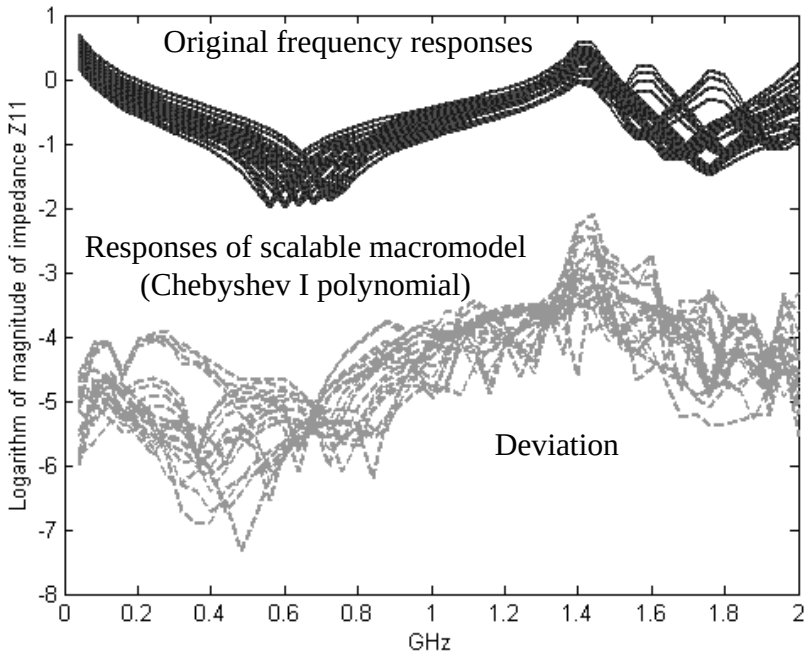

Figure 15: Frequency response of a power plain pair with two design parameters

of the scalable macromodel. The macromodeling method discussed captures resonances accurately and is relevant for developing design libraries for embedded passive components in multilayer configurations.

2.3 Selective Sampling

The electromagnetic behavior of embedded passive devices having many design parameters can be extracted using an electromagnetic simulation or from measurements. If an electromagnetic simulator is used to construct the scalable macromodel, the number of sampling points (which is a function of frequency and design variables) required to represent the electromagnetic behavior of the device becomes an important consideration. Since full wave electromagnetic simulations are often computationally expensive for generating the frequency response over a large frequency bandwidth, methods that minimize the number of simulations are required. This is especially true for devices requiring fine mesh size. Similarly, if a scalable macromodel is constructed

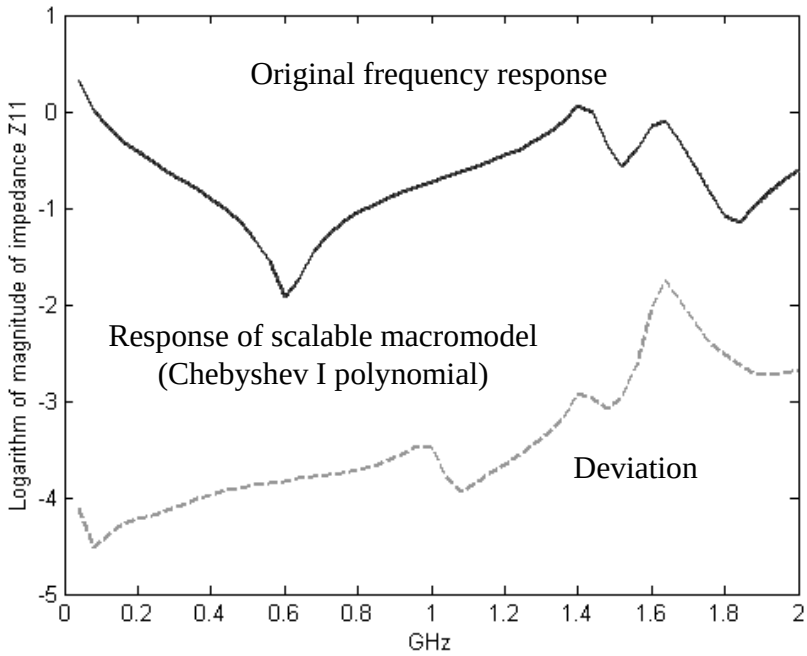

Figure 16: Performance of the scalable macromodel having width of 1.750in and thickness of 1.8mil

from measurements, test vehicles having several embedded passive devices are necessary. At the same time, systematic design variations are required for minimizing the fabrication cost of test vehicles.

Therefore, a selective sampling method shown in Figure 17 has been developed in this dissertation, which iteratively selects the values of the parameters used to construct the scalable macromodel. The method is described below:

1. The process begins with two groups $G1$ and $G2$ having different sampling points (frequency and design variables) in the computational domain. Then, two multidimensional rational functions $H1$ and $H2$ are used to approximate the two groups $G1$ and $G2$, respectively.

2. Frequency responses $R1$ and $R2$ are then computed using the two multidimensional rational functions $H1$ and $H2$ in the computational domain, respectively. According to the error criterion, the maximum deviation point between the

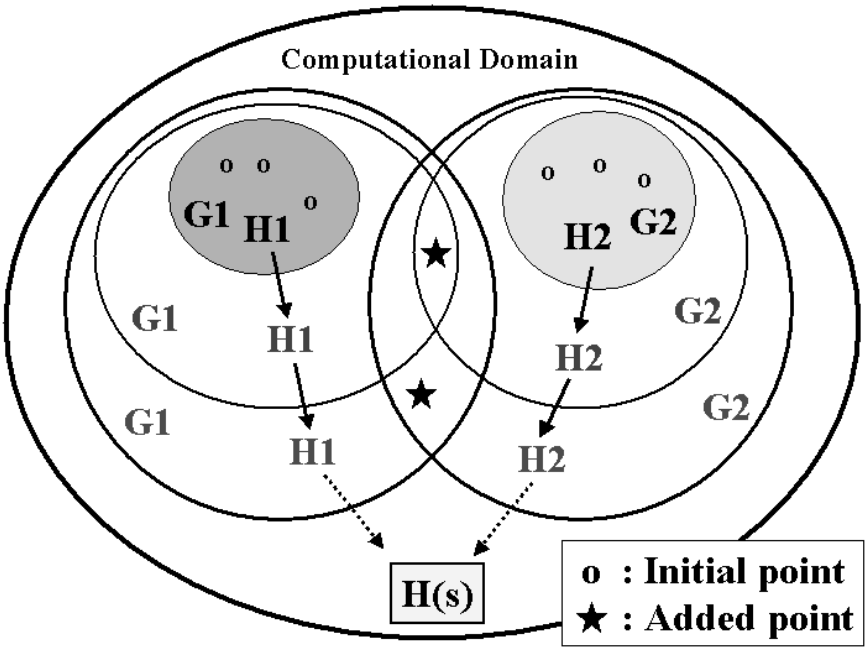

Figure 17: Selective sampling

responses $R1$ and $R2$ is chosen as the next sampling point. In this implementation, the RMS error is used as the error criterion. The new sampling point is then included in the two groups $G1$ and $G2$, and the multidimensional functions $H1$ and $H2$ are recalculated.

3. The algorithm repeats step 2 until the error criterion is satisfied over the entire range of variables.

In general, it is recommended that the initial sampling points be distributed over the computational domain and the number of sampled points can be arbitrarily chosen for constructing two distinct functions.

2.3.1 Test Case 1: Frequency response of a power plane pair

For demonstrating the performance of the selective sampling method, it was applied to the power plane pair shown in Figure 12. Assume initially that the computational domain consists of 1000 frequency points, which are uniformly distributed from 10.0

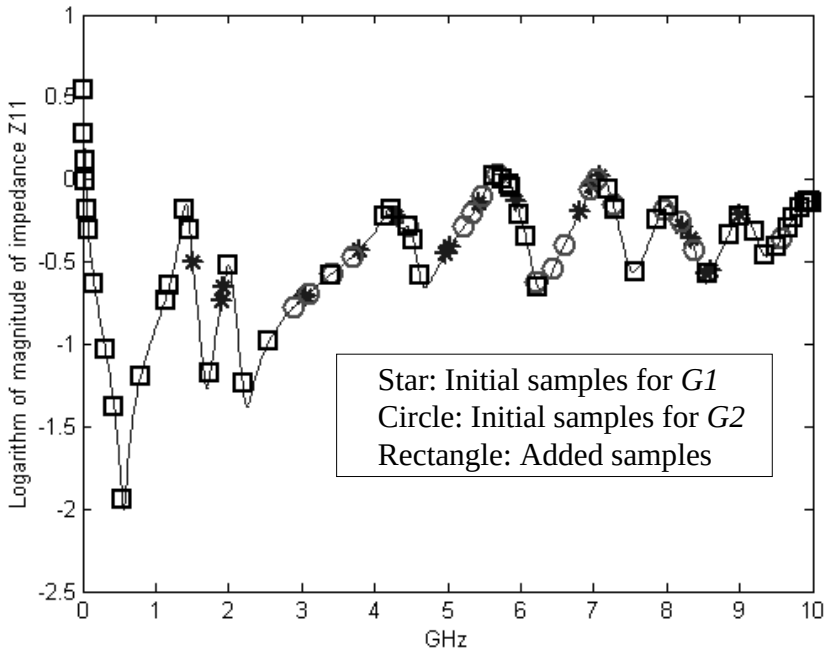

Figure 18: Frequency samples of two groups $G1$ and $G2$

MHz to 10.0 GHz in 10.0 MHz interval. Initially, two groups $G1$ and $G2$ having 20 different frequency samples each were selected. These points were randomly distributed. Then, two rational functions $H1$ and $H2$ based on the Legendre polynomial having order $NS = DS = 30$ were used to approximate the two groups $G1$ and $G2$, respectively.

Figure 18 shows the frequency samples of the two groups $G1$ and $G2$. The 20 stars and 20 circles in the figure represent the initial frequency samples for two groups $G1$ and $G2$, respectively, and the rectangle represents the additional 50 frequency samples generated through the selective sampling method.

During the iteration process, the maximum deviation (RMS error) between the responses $R1$ and $R2$ is shown in Figure 19. Since the method converges to the final solution after 50 iterations, it only requires 90 frequency samples instead of 1000 frequency samples that would otherwise be required. This results in a speed up of 11.

Figure 20 shows the original frequency response (solid line) of the power plane

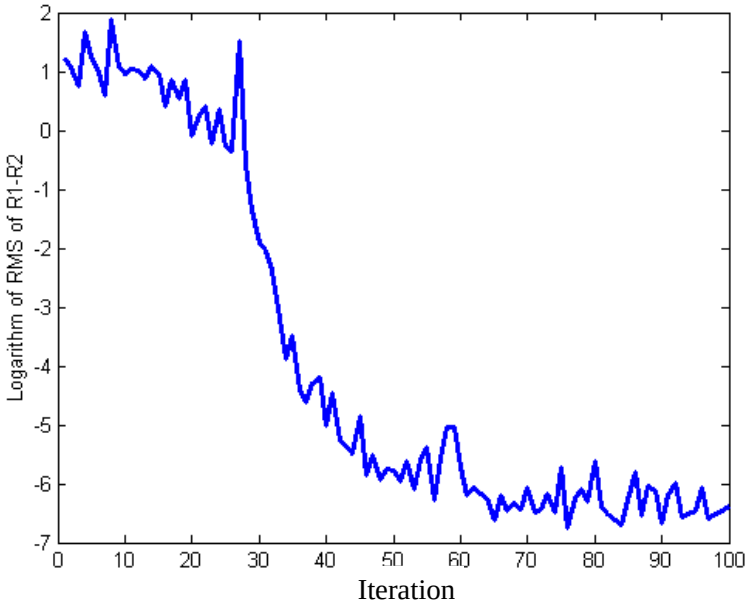

Figure 19: Maximum deviation between two frequency responses vs. the number of iterations

pair, the frequency response (dotted line) generated from the rational function, and the deviation (dashed line), which demonstrates the accuracy of the selective sampling method.

2.3.2 Test Case 2: Power plane pair with two design parameters

Consider the power plane pair shown in Figure 12, which has two design variables, namely, the width and dielectric thickness. The computational domain is the same as the domain used in Section 2.2.1, which has 5 variations for plane width (1200mil to 2000mil in 200mil increment), 4 variations for dielectric thickness (1.5mil to 3.0mil in 0.5mil increment), and 50 uniform frequency samples (40.0 MHz to 2.0 GHz) for each combination of design parameters. Hence, the number of samples required to generate the data is 1000 ($5 \times 4 \times 50$).

Two groups $G1$ and $G2$ having 20 different frequency samples per group were

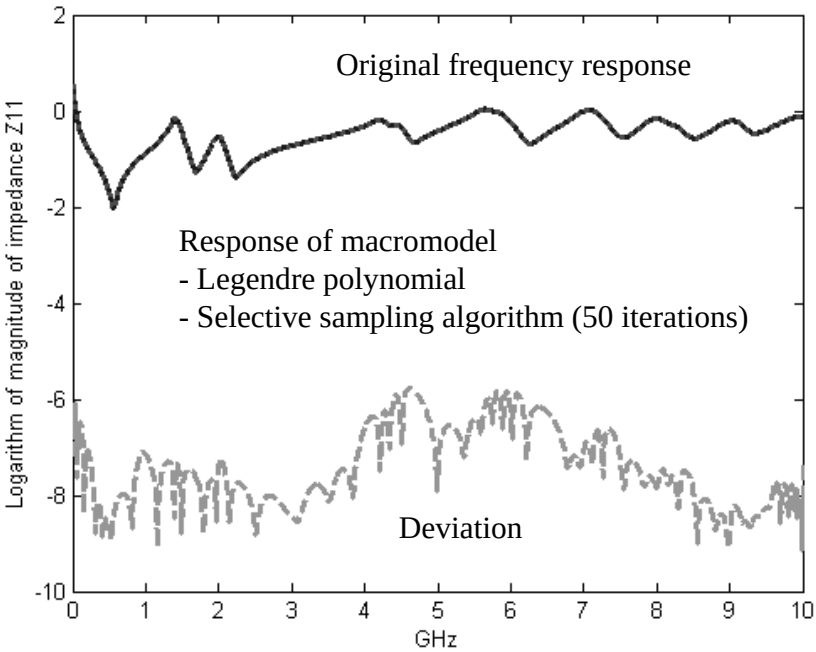

Figure 20: Comparison between the original response and the response of rational functions

randomly generated using the cavity resonator model and distributed over the computational domain. Using the scalable macromodel having estimated orders $NS = 10$, $DS = 10$, $N1 = 2$, $D1 = 2$, $N2 = 2$, $D2 = 2$ in Equation (2.8), the frequency response was approximated. Two scalable macromodels were developed using Chebyshev II polynomials, which were used to approximate the two groups $G1$ and $G2$, respectively.

Figure 21 shows the maximum deviation (RMS error) between the responses $R1$ and $R2$ of the two scalable macromodels $H1$ and $H2$ during the iteration of the selective sampling method. Since the method converges to the final solution after 200 iterations, it only requires 240 frequency samples instead of 1000 frequency samples. A speed up of 4 was therefore achieved.

The comparison between the original frequency response and the response of the scalable macromodel is shown in Figure 22. For evaluating the performance of

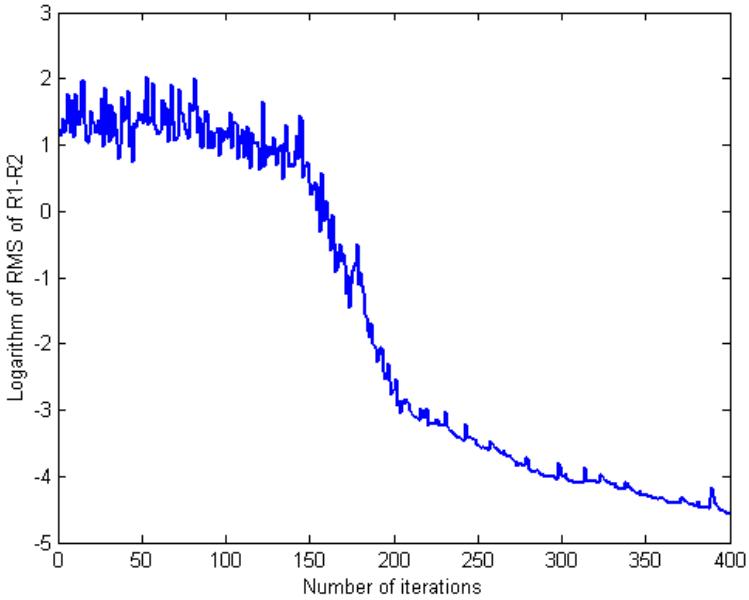

Figure 21: Maximum deviation between two frequency responses vs. the number of iterations

the scalable macromodel, the frequency response of the power plane pair with width of 1.750inch and thickness of 1.8mil, which was not included during the construction of the macromodel, was compared with the response of the macromodel, as shown in Figure 23. The maximum RMS error is less than $10^{-1.6}$.

2.4 Embedded Inductors

The everlasting trend in mobile wireless electronic systems requires the integration of digital and microwave circuits into the chip, package and/or board. One of the most challenging tasks in this trend is the integration of off-chip passive devices such as capacitors and inductors, which use up a lot of real estate, consume large electrical power and require additional manufacturing cost. This resulted in the development of embedded passive components in multilayer configurations, which can reduce the physical size and manufacturing cost and provide a good alternative to surface mount components for high-density integration [1].

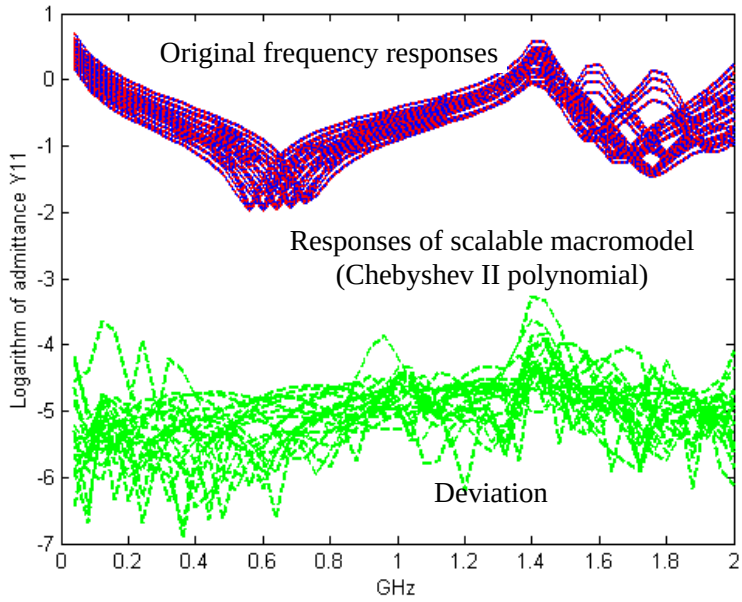

Figure 22: Frequency response of power plane pair with two design parameters

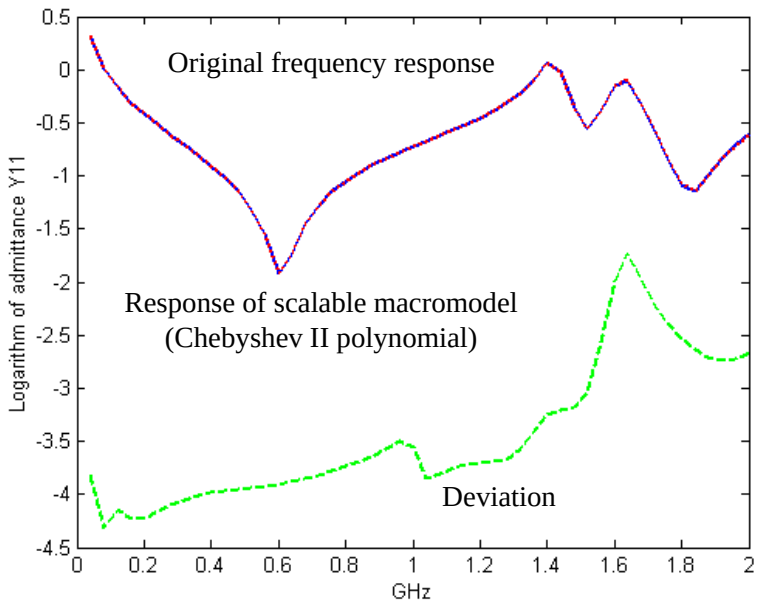

Figure 23: Performance of the scalable macromodel having width=1.750in and thickness=1.8mil

Although some empirical models of passive devices are available in RF design tools such as Advanced Design System (ADS) [63], these models are inaccurate for new technologies. This is because of the parasitic effects associated with embedded passive inductors and capacitors. One of the goals in this dissertation is to develop scalable electrical models for embedded inductors fabricated using printed wiring board (PWB) based technologies. To achieve this goal, the methods discussed in the previous sections have been used for building design libraries. In the following sections, scalable macromodels from electromagnetic simulations and measurements have been constructed.

2.4.1 Scalable Macromodels from Electromagnetic Simulation

In this section, scalable macromodels were constructed from the frequency response of embedded rectangular spiral inductors extracted from electromagnetic simulations. It was assumed that the inductors were designed on the board with two metal layers and an ideal ground plane, as shown in Figure 24(a). The board with thickness of 40mil had a dielectric constant, $\epsilon_r = 3.7$, and loss tangent, $tan\delta = 0.02$. The dielectric material with thickness of 1mil between the first and second layers has a dielectric constant, $\epsilon_r = 3.3$, and loss tangent, $tan\delta = 0.015$. It has been assumed that the metal layers have zero thickness and are lossless. The top view of the inductor is also shown in Figure 24(b). The center point of the inductor is connected to the ground layer through vias.

The inductors have two design parameters, namely, inner diameter distance (12mil to 92mil with 8mil increments) and number of turns (1 to 6) with fixed conductor width (4mil) and conductor spacing (4mil). With the area of the inductor fixed at less than $\leq 160 \times 160[mil^2]$, the 36 inductors shown in Table 2 were simulated to generate the frequency response (impedance parameter) using the electromagnetic

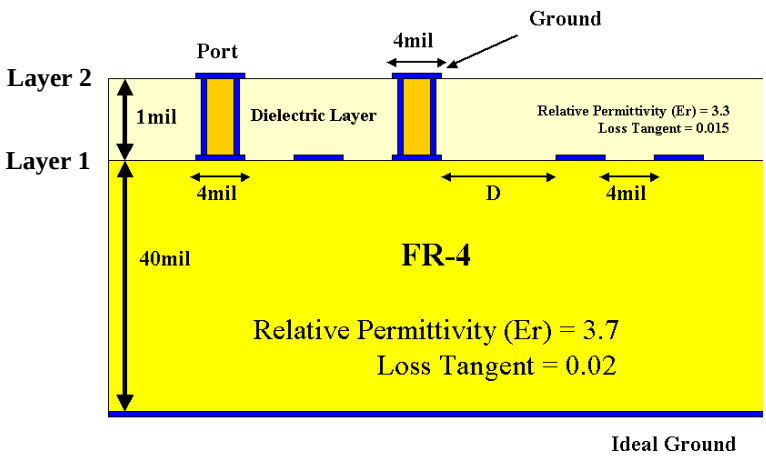

(a)

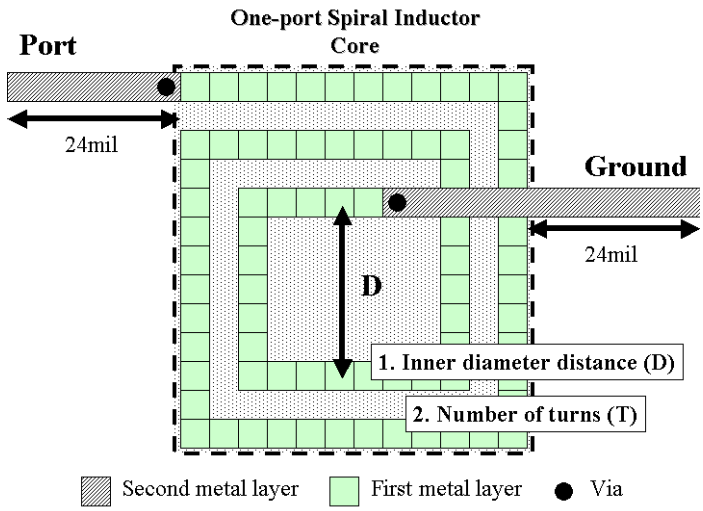

(b)

Figure 24: Embedded rectangular spiral inductor: (a) cross section and (b) top view

solver, SONNET [62]. The inductor with cross mark in Table 2 was reserved for evaluating the accuracy of the scalable macromodel. If 249 frequency samples per device that are randomly generated from 0.05GHz to 5.0GHz are required to extract the electromagnetic behavior of the inductors, a total of 8964 frequency samples would be required for construction of the scalable macromodel.

Table 2: Embedded rectangular spiral inductors

Diameter \ Turn	1	2	3	4	5	6
12 [mil]	o	o	o	o	o	o
20 [mil]	o	o	o	o	o	
28 [mil]	o	o	o	o	o	
36 [mil]	o	o	o	o		
44 [mil]	o	o	o	o		
52 [mil]	o	o	o			
60 [mil]	o	x	o			
68 [mil]	o	o				
76 [mil]	o	o				
84 [mil]	o					
92 [mil]	o					

Two groups $G1$ and $G2$ having 100 different frequency samples were randomly computed over the computational domain using SONNET. The frequency response of 36 inductors was approximated using the scalable macromodel having estimated orders $NS = 6$, $DS = 6$, $N1 = 2$, $D1 = 2$, $N2 = 2$, $D2 = 2$. Two scalable macromodels based on Chebyshev I polynomials were used to approximate the two groups $G1$ and $G2$, respectively.

Figure 25 shows the maximum deviation (RMS error) between the responses $R1$ and $R2$ of the two macromodels $H1$ and $H2$ during the iteration of the selective sampling method. Since the method converges to the final solution after 90 iterations, it only requires 290 frequency samples instead of 8964 frequency samples. This resulted in a speed up of 30.

The comparison between the original frequency response and the response of

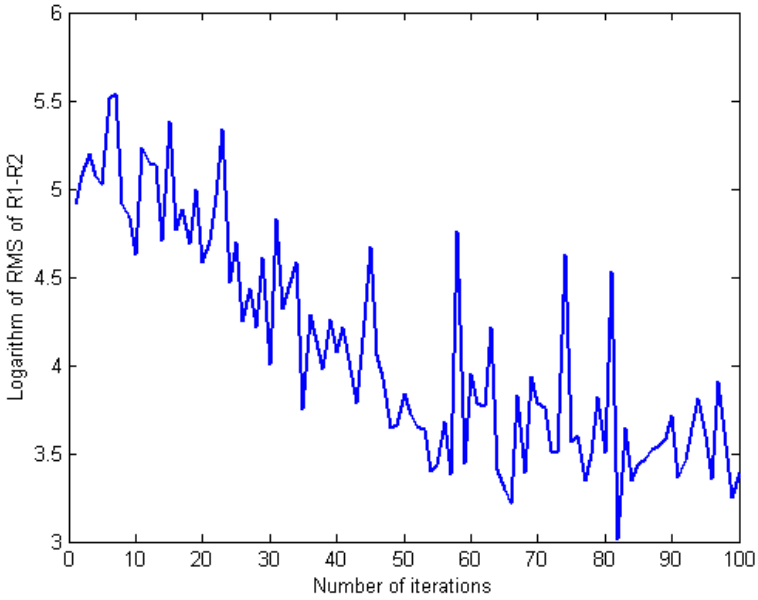

Figure 25: Maximum deviation between two frequency responses vs. number of iterations

the scalable macromodel constructed is shown in Figure 26, indicating the accuracy of the scalable macromodel. From the figure, the resonant peaks have been successfully captured. For evaluating the accuracy, the original frequency response of the embedded inductor with inner diameter distance (60mil) and number of turn (2), which was not included during the construction of the scalable macromodel, was compared with the response of the macromodel, as shown in Figure 27.

2.4.2 Scalable Macromodels from Measurements

For building design libraries of embedded inductors from measurements, over 150 spiral embedded inductors with design variations were designed and fabricated on standard organic substrate using low-cost laminate technology at the Packaging Research Center [58]. The cross section for the test vehicle is shown in Figure 28.

As illustrated in Figure 2.19, the embedded circular spiral inductors were designed on FR-4 board that consisted of two metal layers with a floating metal

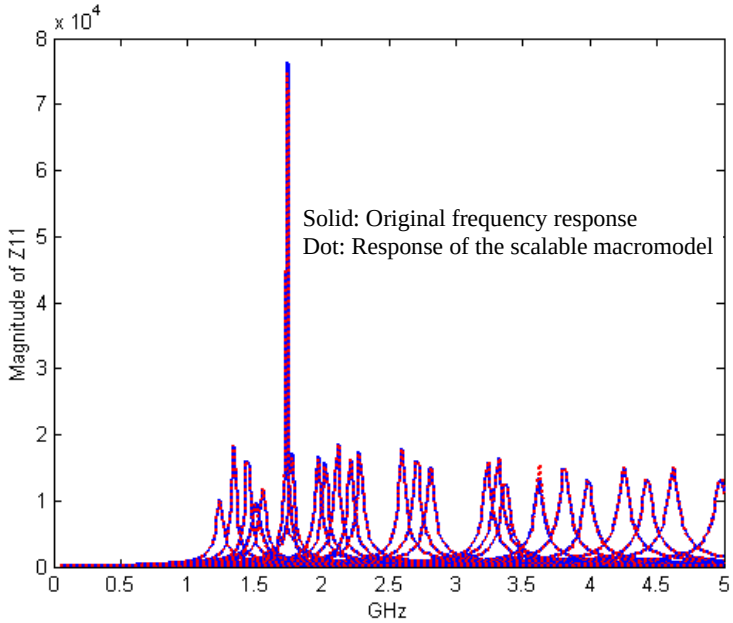

Figure 26: Frequency response of embedded inductors with two design parameters

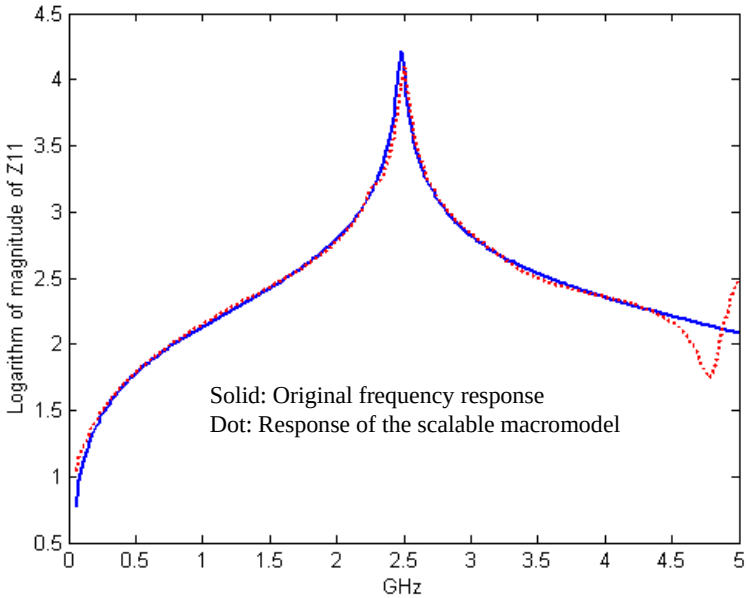

Figure 27: Performance of the scalable macromodel having inner diameter of 60mil and number of turns of 2

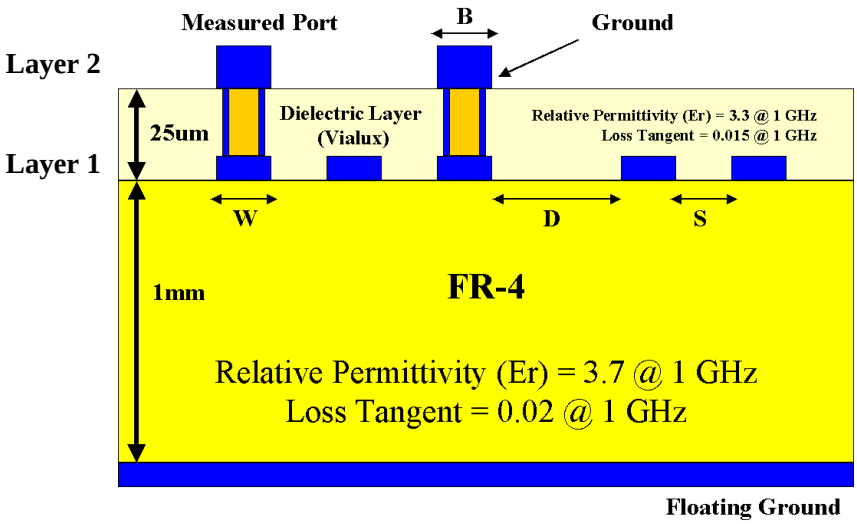

Figure 28: Cross-section of the test vehicle

layer. The dielectric material between the first and second layers is a $25\mu m$ thick Vialux material with a relative permittivity, $\epsilon_r = 3.3$ @ 1.0 GHz, and loss tangent, $tan\delta = 0.015$ @ 1.0 GHz. The dielectric material between the second and third layers is a 1mm thick FR-4 layer cladded with copper of $9\mu m$ thickness with a relative permittivity, $\epsilon_r = 3.7$ @ 1.0 GHz, and loss tangent, $tan\delta = 0.02$ @ 1.0 GHz.

The fabrication process of the device is described as follows:

1. A 1mm thick, copper cladded (9um) FR-4 organic substrate (epoxy-glass fiber composite) was used.

2. A 15um thick photoresist dry film was laminated on the substrate (@ $75°C$) using a vacuum pressure type laminator and then patterned.

3. The first conductor coil layer was patterned by copper etching.

4. The photoresist was then stripped off and a 25um thick photosensitive dielectric epoxy dry film was laminated using a vacuum pressure type laminator to

insulate the conductor coil layer.

5. Photo-via openings were then formed through exposure to ultra violet (UV) light, pre-baking in oven at $110°C$ for 1.0hr, developing in gamma-butyro lactone, and curing the dielectric polymer at $150°C$ (the maximum temperature used in this process) for 1.5hr.

6. The vias and the upper conductor lines were then formed through copper seeding by electroless plating followed by electrolytic copper plating into the photoresist mold made through lamination.

7. For electroless copper plating, the surface of dielectric polymer was catalyzed through such process steps as swell, etch, neutralize, pre-catalyst, and catalyst.

8. After plating, the photoresist was stripped off and the copper seed layer was wet-etched in micro-etch solution.

The top view of a one-port embedded spiral inductor is shown in Figure 29. The ground ring of the inductor is on the second metal layer and the core of the spiral embedded inductor is embedded on the first layer. The center of the inductor on the first layer is connected to the ground ring though the photo-via and the bridge on the first layer. The embedded spiral inductors fabricated in this dissertation were designed with geometrical variations except for the width of the ground ring (24mil) and the width of the bridge connecting the ground ring to the center of the inductor (6mil). As shown in Figure 3, the design variations are conductor width (W), conductor spacing (S), inner diameter distance (D), width of bridge (B), via diameter distance (V), and number of turns (N). In addition to the variations in the core of the inductor, the additional design variations shown in Figure 29 are vertical distance (GV) and lateral distance (GH) between the ground ring and the core of the inductor.

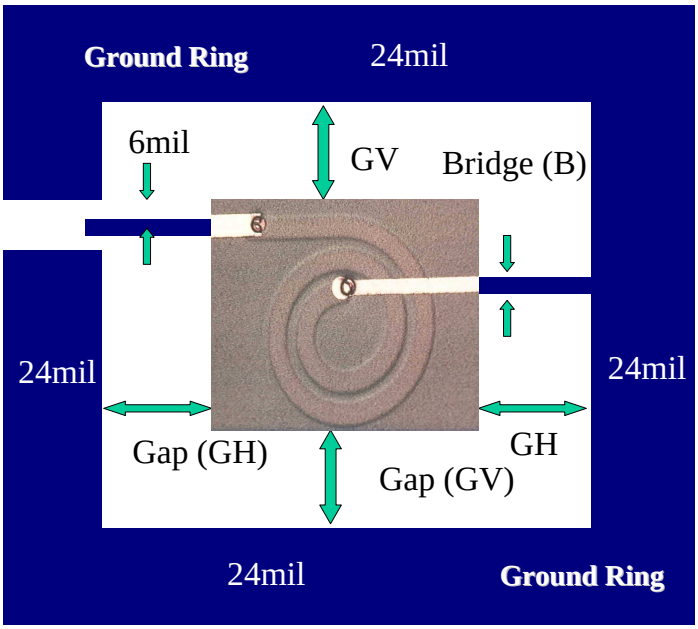

Figure 29: Top view of the inductor

Among several kinds of embedded circular spiral inductors in the test vehicle, inductors with fixed conductor width (6mil) and conductor spacing (6mil) were considered. The design variables of the inductors were inner diameter distance (16mil to 80mil with 16mil increments) and number of turns (1 to 5). The 15 inductors with circle and cross marks shown in Table 3 were designed and measured for extracting the frequency response using HP8720ES vector network analyzer and Cascade Microtech ground-signal-ground microwave probe. Network analyzer calibration was done using short-open-load calibration standards. The one-port S-parameters were recorded from 0.1GHz up to 10GHz.

For the construction of the scalable macromodel, the 14 inductors with circles in Table 3 were used. If 1601 frequency samples per device distributed from 0.05GHz to 10.0GHz with 198MHz interval are required to extract the electromagnetic behavior of the inductors, a total of 22414 frequency samples would be required for the construction of design libraries of the inductors with two design variables.

Table 3: Embedded circular spiral inductors

Diameter \ Turn	1	2	3	4	5
16 [mil]	o	o	o	o	o
32 [mil]	o	o	o	o	
48 [mil]	o	o	o		
64 [mil]	x	o			
80 [mil]	o				

For initializing the selective sampling method, two groups $G1$ and $G2$ having 20 different frequency samples per group were randomly selected over the computational domain. Then, the frequency response of 14 inductors was approximated using the scalable macromodel having estimated orders $NS = 10$, $DS = 10$, $N1 = 2$, $D1 = 2$, $N2 = 2$, $D2 = 2$. Two scalable macromodels were developed using Chebyshev I polynomials, which were used to approximate the two groups $G1$ and $G2$, respectively.

Figure 30 shows the maximum deviation (RMS error) between the responses $R1$ and $R2$ of the two scalable macromodels $H1$ and $H2$ during the iteration of the selective sampling method. Since the error continued to decrease, 500 iterations was selected as the final iteration and the method required 540 frequency samples instead of 22414 frequency samples. A speed up of 41 was therefore achieved.

The comparison between the original frequency response and the response of the scalable macromodel constructed is shown in Figure 31, indicating the accuracy of the scalable macromodel. From the figure, the resonant peaks were successfully captured. For evaluating the performance of the scalable macromodel, the frequency response of the embedded inductor with inner diameter distance (64mil) and number of turns (1), which was not included during the construction of the scalable macromodel, was compared with the response of the scalable macromodel as shown in Figure 32.

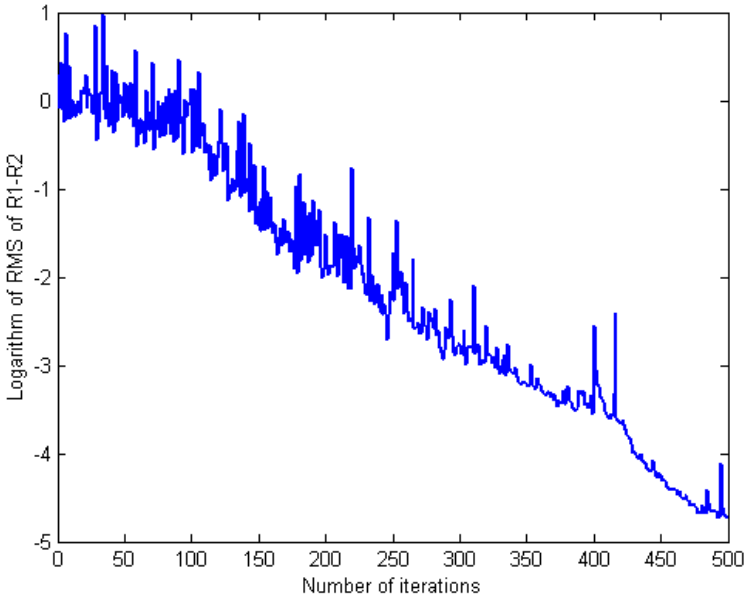

Figure 30: Maximum deviation between two frequency responses vs. number of iterations

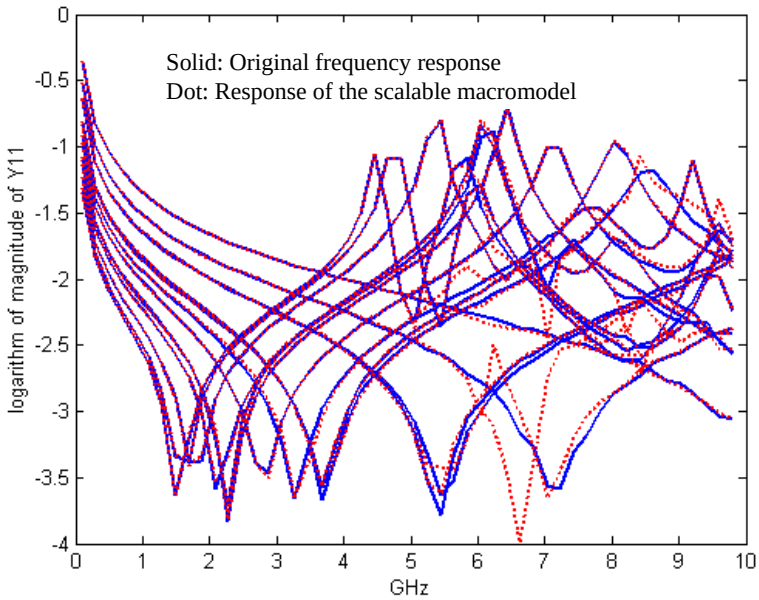

Figure 31: Frequency response of embedded inductors with two design parameters

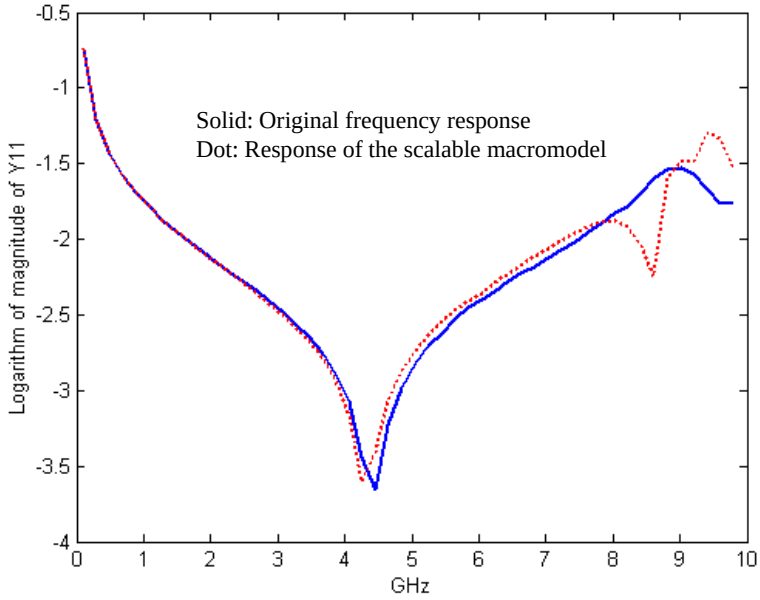

Figure 32: Performance of the scalable macromodel having inner diameter of 64mil and number of turns of 1

2.5 Summary

In this chapter, the power series expansion was replaced with orthogonal polynomials for increasing the accuracy of the scalable macromodel. The orthogonal polynomials implemented in this chapter were Legendre, Chebyshev I, and Chebyshev II polynomials. For building design libraries of embedded passive devices, the scalable macromodel based on multidimensional rational functions was implemented as a multiplication of one-dimensional rational functions having frequency and design parameters. For reducing the number of frequency samples, a selective sampling method was developed.

For demonstrating the performance of the methods proposed in this dissertation, a rectangular power plane structure with two design variations was used. This was also applied to build design libraries of embedded spiral inductors using an electromagnetic simulator and from measurements. The selective sampling method discussed in this chapter provided a method for reducing the sampling points required.

This reduced the computational time, which was demonstrated using numerous examples.

CHAPTER III

PASSIVE MACROMODELS

For time-domain simulation, the macromodel used for capturing the electromagnetic behavior of passive devices needs to satisfy three conditions, namely, 1) the macromodel has to use real coefficients, 2) the macromodel should be stable, and 3) the macromodel needs to be passive. The first condition has been satisfied in this dissertation by construction and the second condition has been satisfied by removing unstable poles located in the right half of the s-plane and prohibiting multiple poles along the imaginary axis of the s-plane. For checking and enforcing passivity of the macromodel, this chapter presents multiport passivity formulae, which have been analytically derived from the pole-residue form of the rational function. Using filter theory, a generalized pole-residue form of filters has been derived and the properties of filters are presented. Finally, this chapter presents the properties and limitations of the multiport passivity formulae followed by the synthesis of passive macromodels for time-domain simulation.

3.1 Filters

Using filter theory, the rational function $H(s)$ can be represented as a summation of filters as:

$$H(s) = \sum_m H_{LP}^m(s) + \sum_n H_{BP}^n(s) + \sum_k H_{HP}^k(s) + \sum_r H_{AP}^r(s) \tag{3.1}$$

where $H_{LP}^m(s)$, $H_{BP}^n(s)$, $H_{HP}^k(s)$, $H_{AP}^r(s)$ represent low pass, band pass, high pass and all pass filters, respectively. The term "filter" is defined as a rational function generating a specific frequency response over a certain frequency band. The filters shown in Equation (3.1) represent a complete set for representing any transfer function.

It is important to note that there are two types of roots of the polynomial in Equation (1.1), namely, real and complex roots. It is assumed that the root is simple (or non-overlapping) in this dissertation. Based on the constraint of real coefficients for the rational functions, the complex roots must always occur in complex conjugate pairs. Therefore, combining the pole-residue form in Equations (1.4) and (3.1) results in:

$$\begin{aligned} H(s) = & \sum_{m=1}^{LPN} \frac{r_m}{s - p_{mr}} \\ & + \sum_{n=1}^{BPN} \frac{\alpha_n + j\beta_n}{s - p_{nr} - jp_{ni}} + \frac{\alpha_n - j\beta_n}{s - p_{nr} + jp_{ni}} \\ & + \sum_{k=1}^{HPN} \frac{\psi_k s}{s - p_{kr}} \\ & + \delta + \eta s \end{aligned} \tag{3.2}$$

where the coefficients p_{mr}, r_m, p_{nr}, p_{ni}, α_n, β_n, p_{kr}, ψ_k, δ, η are real and the superscripts LPN, BPN, HPN are the number of low pass, band pass and high pass filters, respectively. By combining the complex conjugate poles, Equation (3.2) can be rewritten as:

$$\begin{aligned} H(s) = & \sum_{m=1}^{LPN} \frac{r_m}{s - p_{mr}} \\ & + \sum_{n=1}^{BPN} \frac{2\alpha_n(s - p_{nr}) - 2\beta_n p_{ni}}{(s - p_{nr})^2 + p_{ni}^2} \\ & + \sum_{k=1}^{HPN} \frac{\psi_k s}{s - p_{kr}} \\ & + \delta + \eta s \end{aligned} \tag{3.3}$$

Hence, Equation (3.1) can be rewritten as a summation of filters shown in Equation (3.3). The low pass filter H_{LP}^m consists of a real pole p_{mr} with its residue r_m; the band pass filter H_{BP}^n consists of a complex conjugate pole pair $p_{nr} \pm jp_{ni}$ with its corresponding residues $\alpha_n \pm j\beta_n$; the high pass filter H_{HP}^k consists of a real pole

p_{kr} with its residue ψ_k; and the all pass filter H^r_{AP} consists of residues, δ and η. It is important to note that the coefficients of filters in Equation (3.3) are all real.

Equation (3.3) can be generalized for a distributed multiport network containing common poles as:

$$\begin{aligned}[H(s)] = & \sum_{m=1}^{LPN} \frac{[\gamma_m]}{s - p_{mr}} \\ & + \sum_{n=1}^{BPN} \frac{2[\alpha_n](s - p_{nr}) - 2[\beta_n]p_{ni}}{(s - p_{nr})^2 + p_{ni}^2} \\ & + \sum_{k=1}^{HPN} \frac{[\psi_k]s}{s - p_{kr}} \\ & + [\delta] + [\eta]s \end{aligned} \tag{3.4}$$

where the matrices $[\alpha_n]$, $[\beta_n]$, $[\gamma_m]$, $[\psi_k]$, $[\delta]$, $[\eta]$ are PxP residue matrices for a P-port network.

3.2 Properties of Filters

This section shows the relationship between the frequency response and the coefficients of the rational function. Specifically, the low pass and band pass filters are considered in this section since the response of the high pass filter is similar to the response of the low pass filter and the response of the all pass filter is simply a constant or linear line in the frequency response.

It is assumed that the low pass filter in Equation (3.3) consists of a real pole p_r and its residue r. The frequency response (admittance) of the low pass filter is shown in Figure 33. The properties of the low pass filter are discussed below:

1. As shown in Figure 33(a), the real part p_r of a real pole for a fixed residue $r = 200$ determines the slope of the frequency response.

2. As the absolute value of the real part p_r of the real pole becomes smaller, the frequency response becomes sharper near the low frequency range.

3. The residue r for a fixed pole $p_r = -2.0e^6$ (say) determines the amplitude of the frequency response and the sign of the real part of the frequency response, as shown in Figure 33(b).

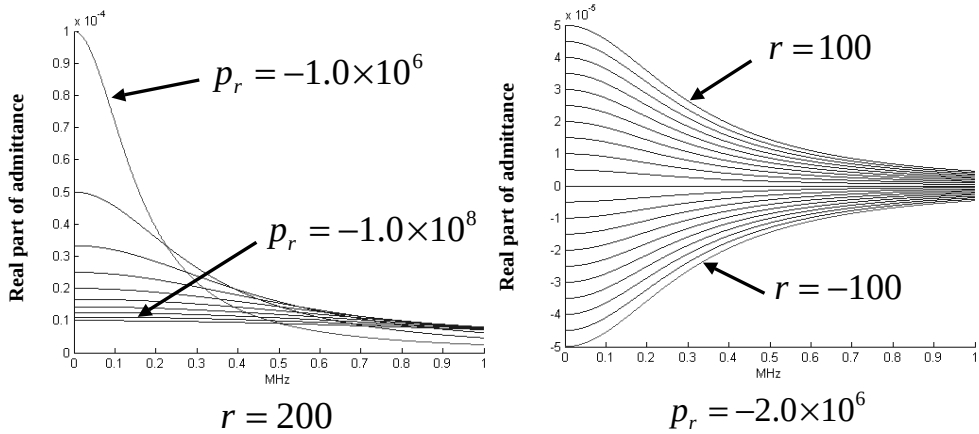

Figure 33: Frequency response for a low pass filter: (a) real part of a real pole for a fixed residue and (b) real part of a real residue for a fixed pole

Similarly, the frequency response of the band pass filter in Equation (3.3) is shown in Figure 34. It is assumed that the band pass filter in Equation (3.3) consists of a complex conjugate pole pair $p_r \pm jp_i$ and its corresponding residues $\alpha \pm j\beta$. In Figure 34, the frequency response has been plotted by varying one parameter while the other parameters are kept fixed. The properties of the band pass filter are discussed below:

1. In Figure 34(a), the real part p_r of the poles determines the slope and sharpness of the frequency response.

2. In Figure 34(b), the imaginary part p_i of the poles determines the resonating frequency.

3. In Figure 34(c), the real part α of the residues determines the amplitude and sign of the real part of the frequency response.

4. In Figure 34(d), the imaginary part β of residues determines the shape and sign of the real part of the frequency response.

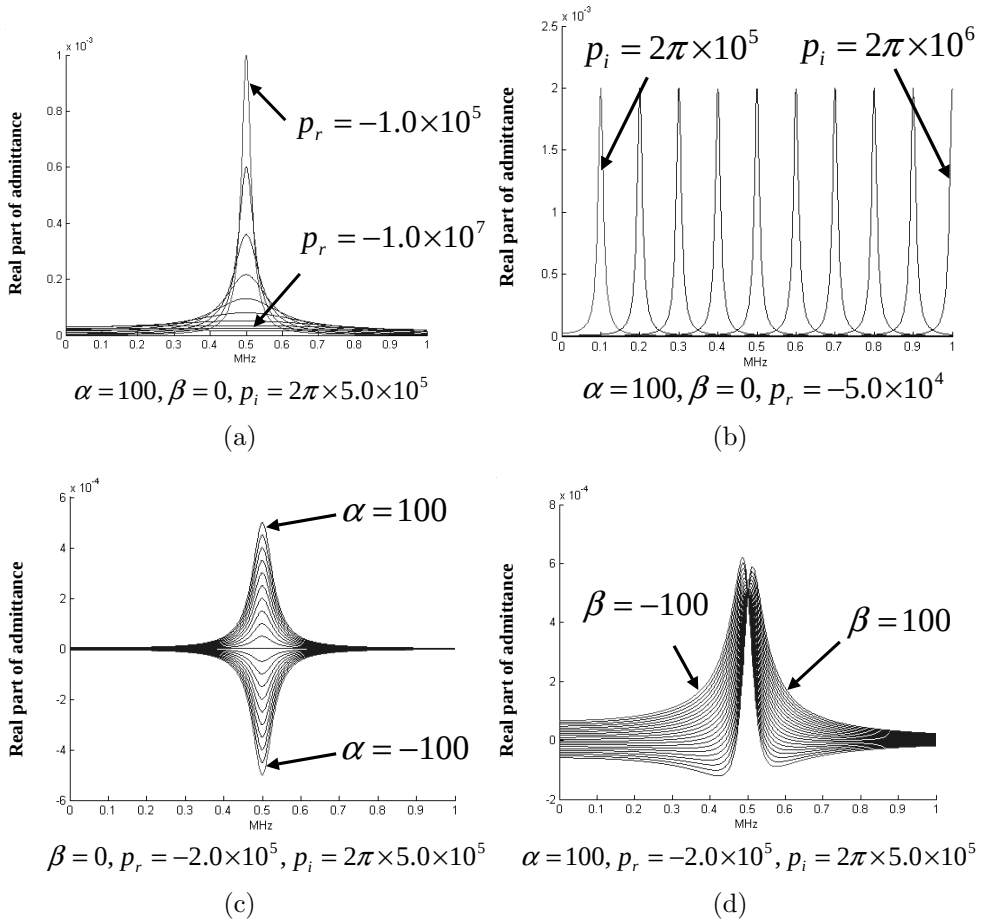

Figure 34: Frequency response for a band pass filter: (a) varying p_r for fixed coefficients p_i, α, β, (b) varying p_i for fixed coefficients p_r, α, β, (b) varying α for fixed coefficients β, p_r, p_i, and (b) varying β for fixed coefficients α, p_r, p_i

3.3 Multiport Passivity Formulae

Based on the maximum modulus theorem [60], the passivity condition for a one-port network can be written as:

$$Re\{H(s = j\omega)\} \geq 0 \quad \forall\omega \tag{3.5}$$

It is important to note that $s = j\omega$ in Equation (3.3) (and not $s = \sigma + j\omega$) simplifies the derivation of the analytical formulae for satisfying passivity of the macromodel. The basic idea behind the construction of passive macromodels for a passive system is that the summation of passive sub-networks is always passive. The rational function $H(s)$ in Equation (3.3) can be regarded as a summation of passive sub-networks consisting of low pass, band pass, high pass and all pass filters. If every sub-network in Equation (3.3) satisfies the passivity condition, the rational function $H(s)$ satisfies the passivity condition as well.

Substituting $s = j\omega$ into Equation (3.3), the rational function $H(s = j\omega)$ can be separated into the real and imaginary parts as:

$$H(s = j\omega) = H_R(j\omega) + jH_I(j\omega) \tag{3.6}$$

By regrouping terms, the real $H_R(s = j\omega)$ and imaginary $H_I(s = j\omega)$ parts of the rational function can be written as:

$$\begin{aligned} H_R(j\omega) = & \sum_{m=1}^{LPN} \frac{-\gamma_m p_{mr}}{p_{mr}^2 + \omega^2} \\ & + \sum_{n=1}^{BPN} \frac{2\omega^2(-\alpha_n p_{nr} + \beta_n p_{ni})}{\left(p_{nr}^2 + p_{ni}^2 - \omega^2\right)^2 + \left(2p_{nr}\omega\right)^2} \\ & + \sum_{n=1}^{BPN} \frac{2(p_{nr}^2 + p_{ni}^2)(-\alpha_n p_{nr} - \beta_n p_{ni})}{\left(p_{nr}^2 + p_{ni}^2 - \omega^2\right)^2 + \left(2p_{nr}\omega\right)^2} \\ & + \sum_{k=1}^{HPN} \frac{\psi_k \omega^2}{p_{kr}^2 + \omega^2} \\ & + \delta \end{aligned} \tag{3.7}$$

$$
\begin{aligned}
H_I(j\omega) = \omega &\sum_{m=1}^{LPN} \frac{-\gamma_m}{p_{mr}^2 + \omega^2} \\
+ \omega &\sum_{n=1}^{BPN} \frac{2\alpha_n(-p_{nr}^2 + p_{ni}^2 - \omega^2)}{\left(p_{nr}^2 + p_{ni}^2 - \omega^2\right)^2 + \left(2p_{nr}\omega\right)^2} \\
- 4\omega &\sum_{n=1}^{BPN} \frac{\beta_n p_{ni} p_{nr}}{\left(p_{nr}^2 + p_{ni}^2 - \omega^2\right)^2 + \left(2p_{nr}\omega\right)^2} \\
- \omega &\sum_{k=1}^{HPN} \frac{\psi_k p_k}{p_{kr}^2 + \omega^2} \\
+ \omega\eta &
\end{aligned}
\tag{3.8}
$$

The passivity of each sub-network can be satisfied using one-port passivity formulae in Equation (3.9), which can be analytically derived from Equation (3.7) by satisfying the maximum modulus theorem in Equation (3.5).

$$
\begin{aligned}
\gamma_m &\geq 0 \\
-\alpha_n p_{nr} \pm \beta_n p_{ni} &\geq 0 \\
\psi_k &\geq 0 \\
\delta &\geq 0
\end{aligned}
\tag{3.9}
$$

For a multiport network, the rational function matrix $[H(s)]$ in Equation (3.4) has to be positive semi-definite at all frequencies according to the passivity constraints discussed in Chapter 1. Using the property of positive semi-definiteness, the one-port passivity formulae in Equation (3.9) can be extended to multiport passivity formulae as:

$$
\begin{aligned}
eigenvalues\ of\ \ [\gamma_m] &\geq 0 \\
eigenvalues\ of\ \ [-\alpha_n p_{nr} \pm \beta_n p_{ni}] &\geq 0 \\
eigenvalues\ of\ \ [\psi_k] &\geq 0 \\
eigenvalues\ of\ \ [\delta] &\geq 0
\end{aligned}
\tag{3.10}
$$

The following properties of multiport passivity formulae in Equation (3.10) are apparent during the construction of the passive macromodel. These properties

have been used for the construction of broadband passive macromodels in the next chapter.

1. The multiport passivity formulae only depend on the poles and residue matrices, which are independent of frequency. Hence, the passivity of the circuit is satisfied over infinite frequency.

2. The multiport passivity formulae are only enforced on each sub-network of $[H(s)]$, and there is no relationship for passivity between sub-networks except that they contribute to the overall frequency response of the macromodel. This makes the method simple to use.

3. For compensating negative eigenvalues in Eq. (3.11), there are two free matrix variables $[\alpha_n]$ and $[\beta_n]$ related to two free variables of complex conjugate poles $p_{nr} \pm jp_{ni}$, a free matrix variable $[\gamma_m]$ related to a real pole p_{mr}, a free matrix variable $[\psi_k]$ related to a real pole p_{kr}, and a free matrix variable $[\delta]$. These can be suitably changed.

3.4 Enforcing Passivity

The non-passive macromodel that does not satisfy the passivity condition needs to be appropriately modified so that the macromodel becomes passive. For enforcing passivity of the macromodel in this dissertation, fixed common poles and symmetric residue matrices are assumed during compensation. Figure 35 shows the procedure for compensating the non-passive macromodel using multiport passivity formulae.

If negative eigenvalues are obtained in the residue matrices $[\gamma]$, $[\psi]$, $[\delta]$ in Equation (3.10), negative eigenvalues are set equal to zero or changed to a small positive value and then a new residue matrix is reconstructed. If the passivity formulae for complex conjugate poles with two residue matrix variables $[\alpha]$ and $[\beta]$ are violated, negative eigenvalues of $[\alpha]$ are set equal to zero or changed to a small positive value

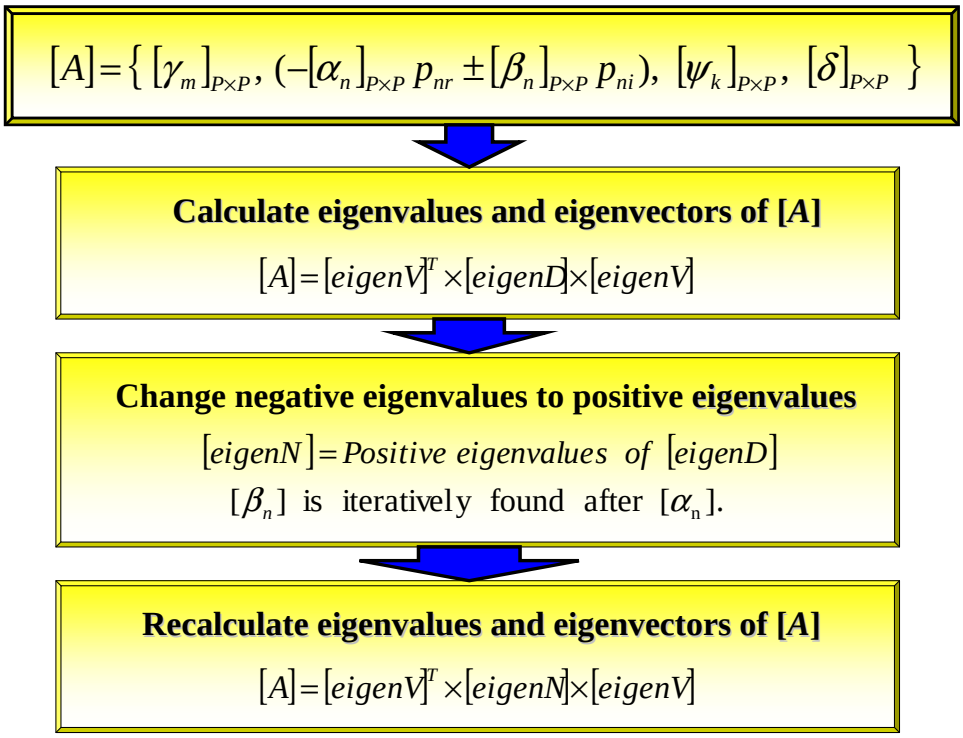

Figure 35: Enforcing passivity using multiport passivity formulae

and then a new residue matrix $[\alpha]$ is reconstructed. Based on the compensated matrix $[\alpha]$, the residue matrix $[\beta]$ is iteratively found for satisfying the passivity formulae in Equation (3.10). A small positive value is used to ensure that the macromodel does not violate the passivity condition even though this may cause small numerical errors in the solution. Figure 35 shows the procedure described in this section.

3.5 Discussion of Multiport Passivity Formulae

3.5.1 Residue Matrix $[\eta]$

In [23]-[47], several methods for checking and enforcing passivity of the macromodels have been discussed. However, it is important to note that these methods were based on scattering (S), admittance (Y), or impedance (Z) parameters. For discussion, this section begins by defining the transfer function $H(s)$ representing S, Y, or Z parameters as a scattering $S(s)$, admittance $Y(s)$, or impedance $Z(s)$ function, respectively.

For discussing the property of the residue matrix $[\eta]$ which can affect the stability and passivity of the network, assume that a one-port macromodel can be represented as an impedance function $Z(s) = R - Cs$, where R and C are positive numbers. It is obvious that the impedance parameter Z generated from the transfer function $Z(s)$ does not violate the maximum modulus theorem. Similarly, the admittance parameter $Y = 1/Z$ generated from the transfer function $Z(s)$ does not violate the maximum modulus theorem since the real part of the admittance parameter Y over infinite frequency bandwidth is always positive. However, it is important to note that after converting $Z(s)$ to $Y(s)$ using $Y(s) = 1/Z(s)$, the transfer function $Y(s) = 1/(R - Cs)$ is unstable since the pole is located in the right half of the s-plane due to the positive values R and C. This leads to a diverging time-domain waveform during transient simulation.

Consider another example where a one-port macromodel can be represented as an admittance function $Y(s) = -Cs$, where C is a positive number, and the macromodel is connected to a resistor $R_1 > 0$ and a resistor $R_2 > 0$, as shown in Figure 36.

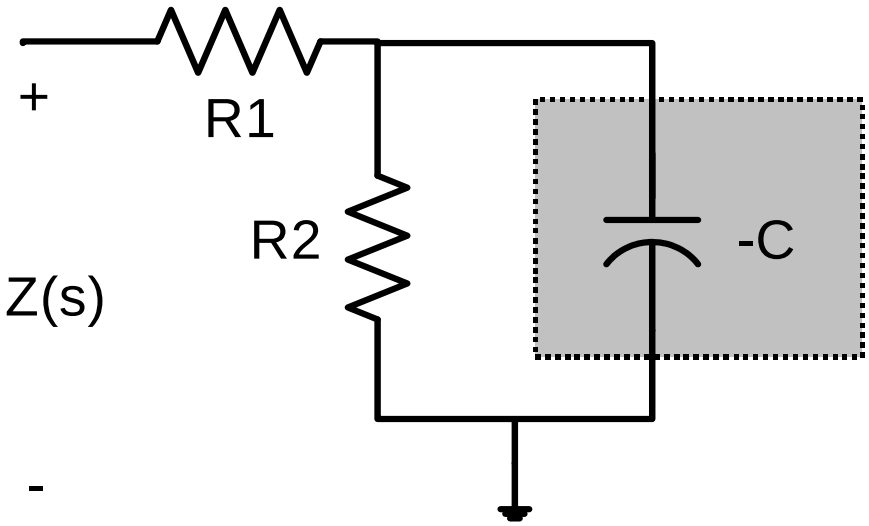

Figure 36: Unstable circuit

In Figure 36, the transfer function $Z(s)$ at the input port can be written as:

$$Z(s) = \frac{R_1 - sC(R_1R_2 + 1)}{1 - sR_2C} \tag{3.11}$$

which does not violate the maximum modulus theorem since the real part Z_R of $Z(s = j\omega)$ is

$$Z_R = \frac{R_1 + \omega^2 R_2 C^2 (R_1 R_2 + 1)}{1 + \omega^2 R_2^2 C^2} \tag{3.12}$$

which is always positive over infinite frequency bandwidth. However, the function $Z(s)$ violates the stability condition since C, R_1, and R_2 are all positive. Therefore, even though the frequency response of any transfer function does not violate the maximum modulus theorem, both examples considered violate the stability condition, which results in diverging waveform during transient simulation. Hence, if a method uses the parameters generated from the transfer function matrix $[H(s)]$ having a residue matrix $[\eta]$ for detecting the frequency bands having negative eigenvalues corresponding to the real part of the parameters, the method may enforce the passivity condition on the transfer function matrix, but not the stability condition. Therefore, it is important to revisit the definition of the stability condition.

Several methods in [60] based on the $S(s)$, $Y(s)$, or $Z(s)$ function matrix have been discussed for checking stability of the macromodel. The primary condition for stability is that the poles of $H(s)$ lie on the left half of the s-plane. This condition implies that the poles of both $Y(s)$ and $Z(s)$ lie on the left half of the s-plane. According to Talbot's test in [60], the poles of $S(s)$ become stable if the poles of both $Y(s)$ and $Z(s)$ are stable. The stability of the transfer functions $Y(s)$ and $Z(s)$ can be checked using the Hurwitz's test as described in [60]. Hence, the stability and passivity of the macromodel can be guaranteed using both the Hurwitz's test and maximum modulus theorem.

For discussion, assume that the rational function $H(s)$ can be written as

$H(s) = Q(s)/P(s)$, where $Q(s)$ and $P(s)$ are the numerator and denominator polynomial, respectively. It is important to note that $Y(s)$ and $Z(s)$ can both be represented using the same polynomial $Q(s) + P(s)$. For satisfying the stability condition, it is required that the polynomial $Q(s) + P(s)$ must be strict Hurwitz. If the roots of $P(s)$ and $Q(s)$ lie on the left half of the s-plane, the rational function satisfies the strict condition. The polynomial $Q(s) + P(s)$ is Hurwitz if the continued fractional expansion of the ratio of its even part polynomial to its odd part polynomial (or vice versa) yield coefficients that are all positive [60]. For instance, consider a rational function

$$H(s) = \frac{Q(s)}{P(s)} = \frac{s^2 + 2s + 3}{s^3 + s^2 + 2s + 3} \tag{3.13}$$

to determine if it is Hurwitz. The polynomial $L(s) = Q(s) + P(s)$ becomes

$$L(s) = Q(s) + P(s) = s^3 + 2s^2 + 4s + 6. \tag{3.14}$$

The fractional expansion $\varphi(s)$ of the ratio of the even part polynomial $E(s) = 2s^2 + 6$ to odd part polynomial $O(s) = s^3 + 4s$ becomes

$$\begin{aligned} \varphi(s) &= \frac{s^3 + 4s}{2s^s + 6} \\ &= \frac{1}{2}s + \frac{1}{2s + \frac{1}{\frac{1}{6}s}} \end{aligned} \tag{3.15}$$

Since the coefficients are all positive, the function is Hurwitz. Using the passivity formulae in Equation (3.9), consider the filters in Equation (3.3) to determine if they satisfy the Hurwitz condition.

- For the low pass filter, the polynomial $L(s) = s + \gamma_m - p_{mr}$ satisfies the Hurwitz condition since $\gamma \geq 0$ for $p_{mr} \leq 0$.

- For the band pass filter, the polynomial $L(s) = s^2 + 2(\alpha_n - p_{nr})s + p_{nr}^2 + p_{ni}^2 - 2\alpha_n p_{nr} - 2\beta_n p_{ni}$ satisfies the Hurwitz condition since the coefficients become all positive due to the passivity formulae.

- For the high pass filter, the polynomial $L(s) = (\psi_k + 1)s - p_{kr}$ satisfies the Hurwitz condition since $\psi_k \geq 0$ for $p_{kr} \leq 0$.

- For δ in the all pass filter, the polynomial $L(s) = \delta$ satisfies the Hurwitz condition since $\delta \geq 0$.

Hence, the filters in Equation (3.3) except η, which does not have any pole, have already satisfied the stability and passivity conditions based on the passivity formulae, which satisfy the Hurwitz's test as well as the maximum modulus theorem. The stability of η can be enforced using the Hurwitz's test, which results in $\eta \geq 0$. For a mulitport network, the enforcement can be extended to positive semi-definiteness for $[\eta]$. If the matrix $[\eta]$ is positive semi-definite, the circuit elements become all positive during the synthesis of the macromodel, as discussed in Section 3.6. Enforcing the positive semi-definiteness on all filters makes the circuit elements to be physically realizable passive devices during the synthesis of the macromodel.

In addition, the basic concept that the summation of passive sub-networks is passive is preserved. Therefore, the passivity formulae for a multiport network can be modified as:

$$\begin{aligned} eigenvalues\ of\ \ [\gamma_m] &\geq 0 \\ eigenvalues\ of\ \ [-\alpha_n p_{nr} \pm \beta_n p_{ni}] &\geq 0 \\ eigenvalues\ of\ \ [\psi_k] &\geq 0 \\ eigenvalues\ of\ \ [\delta] &\geq 0 \\ eigenvalues\ of\ \ [\eta] &\geq 0 \end{aligned} \tag{3.16}$$

3.5.2 Overlapping Real Poles

Consider a low pass filter with double real poles written in the form:

$$H(s) = \frac{as + b}{(s - p_r)^2} \tag{3.17}$$

Substituting $s = j\omega$ into Eq. (3.17), the real part $H_R(s)$ of the rational function can be written as:

$$H_R(s) = \frac{bp_r^2 - (b + 2ap_r)\omega^2}{(p_r^2 - \omega^2)^2 + (2\omega p_r)^2} \tag{3.18}$$

which results in another passivity formula for double real poles, namely:

$$\begin{aligned} b &\geq 0 \\ -b - 2ap_r &\geq 0 \end{aligned} \tag{3.19}$$

Equation (3.4) can therefore be extended as:

$$\begin{aligned} [H(s)] = &\sum_{m=1}^{LPN} \frac{[\gamma_m]}{s - p_{mr}} \\ &+ \sum_{d=1}^{DPN} \frac{[\epsilon_d]s + [\theta_d]}{(s - p_{dr})^2} \\ &+ \sum_{n=1}^{BPN} \frac{2[\alpha_n](s - p_{nr}) - 2[\beta_n]p_{ni}}{(s - p_{nr})^2 + p_{ni}^2} \\ &+ \sum_{k=1}^{HPN} \frac{[\psi_k]s}{s - p_{kr}} \\ &+ [\delta] + [\eta]s \end{aligned} \tag{3.20}$$

where the coefficient p_{dr} is real, the superscript DPN is the number of double real poles and the matrices $[\epsilon_d]$ and $[\theta_d]$ are PxP residue matrices for a P-port Network.

Therefore, the passivity formulae for a multiport network in Equation (3.20) can be modified as:

$$\begin{aligned} eigenvalues\ of\ \ [\gamma_m] &\geq 0 \\ eigenvalues\ of\ \ [\theta_d] &\geq 0 \\ eigenvalues\ of\ \ [-\theta_d - 2\epsilon_d p_{dr}] &\geq 0 \\ eigenvalues\ of\ \ [-\alpha_n p_{nr} \pm \beta_n p_{ni}] &\geq 0 \\ eigenvalues\ of\ \ [\psi_k] &\geq 0 \\ eigenvalues\ of\ \ [\delta] &\geq 0 \\ eigenvalues\ of\ \ [\eta] &\geq 0 \end{aligned} \tag{3.21}$$

3.5.3 Limitations of Multiport Passivity Formulae

Though the summation of passive sub-networks results in a passive network, the enforcement of passivity on sub-networks represents a sufficient but not necessary condition. Since the summation of non-passive sub-networks may result in a passive network, a concern is that the passivity constraints discussed in this dissertation may not apply for all frequency data. For a network containing only complex conjugate poles, the passivity constraints enforced on sub-networks can be satisfied due to the form of Equations (3.10) and (3.21). The problem arises when the network contains real poles. As an example, consider the transfer function,

$$H(s) = 10 - \frac{3}{s+2} \tag{3.22}$$

which is stable and passive but contains a non-passive sub-network. Using Equation (3.3), the above transfer function can be re-written in the form:

$$H(s) = 8 + \frac{1}{s+2} + \frac{2s}{s+2} \tag{3.23}$$

where the sub-networks are passive and the resulting transfer function is the same as Equation (3.22). The passivity constraints can now be enforced on each sub-network. In certain rare cases, when the frequency response cannot be represented as a summation of passive sub-networks as in Equation (3.3), enforcement of multiport passivity formulae may lead to some loss of accuracy.

3.6 Network Synthesis

Using the pole-residue representation of the rational function matrix $[H(s)]$ representing the admittance parameters, electrical networks consisting of resistors, inductors, capacitors, and controlled sources can be constructed [51]. For a one-port network in Equation (3.3), RL networks can be used to represent a real pole and residue of the low pass filter, RLC networks can be used to represent a complex conjugate pole

Low pass filter	Band pass filter	High pass filter	All pass filter
$Y_m(s) = \dfrac{\gamma_m}{s - p_{mr}}$	$Y_n(s) = \dfrac{2\alpha_n(s - p_{nr}) - 2\beta_n p_{ni}}{(s - p_{nr})^2 + p_{ni}^2}$	$Y_k(s) = \dfrac{s\psi_k}{s - p_{kr}}$	$Y(s) = \delta$ $\quad Y(s) = \eta\, s$
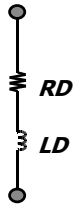 $RD_m = \dfrac{-p_{mr}}{\gamma_m}$ $LD_m = \dfrac{1}{\omega_o \gamma_m}$	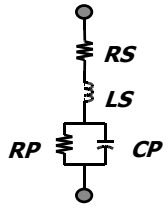 $RS = \dfrac{-\alpha_n p_{nr} + \beta_n p_{ni}}{2\alpha_n^2}$ $LS = \dfrac{1}{2\omega_o \alpha_n}$ $RP = \dfrac{p_{ni}^2(\alpha_n^2 + \beta_n^2)}{2\alpha_n^2(-\alpha_n p_{nr} - \beta_n p_{ni})}$ $CP = \dfrac{2\alpha_n^3}{\omega_o p_{ni}^2(\alpha_n^2 + \beta_n^2)}$	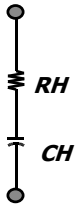 $RH = \dfrac{1}{\psi_k}$ $CH = -\dfrac{\psi_k}{p_{kr}\omega_o}$	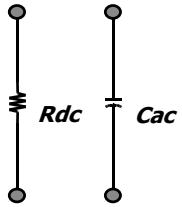 $Rdc = \dfrac{1}{\delta}$ $\quad Cac = \dfrac{\eta}{\omega_o}$

Figure 37: Values of the electrical elements

and residue pair of the band pass filter, and RC networks can be used to represent a real pole and residues of the high pass filter. A resistor and a capacitor can be used to represent the all pass filter. The values of the electrical components, which use frequency scaling, are shown in Figure 37. The frequency scaling will be discussed in Chapter 4. It is important to note that the sign of all elements becomes positive if multiport passivity formulae are satisfied.

For a multiport network in Equation (3.4), the configurations of electrical networks, which consist of a dummy voltage source, a current controlled voltage source, and a current controlled current source, are shown in Figure 38. The local ground for SPICE sub-circuits has been used in the circuit implementation. The self-admittance and trans-admittance networks are shown in Figure 39. It is important to note that the circuit elements in the trans-admittance network are also all positive. Hence, multiport passivity formulae enable the circuit elements to be all positive by using controlled sources.

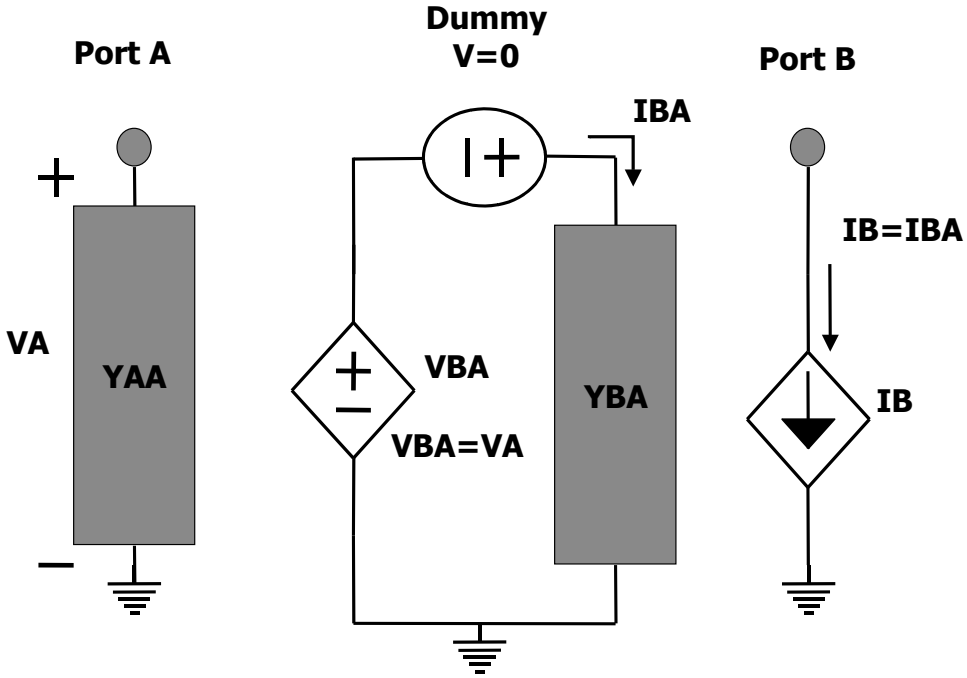

Figure 38: Electrical network configurations for the macromodel using admittance parameters

3.7 Summary

Using filter theory, any transfer function can be represented as a summation of low pass, band pass, high pass, and all pass filters. Using this property, the relationship between the frequency response and the coefficients of filters has been derived. This results in the conclusion that the magnitude, shape of the resonant peaks and the passivity of the macromodel depend on both poles and residues.

Using the pole-residue form of the rational function, multiport passivity formulae were successfully derived for checking and enforcing passivity of the macromodel. If the macromodel violated the multiport passivity formulae, negative eigenvalues in the residue matrix were set equal to zero or changed to a small positive value to ensure that the macromodel does not violate the passivity condition and then the residue matrix was reconstructed.

For ensuring stability and passivity for the all pass filter, positive semi-definiteness was enforced on the residue matrix $[\eta]$, which does not have explicit poles. This was

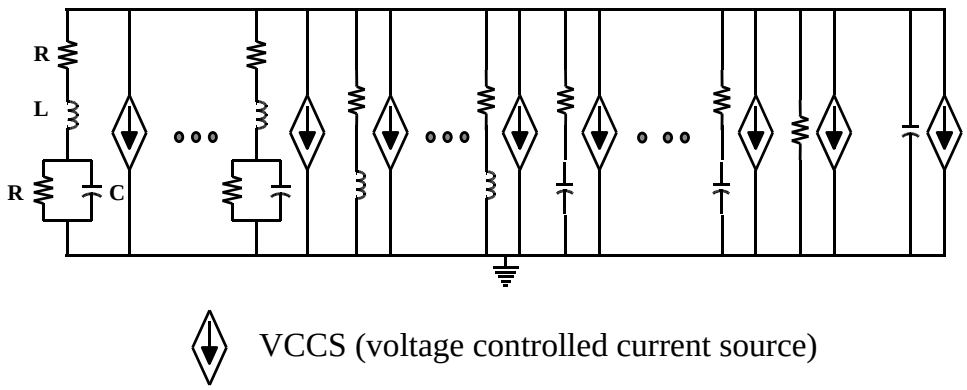

(a)

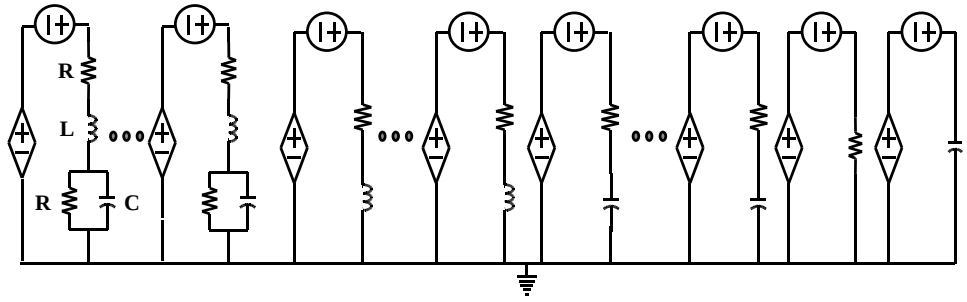

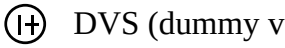

(b)

Figure 39: (a) Self-admittance YAA and (b) trans-admittance YBA realizations

based on the Hurwitz test. In addition, a low pass filter containing double real poles was included in the construction of the passive macromodel. It is important to note that the passivity formulae described in this chapter are sufficient but not necessary conditions. This may lead to some loss of accuracy in certain rare cases.

A method was developed for the synthesis of the macromodel into equivalent circuit elements. Based on the passivity formulae developed, the synthesis always results in positive circuit elements.

CHAPTER IV

BROADBAND MACROMODELS

For interconnect networks supporting fast transient waveforms, the macromodel needs to capture the frequency response of distributed networks accurately. In the past, numerical methods such as Pade approximation [23]-[28], least squares approximation [33]-[41], and vector fitting [42]-[47] have been used. However, since these methods use a single matrix for the construction of the macromodel, they do not capture a large number of resonant peaks due to the behavior of the ill-conditioned matrix. Hence, this chapter addresses the ill-conditioned matrix problem arising during the construction of broadband macromodels. In this chapter, several methods based on band division, selector, subband reordering, subband dilation, and pole replacement are presented.

For the automated construction of broadband macromodels, methods that determine the subbands automatically using the magnitude of the frequency response are presented. During the construction of multiport broadband macromodels, a method that reduces the size of the matrix for computing the common poles of the rational function matrix is discussed after discussing the property of common pole systems. For reducing the order of broadband macromodels, a method for eliminating filters that have minimal effect on the frequency response is presented.

4.1 Ill-conditioned Matrix Problem

The ill-conditioned matrix problem is apparent in Equation (1.1) where the power series expansion can have a large dynamic range. For instance, if the frequency response ranging from DC to 2.0 GHz needs to be approximated using the orders

$NS = 22$ and $DS = 22$, the dynamic range of elements in the matrix A in Equation (1.6) is from 1 to $(2\pi \times 2.0 \times 10^9)^{22}$, which causes the matrix to become ill-conditioned.

The ill-conditioned matrix problem can be improved by scaling the frequency using a constant factor ω_o. Using frequency scaling, Equation (1.5) can be rewritten in the form:

$$\sum_{ns=0}^{NS} a_{ns} \left(\frac{s}{\omega_o}\right)^{ns} - H(s) \sum_{ds=0}^{DS} b_{ds} \left(\frac{s}{\omega_o}\right)^{ds} = 0 \tag{4.1}$$

However, it has been shown that the scaling factor ω_o in Equation (4.1) does not result in significant improvement in the approximation beyond 20-30 poles [38], [39]. Hence, the author in [38] has used the Chebyshev polynomial expansion to approximate the frequency response using the orthogonal property of Chebyshev polynomials. However, it is important to note that the power series expansion with frequency scaling is comparable to the Chebyshev polynomial expansion for low order systems [39]. This property has been illustrated in Section 2.1 during the comparison between power series and orthogonal polynomials. In addition, a major problem with the Chebyshev polynomial expansion is that it needs to be finally converted into the pole-residue representation for implementation in SPICE. It is to be noted that since the size of the matrix has not changed, the ill-conditioned matrix problem still exists when the frequency response having a large number of poles needs to be approximated.

4.2 Limitations of Least Squares Approximation

In the following test cases, the performance of least squares approximation (LSA) is discussed by sweeping the order $NS = DS - 1$ from 1 to 40 in Equation (4.1). The frequency scaling factor used is $2\pi \times 1.0 \times 10^9$. In this section, only the stability condition is enforced on the rational function.

Table 4: Poles and residues of a known transfer function - Low order system

Filter	Original Poles [MHz]	Original Residues [MHz]
Low Pass (LP=1)	-0.2	0.001
Band Pass (BP=2)	$-4 \pm 162j$ $-5 \pm 437j$	$0.22 \pm 0.0015j$ 0.04

4.2.1 Low Order System

A known transfer function with poles and residues shown in Table 4 was used to generate the frequency response from 1.0 Hz to 1.0 GHz with 500 equally spaced frequency samples. Using the frequency response, the transfer function was constructed by sweeping the order $NS = DS - 1$ from 1 to 40 to check the performance of the LSA discussed earlier.

The frequency response of the system was successfully captured, as shown in Figure 40. As shown in Figure 41, the extracted number of low pass and band pass filters is $LP = 1$ and $BP = 4$, respectively. For further discussion, Figures 40 and 41 have been analyzed with details as follows:

- Figure 40(a) shows the root-mean-square (RMS) error between the actual response and the approximated response as the order NS is increased for the rational function. From the figure, the accuracy of the rational function is not improved as the order NS increases beyond $NS = 14$. In fact, the RMS error increases beyond $NS = 15$.

- Figure 40(b) shows the original frequency response (solid line) generated from the known transfer function, the frequency response (dotted line) generated from the rational function of order NS of 14, and the deviation (dashed line). For the order NS of 14, the rational function has successfully approximated the frequency response of the system.

- Figure 41(a) shows the distribution of the poles of the known transfer function

and the extracted rational function. From the figure, two spurious filters with complex conjugate poles located far away from the imaginary axis have been extracted. It is important to note that a pole pair at 2.07 GHz has been extracted, which is located outside the frequency band of 1.0 GHz. This issue will be discussed in a later section.

- Figure 41(b) shows the distribution of the residues of the known transfer function and the rational function approximated. From the figure, residues of the two spurious poles have negligible values compared to the other residues. As discussed in Chapter 3, this results in the small magnitudes of resonant peaks corresponding to the two spurious poles. In a later section, this property will be used for reducing the order of the macromodel.

4.2.2 High Order System

To see the performance of the LSA for a high order system having increased real and complex conjugate pair poles, a known transfer function with poles and residues shown in Table 5 was used to generate the frequency response from 1.0 Hz to 1.0 GHz with 500 equally spaced frequency samples.

As compared to the low order system, the frequency response has more resonant peaks within the frequency of interest. Similarly, the transfer function was constructed by sweeping the order $NS = DS - 1$ from 1 to 40 to check the performance of LSA. For order $NS = 14$ having the minimum error in Figure 42(a), the extracted number of low pass and band pass filters is $LP = 2$ and $BP = 6$, respectively. However, both the frequency response and transfer function of the system were inaccurately captured as shown in Figures 42 and 43. Figures 42 and 43 have been analyzed with details as follows:

- In Figure 42(a), the RMS error between the frequency response of the original

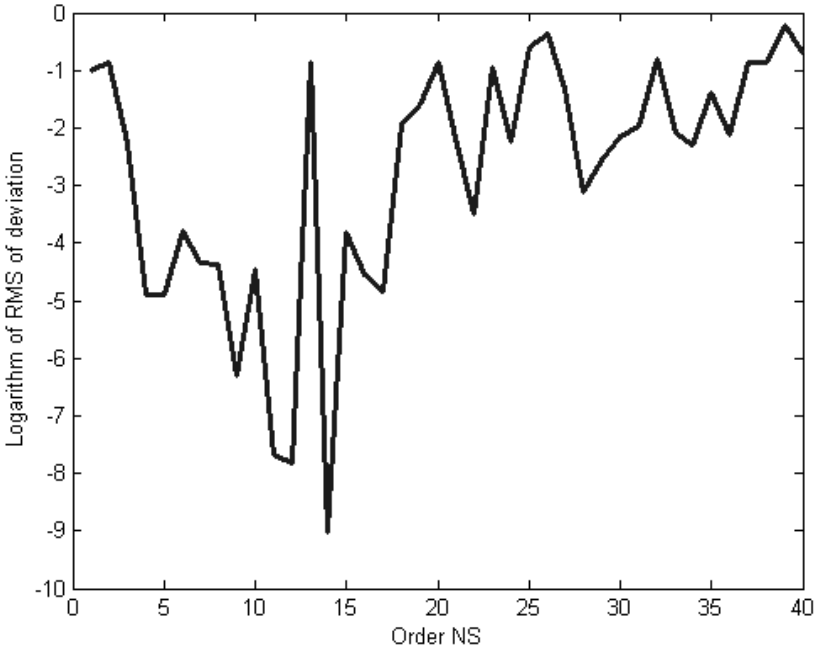

(a)

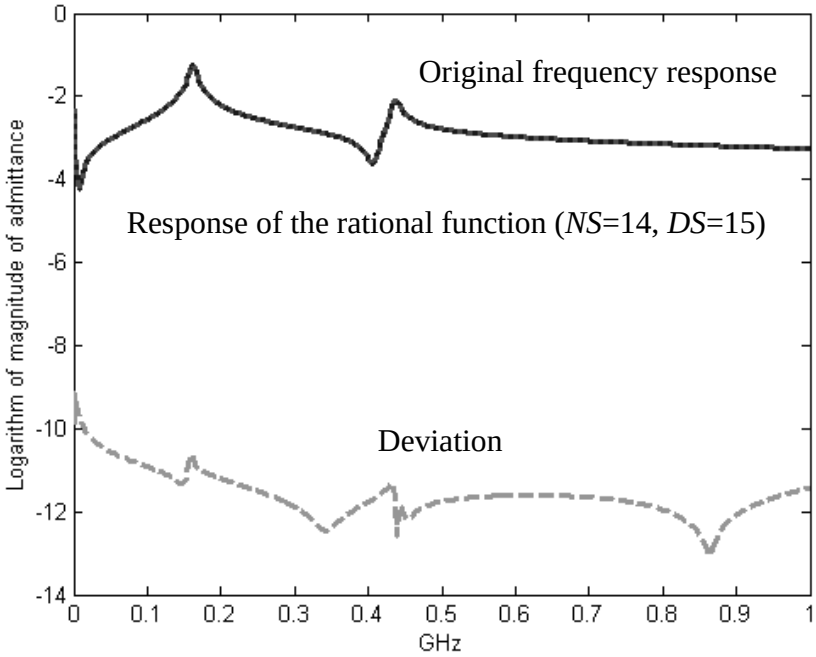

(b)

Figure 40: Performance of LSA for $LP = 1$ and $BP = 2$: (a) the RMS error of the deviation vs. the order NS and (b) the original frequency response (solid line) of the known transfer function, the frequency response (dotted line) of the rational function of order $NS = 4$ and $DS = 5$, and the deviation (dashed line)

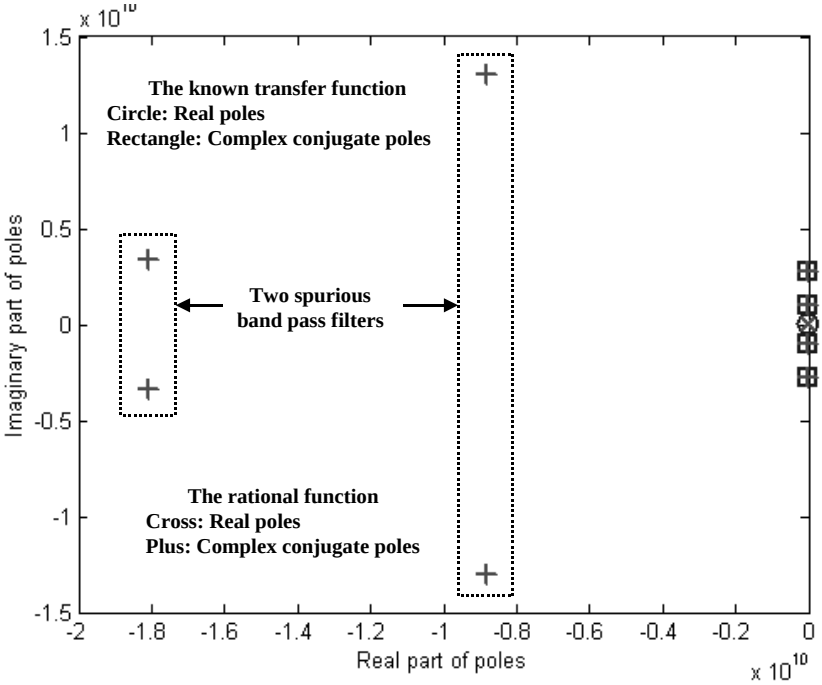

(a)

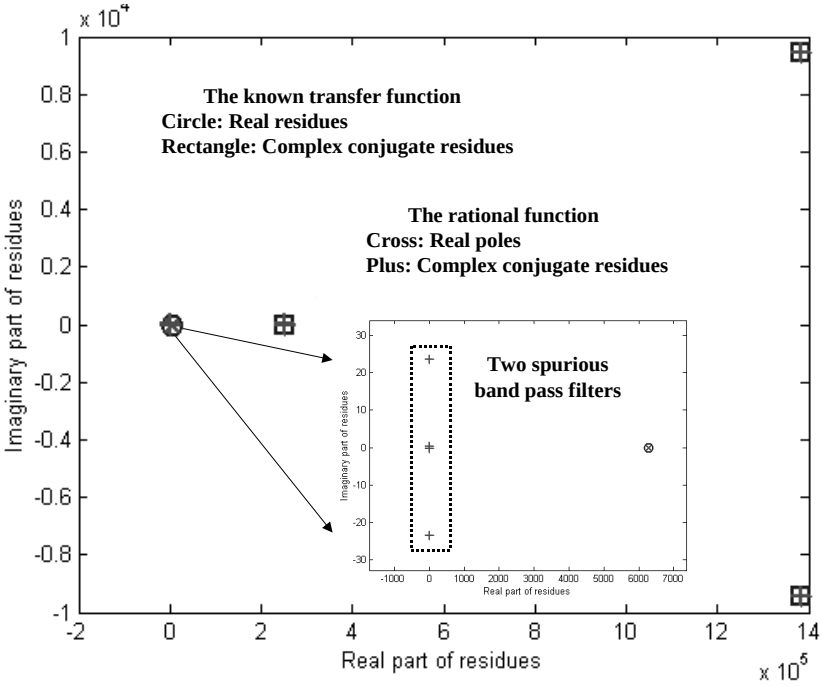

(b)

Figure 41: Performance of LSA for $LP = 1$ and $BP = 2$: (a) comparison of pole distributions and (b) comparison of residue distributions

Table 5: Poles and residues of a known transfer function - High order system

Filter	Original Poles [MHz]	Original Residues [MHz]
Low Pass (LP=3)	-0.2	0.001
	-2.3	0.076
	-4.5	0.841
Band Pass (BP=8)	$-4 \pm 52j$	0.1
	$-4 \pm 162j$	$0.22 \pm 0.0015j$
	$-5 \pm 291j$	0.5
	$-2 \pm 309j$	0.02
	$-4 \pm 325j$	$0.52 \pm 0.0011j$
	$-5 \pm 437j$	0.04
	$-5 \pm 488j$	0.12
	$-11 \pm 818j$	$1.19 \pm 0.0090j$

transfer function and the extracted transfer function is plotted as a function of the order NS. Beyond $NS = 15$, the error increases.

- In Figure 42(b), the frequency response is compared between the extracted rational function and known transfer function for order $NS = 14$. The error is also plotted as a deviation in Figure 42(b). Based on Figures 42(a) and (b), it is clear that the LSA is limited to low order systems, meaning that the minimum eigenvalue tracking method is also limited to only low order systems.

- Figure 43(a) shows the distribution of the poles of the known transfer function and the extracted rational function. From the figure, only a complex conjugate pole pair is accurately captured.

- Figure 43(b) shows the distribution of the residues of the known transfer function and the extracted rational function. From the figure, the residues of the low pass and band pass filters are inaccurately extracted and all the filters become spurious filters.

Figure 43 shows several real and complex conjugate poles and residues extracted for the rational function with order $NS = 14$. The extracted number of low

pass and band pass filters is $LP = 2$ and $BP = 6$, respectively. However, it should be noted that the minimum eigenvalue tracking method is valid for low order systems.

4.3 Band Division

As shown in Equation (3.4), the rational function matrix $[H(s)]$ has been represented in the pole-residue form as a summation of sub-networks. Both the stability and passivity conditions in each sub-network were satisfied using stability constraints and multiport passivity formulae described earlier. Since stability constraints and passivity formulae were only enforced on each sub-network, there is no relationship for the stability and passivity conditions between sub-networks except that they contribute to the overall response of the macromodel. This enables the entire frequency response to be divided into smaller frequency bands that alleviate the ill-conditioned problem discussed in the previous section.

The basic idea for the construction of the broadband macromodel is that if complex conjugate poles and real poles can be extracted from a localized region of the frequency response, then the original frequency response can be divided into smaller frequency bands (or subbands), as shown in Figure 44. In Figure 44, poles from the localized region within a subband can be extracted. The process of dividing the entire frequency band of interest into smaller subbands is called as band division in this dissertation. The subbands can be either of uniform or non-uniform width and contain a set of sampled frequency data, as shown in the figure. The criterion for choosing the width of each subband depends on the nature of the frequency response. It is desirable to divide the entire frequency band into subbands where resonant peaks exist. In areas where no resonant peaks exist, the subbands are overlapped to minimize the number of subbands required. The orders NS and DS for each subband can be estimated by using the minimum eigenvalue tracking method based on the least squares approximation or counting the number of resonant peaks in the

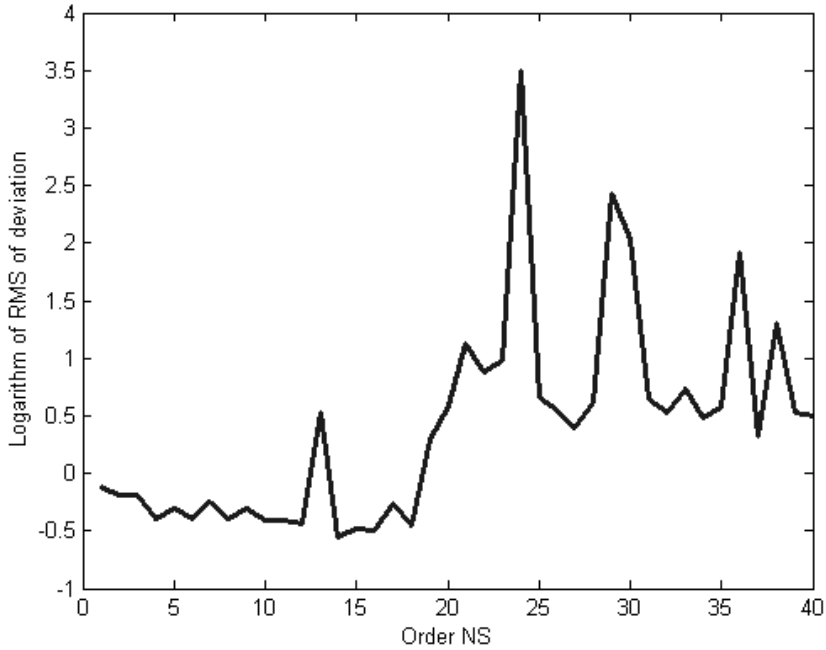

(a)

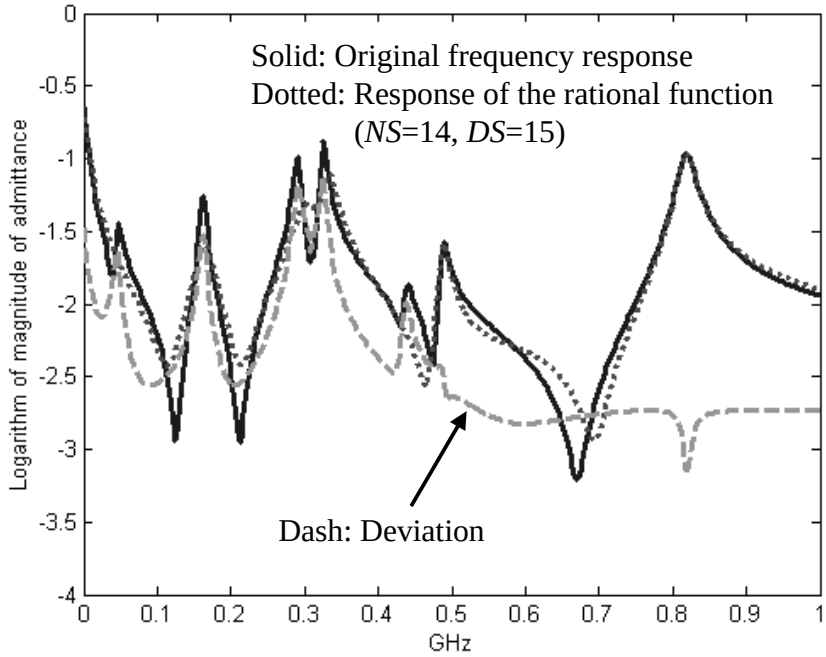

(b)

Figure 42: Performance of LSA for $LP = 3$ and $BP = 8$: (a) the root-mean-square error of the deviation vs. the order NS and (b) the original frequency response (solid line) of the known transfer function, the frequency response (dotted line) of the rational function of the order NS of 14, and the deviation (dashed line)

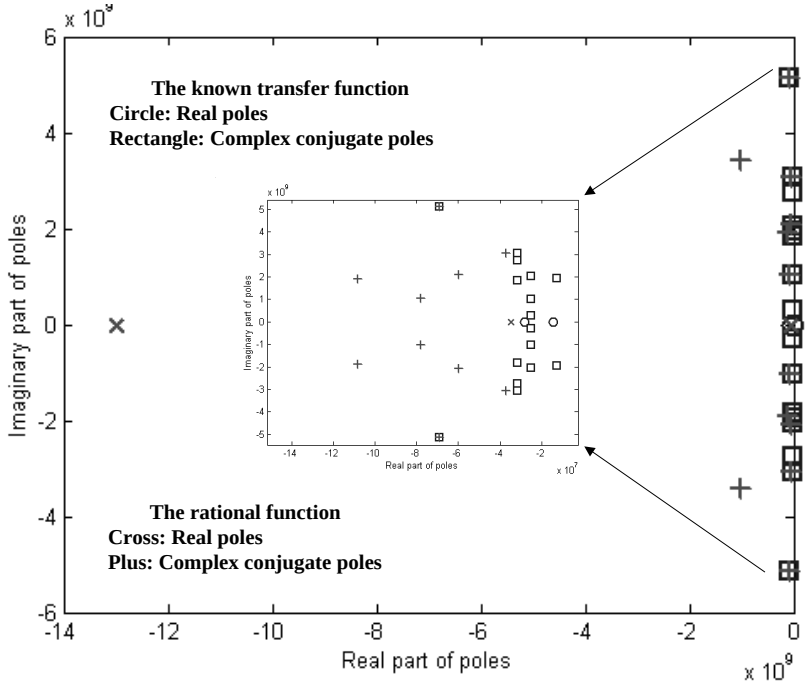

(a)

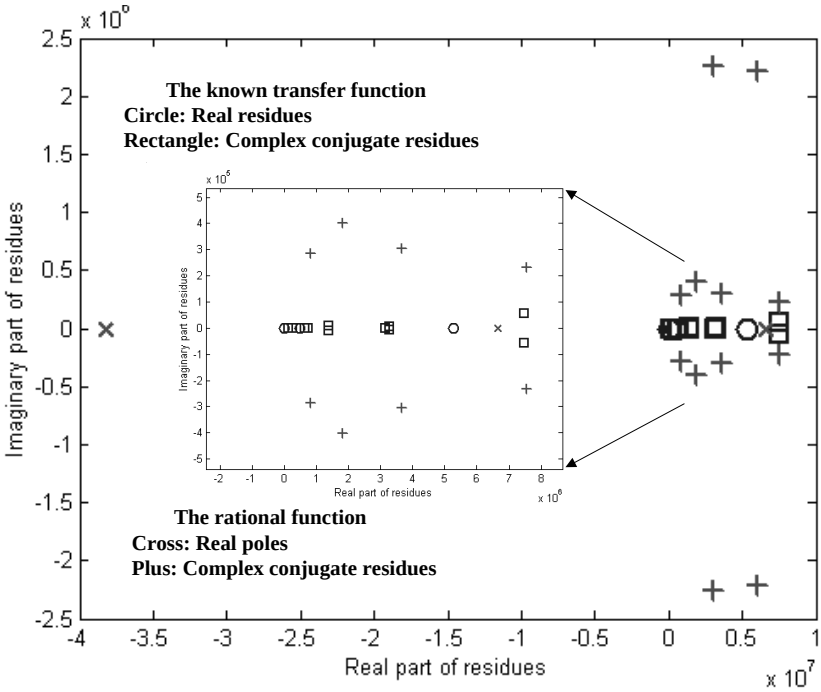

(b)

Figure 43: Performance of LSA for $LP = 3$ and $BP = 8$: (a) comparison of pole distributions and (b) comparison of residue distributions

frequency response.

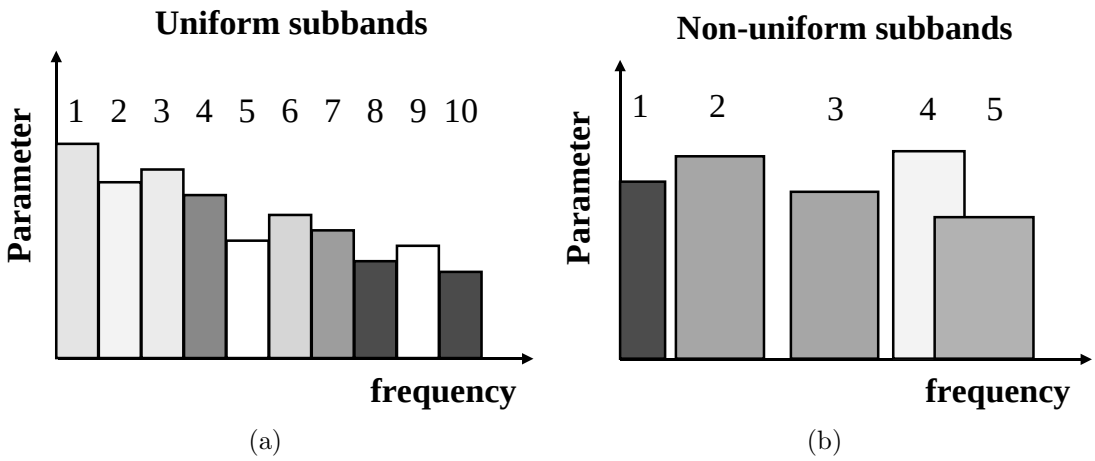

Figure 44: Band division: (a) 10 uniform subbands and (b) 5 non-uniform subbands (subbands 1, 2, 3: non-overlapping, subbands 4, 5: overlapping)

4.4 Band Interactions

During the least squares approximation process discussed in Chapter 1, the residues have been computed after computing the stable poles. In the algorithm, the stable poles are retained after removing the unstable poles, which are often present. However, it is important to note that the stable poles are affected by the unstable poles during least squares approximation. Hence, inaccurate residues can be extracted due to the inaccurate stable poles, which results in the violation of the passivity condition. Therefore, it is critical to extract the accurate poles from the frequency band of interest. This is caused by the interaction between poles and residues, which affects the accuracy of the macromodel.

Using band division, the macromodel for each subband can be extracted in parallel. However, the macromodel from each subband can interact with each other since the extrapolation of each macromodel outside the subband of interest can produce a non-zero frequency response in adjacent subbands. This interaction, called a band interaction in this dissertation, can result in an erroneous frequency response when sub-macromodels are combined, as shown in Chapter 5. Hence, four methods,

namely, selector, subband reordering, subband dilation and pole replacement methods have been developed for compensating the interaction between subbands.

4.4.1 Selector

In Chapter 3, the multiport passivity formulae were derived from the pole-residue form of the rational function using filter theory. This led to the representation of the frequency response of any linear time-invariant passive network as a summation of low pass, band pass, high pass and all pass filters. Therefore, the interaction between subbands can be regarded as the interaction between filters. For alleviating the interaction between subbands, a method of handling the filter interaction is required, which is called as the selector method in this dissertation. The terminology 'selector', which selects the filters, is used to differentiate it from the terminology 'filter', which generates the frequency response. Since there are four types of filters, namely, low pass, band pass, high pass and all pass filters, the selector method requires handling of all the filters.

For applying the selectors on filters, it is important to determine the filters within and outside the subband of interest. This is because undesirable filters can be found during the construction of the macromodel from each subband since there are no constraints that limit the type and position of the filters. This was demonstrated during the discussion on the limitations of least squares approximation in Section 4.2.

As shown in Figure 33, the low pass filter can be located in the first subband since the peak (magnitude) of the low pass filter is located at DC. Similarly, the high pass filter can be located in the last subband since the peak of the high pass filter is located at infinite frequency. Hence, the low pass and high pass filters can be selected by passing and removing the filters, depending on the subband of interest. However, the band pass filter can be located in any subband, depending on the imaginary value of the poles of the filter. The band pass filter has several types of selectors.

For discussion, consider a subband shown in Figure 45(a). In the figure, region BB between frequency points α and β is the frequency response to be interpolated. The remaining regions, namely, LB and HB are outside the frequency region BB. Hence, several scenarios aries during the approximation of the frequency response of the region BB. These are:

1. **Region BB is dominated by the band pass filters in the regions LB and BB:** For accurate approximation of the region BB, it is necessary to extract the band pass filters that approximate the regions LB (extrapolation) and BB (interpolation). This can be achieved using the L-type selector shown in Figure 45(b). The L-type selector ensures smooth extrapolation when the band-limited frequency response is approximated.

2. **Region BB is dominated by the band pass filters in the region HB:** For accurate approximation of the region BB, it is necessary to extract the band pass filters that approximate the region HB (extrapolation). This can be achieved using the H-type selector.

3. **Region BB is dominated by the band pass filters in the region BB:** For accurate approximation of the region BB, it is necessary to extract the band pass filters in the region BB (interpolation). This can be achieved using the B-type selector.

4. **Region BB is dominated by the band pass filters in the regions LB and HB:** For accurate approximation of the region BB, it is necessary to extract the band pass filters approximating the regions LB and HB (extrapolation). This can be achieved using the R-type selector.

5. **Region BB is dominated by the band pass filters in the region LB:** For accurate approximation of the region BB, it is necessary to extract the band

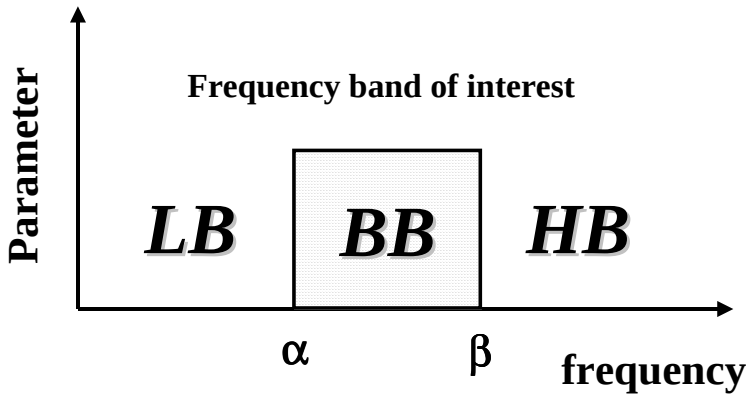

(a)

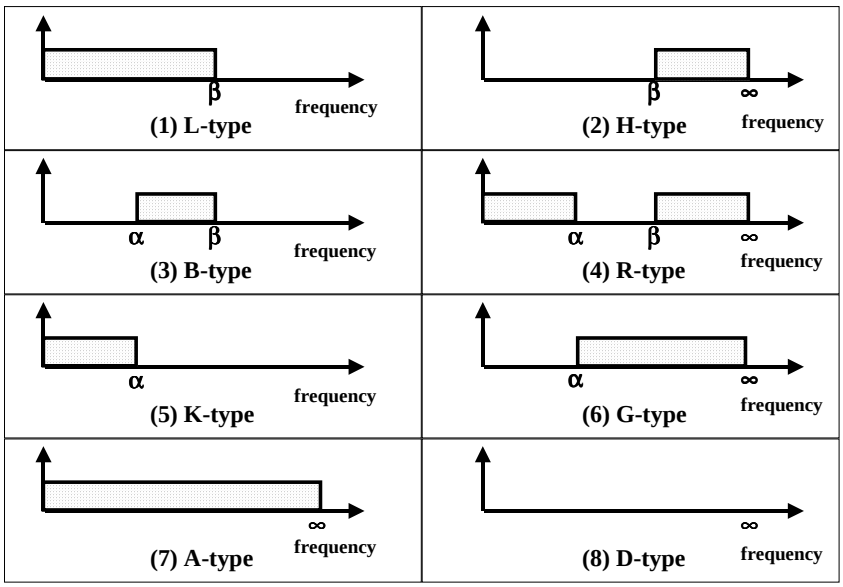

(b)

Figure 45: (a) Frequency subband and (b) selectors

pass filters approximating the region LB (extrapolation). This can be achieved using the K-type selector.

6. **Region BB is dominated by the band pass filters in the regions BB and HB:** For accurate approximation of the region BB, it is necessary to extract the band pass filters approximating the regions BB (interpolation) and HB (extrapolation). This can be achieved using the G-type selector.

Hence, the L-type, H-type, B-type, R-type, K-type and G-type selectors can be used for selecting and retaining the band pass filters appropriately. As shown in Figure 45(b), the A-type and D-type selectors can be used for passing and removing all the band pass filters, respectively.

4.4.2 Subband Reordering

Often times, realistic distributed networks having a large amplitude variation need to be approximated. In this case, for minimizing the interaction between subbands, the construction sequence is reordered based on the magnitude of the frequency response at every stage. This is called as subband reordering in this dissertation. The sub-macromodel of the subband with the largest magnitude is constructed first, prior to the other subbands. This is shown in Figure 46, where subbands 2 and 3 in Figure 44(a) are interchanged during the macromodel construction process. Subband reordering reduces numerical errors caused by dominant poles in an adjacent subband. For the construction of the sub-macromodel from the subband of interest, three steps are used. First, the frequency response of the subband of interest is prepared by subtracting the frequency response of the broadband macromodel from the original frequency response. Second, the sub-macromodel from the subband of interest is constructed using least squares approximation. Third, the selectors are applied to select the filters in the sub-macromodel.

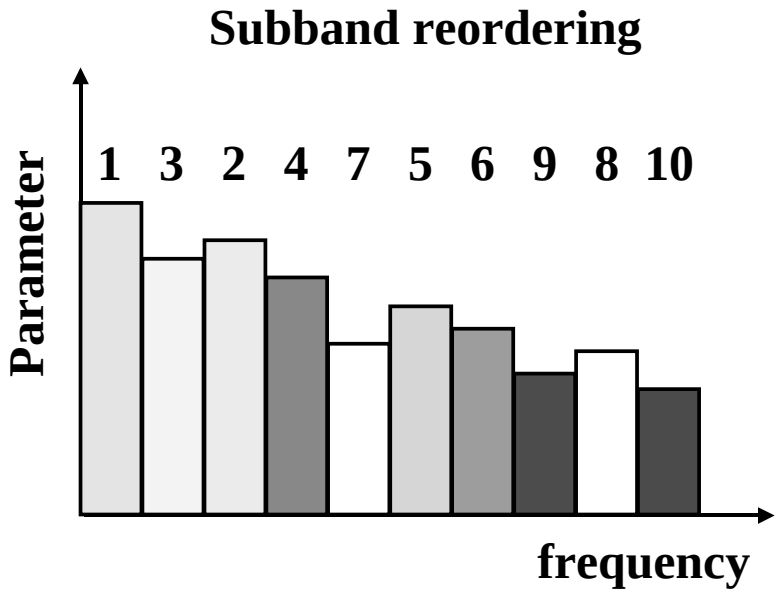

Figure 46: Subband reordering

4.4.3 Subband Dilation

In subband dilation, the subbands are dilated to provide local correction in the region between adjacent subbands. This method results in an overlap between subbands, as shown in Figure 47. In the figure, subband 'n' is dilated to overlap subbands 'n-1' and 'n+1'. The amount of overlap is determined by the position of poles in each subband. If the poles are located at the boundary between bands, then these poles have the maximum effect on both frequency bands. As the poles are located farther away from the boundary, the effect of these poles on adjacent bands is minimized. Using this criterion, the subbands are suitably dilated such that the poles at the boundary lie in the overlapped region. The macromodels of the three subbands are then iteratively corrected by monitoring the error in the three subbands using the pole replacement method discussed in the next section.

4.4.4 Pole Replacement

Though subband reordering and subband dilation methods minimize the interaction between subbands, correction may once again be necessary since these methods may

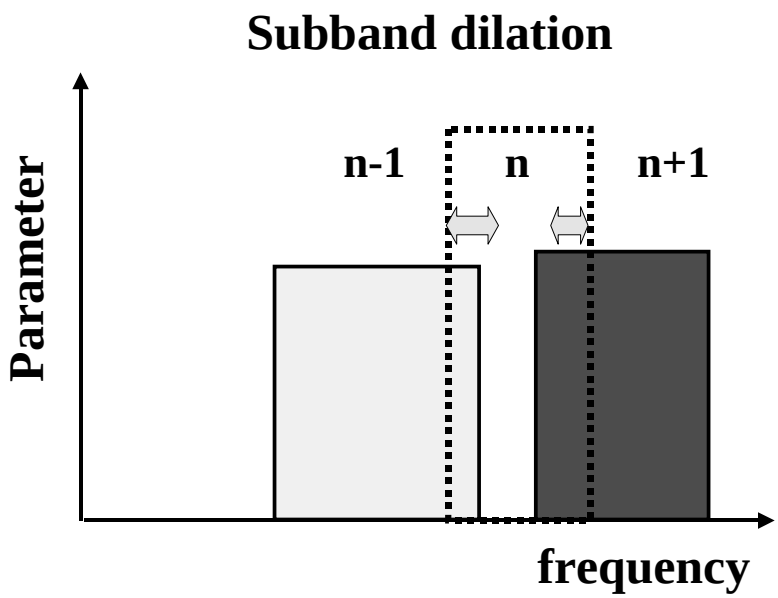

Figure 47: Subband dilation

sometimes miss the poles at the boundary between subbands or generate spurious poles within the subband. This dissertation uses a pole replacement method to improve the accuracy of the constructed macromodel by discarding spurious poles and extracting accurate poles, as shown in Figure 48. The pole replacement method is applied after the macromodel for each subband is constructed. The details of the pole replacement method are described below.

1. The process begins with the comparison between the original frequency response $[Ho(s)]$ and the frequency response $[Hm(s)]$ from the macromodel.

2. Based on the error criterion, the maximum difference value Emo and location Lmo between $[Ho(s)]$ and $[Hm(s)]$ are calculated and stored.

3. The algorithm searches for a set of poles around the location Lmo and determines the width of the subband to be recalculated.

4. The root-mean-square error $RMSe$ between $[Ho(s)]$ and $[Hm(s)]$ in the subband is calculated and stored. The frequency response associated with the poles in the subband is then subtracted from $[Hm(s)]$ in order to recalculate

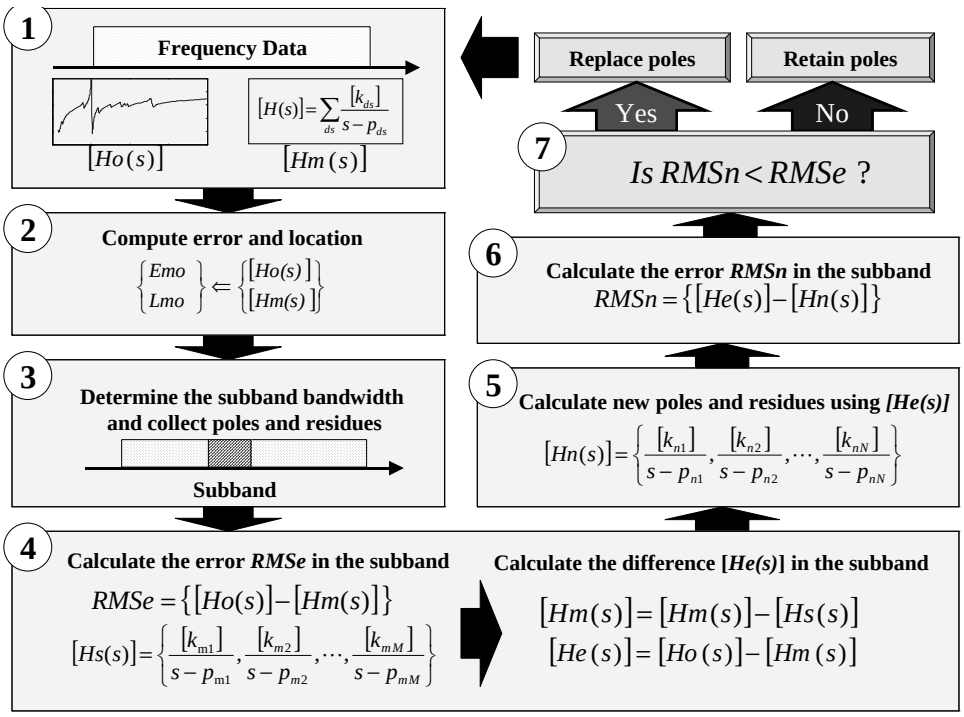

Figure 48: Pole replacement

the frequency response of the subband. Then, the difference between $[Ho(s)]$ and $[Hm(s)]$ is calculated and stored in $[He(s)]$.

5. Using $[He(s)]$, new poles and residues are recalculated in the subband.

6. The frequency response using new poles and residues $[Hn(s)]$ is computed and the root-mean-square error $RMSn$ between $[He(s)]$ and $[Hn(s)]$ in the subband is again calculated and stored.

7. If $RMSn < RMSe$, then old poles and residues are replaced with new poles and residues. If $RMSn > RMSe$, then old poles and residues are retained.

8. Steps 1 to 7 are repeated until the error is minimized.

The location and size of each subband is recalculated iteratively in the pole replacement method. The error criterion determines the maximum error value Emo, the location Lmo, and the width of the subband being recalculated. In this research,

the root-mean-square error has been used as the error criterion and the subband width around the location Lmo is determined based on the position of poles being replaced. Assuming the number of poles being replaced is k, the algorithm searches for $k+2$ poles around the location Lmo. The $k+2$ poles are then reordered in increasing frequency such that pole $p(1)$ corresponds to the lowest frequency and pole $p(n)$ corresponds to the highest frequency. The left and right boundaries of the subband are then determined as the mid-frequency points between poles $p(1)$, $p(2)$ and $p(n-1)$, $p(n)$, respectively. If the width and position of the subband remains the same as before, then the subband is suitably dilated to minimize error. If the location Lmo is not changed after dilating the subband, then the location Lmo is stored and ignored in subsequent iterations.

With the use of band division, subband reordering and subband dilation methods, the number of iterations required for the pole replacement method to converge is minimum. Even though the pole replacement method was originally intended for increasing the accuracy of poles and residues of the passive macromodel, it can be used to compensate for negative eigenvalues by inserting additional poles and residues, as discussed in Chapter 1. After the poles and residues in the entire frequency band or subbands are calculated, the residue matrices δ and η can be calculated. It is important to note that the broadband macromodel can be constructed using band division, subband reordering, subband dilation, and pole replacement methods along with frequency scaling, without having an ill-conditioned matrix problem. In addition, since the number of required poles is reduced and the orders NS and DS become small within a subband, the size of the matrix A in Equation (1.6) becomes small and the required computational memory and CPU time can be reduced. Therefore, the minimum eigenvalue tracking algorithm which was originally limited to a low-order system can be used for the construction of broadband macromodels containing hundreds of poles.

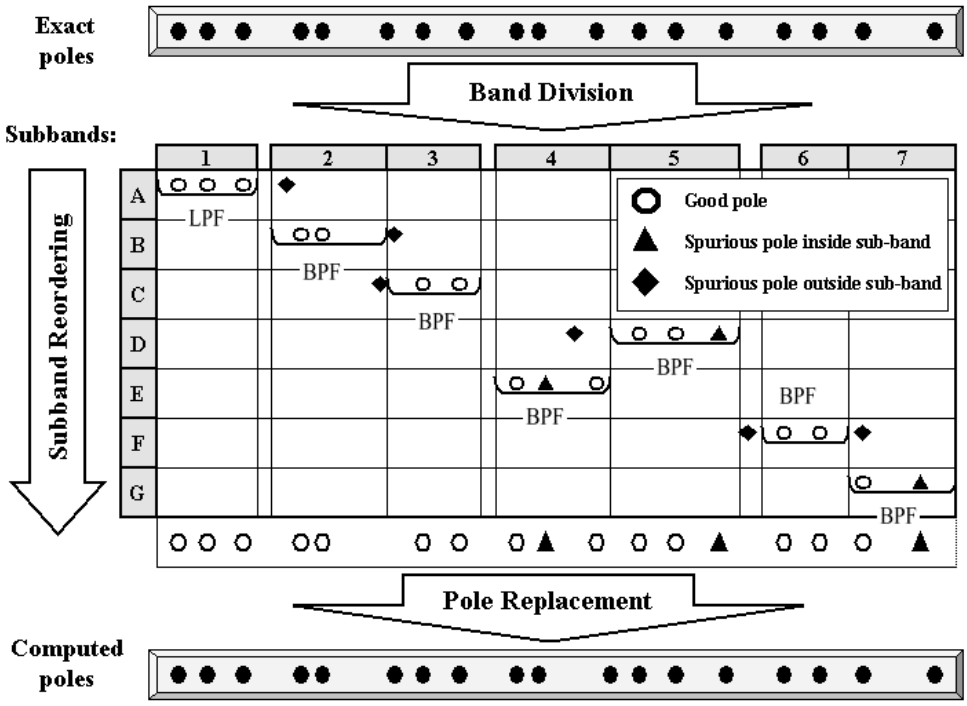

Figure 49: Illustration of the band division and subband reordering methods

4.5 Illustrative Example

The application of the methods discussed is illustrated in Figure 49. The exact poles of the network are shown at the top of the figure. It has been assumed that all the poles are complex conjugate poles. In Figure 49, the good poles are the exact poles of the network. All the other poles except for the good poles are regarded as spurious poles. Using the band division method, the entire frequency response has been divided into 7 non-uniform subbands such that each subband has between one to four resonant peaks. The bands are numbered from 1 - 7 horizontally and named A - G vertically. This has been done intentionally to differentiate band division from subband reordering. The steps illustrated below assume that after the extraction of the poles from each subband, the corresponding residues are extracted. The frequency response of the broadband macromodel is then subtracted from the overall response prior to the macromodel construction for the next subband. The various steps are described below:

1. During the construction of the sub-macromodel from subband A, three good poles and a spurious pole located outside subband A are extracted using the eigenvalue method discussed earlier. After applying the L-type selector with bandwidth equal to subband 1, three good poles are extracted.

2. After subtracting the frequency response of the above macromodel from the overall response, a spurious pole located outside subband B and two good poles are extracted from subband B. After applying the B-type selector on subband B, the spurious pole is removed and two good poles are retrieved. Note that there is an exact pole near the boundary between subbands B and C, which is not included.

3. During the calculation in subband C, a spurious pole located outside subband C and two good poles are extracted. After applying the B-type selector, two good poles are retained. Up to this point, seven good poles have been extracted and an exact pole near the boundary of subbands B and C has been missed.

4. The next computational domain moves to subband D corresponding to subband 5 instead of subband 4 (subband reordering). This is because the magnitude of the frequency response is larger in subband 5 than in subband 4. The sub-macromodel constructed from subband D results in two spurious poles and two good poles. After applying the B-type selector to remove poles located outside subband D, a spurious pole and two good poles are extracted.

5. From subband E corresponding to subband 4, a spurious pole and two good poles are extracted. After applying the B-type selector, a spurious pole and two good poles are retained.

6. From subband F corresponding to subband 6, two spurious poles located outside subband F and two good poles are extracted. After applying the B-type selector,

two good poles are retained.

7. From subband G, a spurious pole and a good pole are extracted after applying the G-type selector. After collecting sub-macromodels from each subband, 14 good poles and 3 spurious poles are found using the band division and subband reordering methods. The pole replacement method is now applied to correct the good poles and eliminate the spurious poles.

4.6 Test Cases

4.6.1 Test Case 1: Frequency response from a known transfer function (low-order system)

To demonstrate the application of the band division and subband reordering methods using selectors for handling the filters, the frequency response derived from a known transfer function of a low-order system has been used. The transfer function has a low pass filter having a pole -0.2 with its residue 2 and two band pass filters having two complex conjugate pole pairs at $-0.05 \pm j$, $-0.3 \pm j3.5$ with corresponding residues $2 \mp 0j$ and $10.0 \mp 0.03j$. The transfer function was used to extract the frequency response from 0.001 [radian/sec] to 10 [radian/sec] with 10,000 frequency samples. The frequency response was divided into 3 irregularly spaced subbands, $\omega = 0.001 - 0.2$ [radian/sec], $\omega = 0.9 - 1.1$ [radian/sec], and $\omega = 3.2 - 3.7$ [radian/sec]. The criterion for choosing the subbands was based on the given frequency data whereby at least one resonant peak existed in the subbands. The orders NS of 6 and DS of 7 were used for capturing the frequency response in the first and second subbands and the orders NS of 10 and DS of 11 were used for capturing the response of the third subband.

Initially, no selectors were used to remove spurious filters. The poles and residues of the constructed macromodel are shown in Table 6. The frequency response of the macromodel is shown in Figure 50. As is evident in Figure 50, the

Table 6: Without using selectors

	Poles	Residuse
Subband 1	-0.19999915	2.00017346
	$-0.02674632 \pm 1.16151630j$	$3.77686436 \mp 0.08154520j$
Subband 2	$-0.04999999 \pm 1.00000001j$	$1.99998865 \mp 0.00001349j$
	$-0.30795401 \pm 3.48647974j$	$9.93377716 \mp 0.00230286j$
Subband 3	$-0.31274900 \pm 3.48027639j$	$3.93938323 \pm 0.34367262j$

macromodels constructed from the three subbands result in an erroneous frequency response because of the interaction between subbands.

Next, selectors were applied to each subband. From the first subband, a real pole and two complex conjugate poles were extracted. Of these poles, only the real pole was located within subband 1. Using a L-type selector with bandwidth equal to subband 1, only one real pole was retained. The frequency response of the macromodel generated from subband 1 is shown in Figure 51(a). After subtracting this macromodel from the original frequency response, the poles were extracted from subband 2. Four complex conjugate poles were extracted. Two complex conjugate poles were located within subband 2. Using a B-type selector with bandwidth equal to subband 2, two complex conjugate poles were retained. The frequency response from the broadband macromodel generated from subbands 1 and 2 is shown in Figure 51(b). After subtracting the broadband macromodel from the original frequency response, two complex conjugate poles were extracted from subband 3. Using a B-type selector with bandwidth equal to subband 3, two complex conjugate poles were retained. The poles and residues before and after the construction of sub-macromodels are shown in Tables 7 and 8, respectively.

In Table 7, the poles (second complex conjugate pole pair) extracted from subband 1 inaccurately captured the poles of subband 2 and the poles extracted from subband 2 accurately captured the poles of subband 3, resulting in an erroneous frequency response without the use of selectors. The comparison between the original

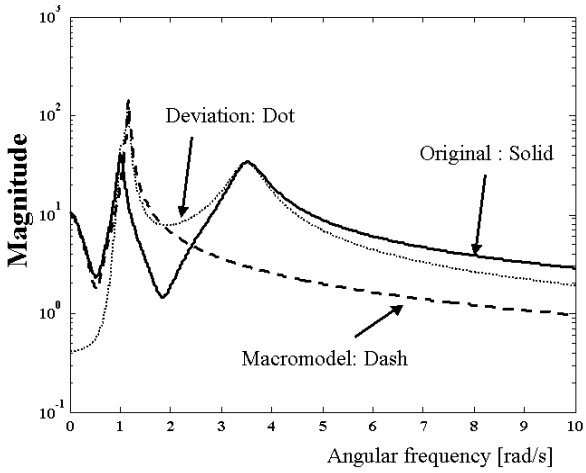

(a)

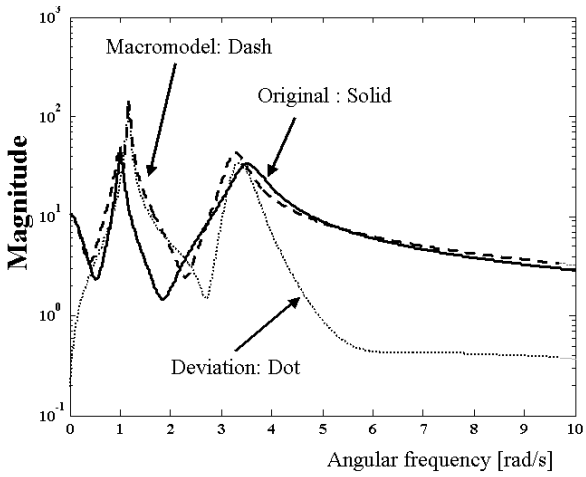

(b)

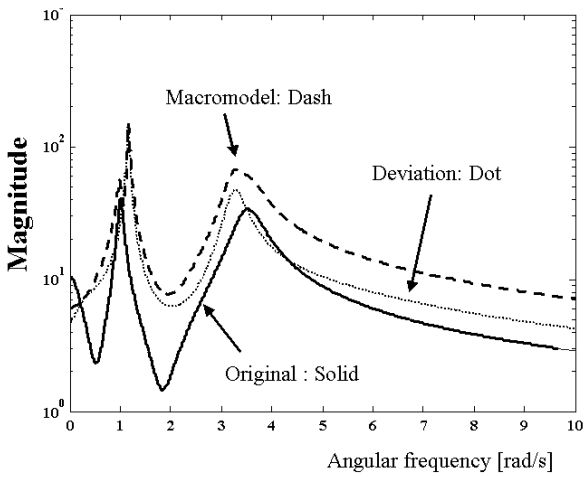

(c)

Figure 50: The magnitude comparison between the original data and the response of macromodels without using selectors (Solid line: Original, Dashed line: Macromodels, Dotted line: Deviation): (a) the first subband, (b) the first and second subbands and (c) the entire frequency band

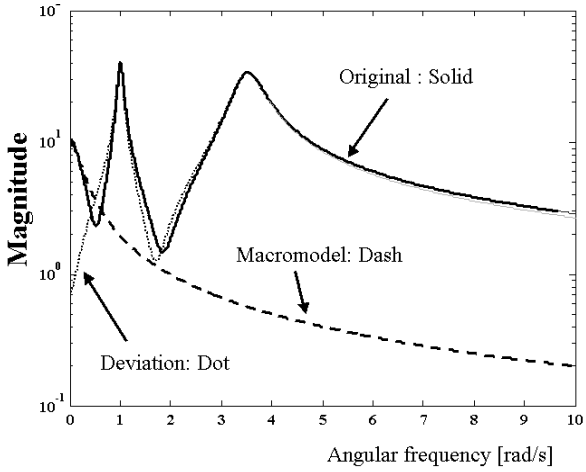

(a)

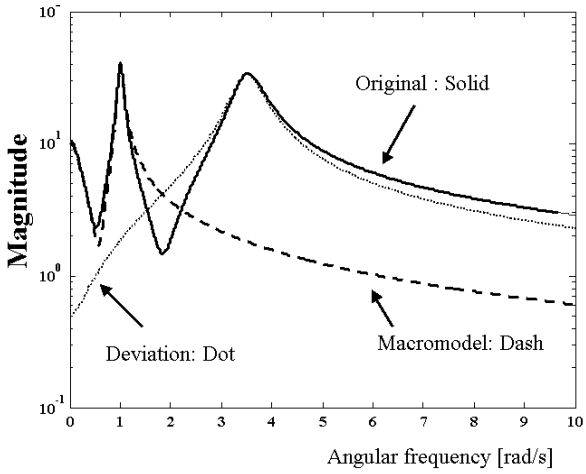

(b)

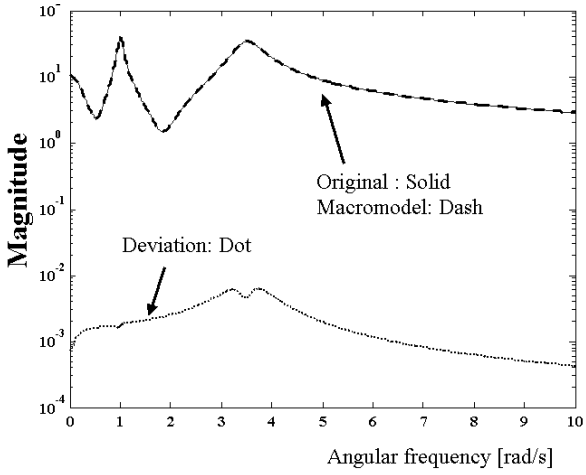

(c)

Figure 51: The magnitude comparison between the original data and the response of macromodels with filters (solid: original, dash: macromodel, dot: deviation): (a) the first subband, (b) the first and second subbands and (c) the entire frequency band

Table 7: Using selectors (before)

	Poles	Residues
Subband 1	-0.19999915	2.00017346
	$-0.02674632 \pm 1.16151630j$	$3.77686436 \mp 0.08154520j$
Subband 2	$-0.04999999 \pm 0.99999999j$	$2.00000111 \pm 0.00000335j$
	$-0.30861992 \pm 3.50878764j$	$10.00240491 \mp 0.04257531j$
Subband 3	$-0.30003413 \pm 3.50022682j$	$10.00240491 \mp 0.04257531j$

Table 8: Using selectors (after)

	Poles	Residuse
Subband 1	-0.19999915	2.00017346
Subband 2	$-0.04999999 \pm 0.99999999j$	$2.00000111 \pm 0.00000335j$
Subband 3	$-0.30003413 \pm 3.50022682j$	$10.00240491 \mp 0.04257531j$

frequency data and the response of the broadband macromodel constructed from subbands 1, 2, and 3 using selectors is shown in Figure 51(c) indicating the accuracy of the macromodel. It is interesting to note that for this example, the macromodel of subband 3 is required even if the frequency response only up to subband 2 is available. This was possible through the use of the G-type selector in subband 2.

4.6.2 Test Case 2: Frequency response from a known transfer function (high-order system)

The frequency response of three low pass $LP = 3$ and eight band pass $BP = 8$ filters in Table 4 discussed earlier was considered to check the performance of the proposed methods. The frequency response was equally divided into 10 subbands and was approximated using the estimated order $NS = DS - 1$ of 5 within each subband. Figure 52 shows the comparison between the frequency response of the known transfer function and the frequency response of the macromodel, which demonstrates that the methods proposed in this dissertation provide for accurate approximation of the frequency response for a high-order system. The extracted number of low-pass and

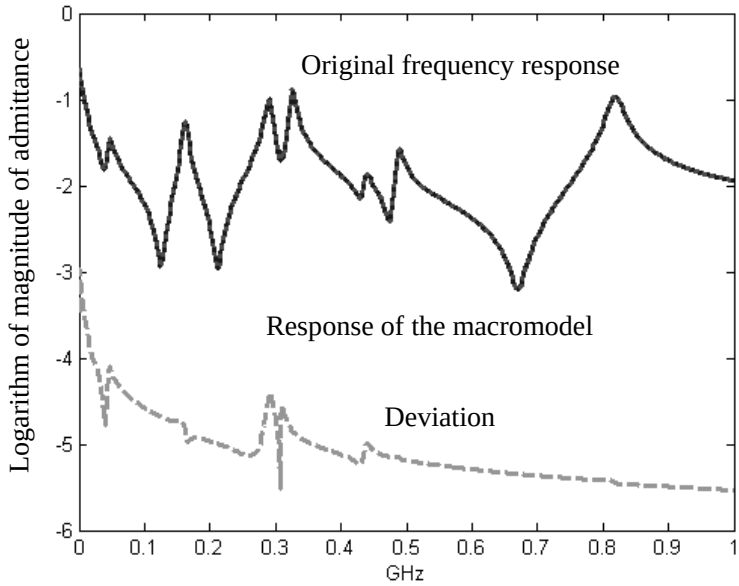

Figure 52: Performance of LSA for $LP = 3$ and $BP = 8$: the original frequency response (solid line) of the known transfer function, the frequency response (dotted line) of the macromodel, and the deviation (dashed line)

band-pass filters was $LP = 2$ and $BP = 8$, respectively.

4.6.3 Test Case 3: One-port lossy transmission line

To demonstrate the performance of the pole replacement method, the one-port admittance parameter for a lossy transmission line up to 2.5 GHz was considered. The frequency response was equally divided into 10 subbands having a bandwidth of 250 MHz and was approximated using the estimated order NS of 4 within each subband. Figure 53 shows the comparison between the original data and the frequency response of the macromodel. It is important to note that the number of original resonance peaks is roughly 32 and the estimated number of complex conjugate poles is 64. However, the number of complex conjugate poles and real poles extracted was 30 and 1, respectively, because the lower estimated order NS of 4 was used in each subband. It is obvious that there are many missing poles and spurious poles based on the comparison in Figure 53. After using the pole replacement method in each subband (number of iterations = 50) and over the entire computational domain (number

of iterations = 100), the missing poles were extracted and the spurious poles were discarded. The number of complex conjugate poles and real poles extracted was 66 and 4, respectively. Figure 54 shows the comparison between the original frequency data and the response of the macromodel after using the pole replacement method.

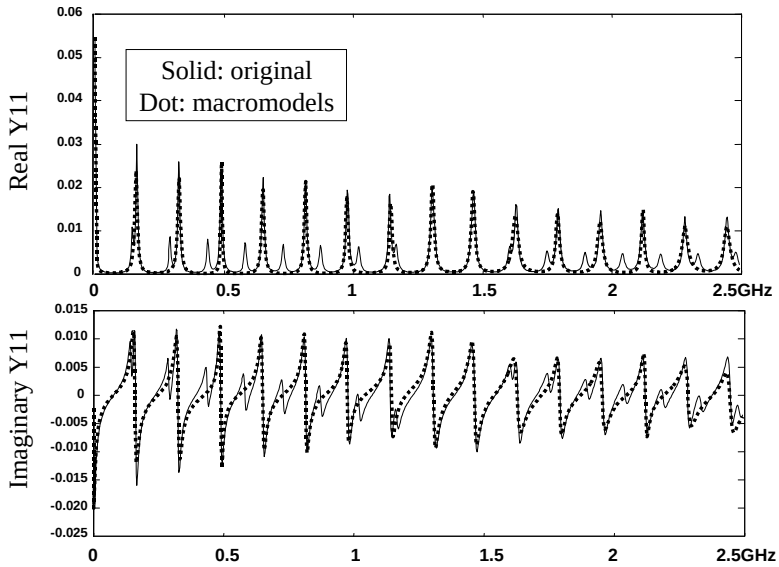

Figure 53: Passive macromodel without using the pole replacement method (NS = 4 and DS = 5 in each subband, number of iterations of the local pole replacement method = 0, number of iterations of the global pole replacement method = 0, number of complex conjugate poles = 30 and number of real poles = 1)

4.7 Automated Construction

For the automated construction of broadband macromodels, it is important to determine the subbands automatically. This can be achieved by detecting the location of resonant peaks and nulls in the frequency response, as shown in Figure 55. The details of the method are described below:

1. The process begins by assuming that the frequency samples are sorted from low to high frequency. The magnitude M_{prev} of the first frequency sample is set equal to zero although it has a non-zero value. This ensures the first frequency sample to be the left boundary of the first subband.

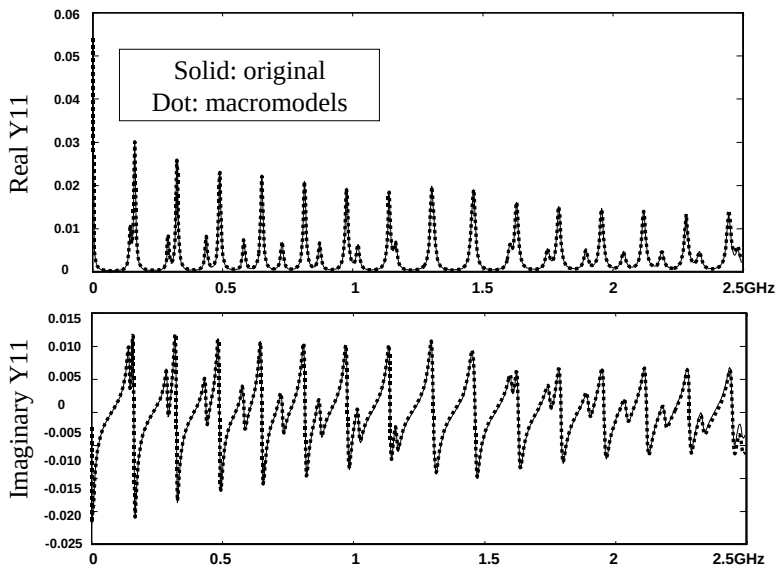

Figure 54: Passive macromodel using the pole replacement method ($NS = 4$ and $DS = 5$ in each subband, number of iterations of the local pole replacement method = 50, number of iterations of the global pole replacement method = 100, number of complex conjugate poles = 66 and number of real poles = 4)

2. The process computes the magnitude M_{next} of the next frequency sample. If $M_{prev} < M_{next}$, M_{next} is stored in M_{prev} and the process repeats the second step. If $M_{prev} \geq M_{next}$, M_{next} is stored in M_{prev} and proceeds to the next step. In this step, the maximum peak location of resonant peaks is detected.

3. The process computes the magnitude M_{next} of the frequency response of the next frequency sample. If $M_{prev} > M_{next}$, M_{next} is stored in M_{prev} and the process repeats the third step. If $M_{prev} \leq M_{next}$, the location and magnitude of the previous sample is stored in L_{min} and M_{min}, respectively. In this step, the interface between two resonant peaks is detected. The value L_{min} is set to the right boundary of the subband and left boundary of the next subband.

4. The process repeats the steps from 2 to 3.

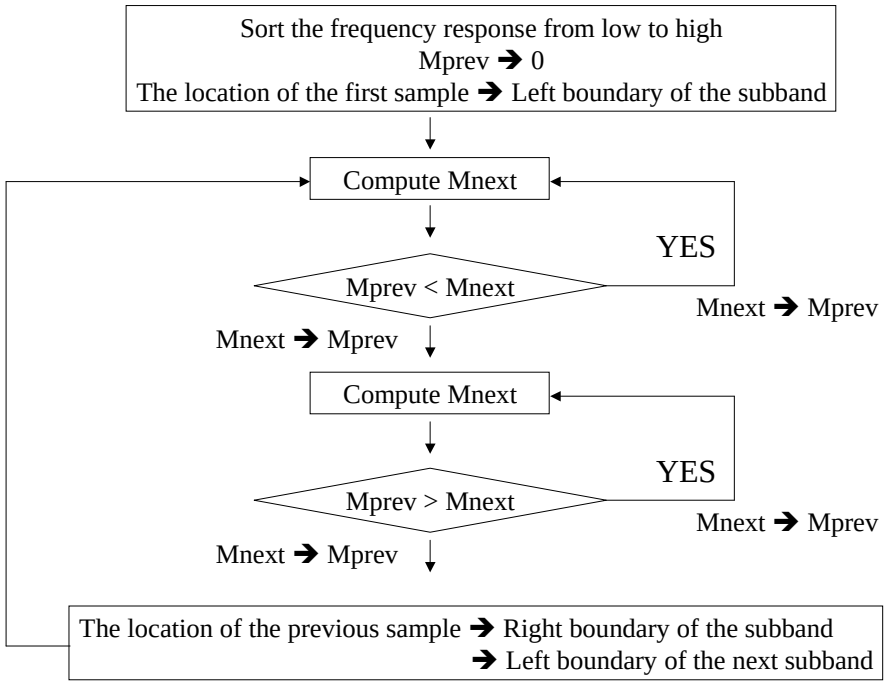

Figure 55: A flow chart for detecting the subbands

4.8 Multiport Construction

To estimate the construction time for a multiport macromodel, it is assumed that all numerator polynomials in $[Q(s)]$ for a N-port network in Equation (1.18) have the same order NS. Then, the size C of matrix $[A]^T[A]$ in Equation (1.7) for computing the common poles becomes:

$$C = NS \times \frac{N(N+1)}{2} + DS \tag{4.2}$$

For a matrix of size C, the required computation time is $O(2/3 \times C^3)$ using LU decomposition [66]. Hence, computation time of $\approx O(NS^3 \times N^6)$ is required for computing the coefficients of the denominator polynomial. For a large N, the construction time of the macromodel is dominated by the term N.

After multiplying the common denominator polynomial $P(s)$ on both sides in

Equation (1.15), the resulting equation becomes

$$\begin{bmatrix} H_{11}(s) & H_{12}(s) & \cdots & H_{1N}(s) \\ H_{21}(s) & H_{22}(s) & \cdots & H_{2N}(s) \\ \vdots & \vdots & \ddots & \vdots \\ H_{N1}(s) & H_{N2}(s) & \cdots & H_{NN}(s) \end{bmatrix} P(s) = \begin{bmatrix} Q_{11}(s) & Q_{12}(s) & \cdots & Q_{1N}(s) \\ Q_{21}(s) & Q_{22}(s) & \cdots & Q_{2N}(s) \\ \vdots & \vdots & \ddots & \vdots \\ Q_{N1}(s) & Q_{N2}(s) & \cdots & Q_{NN}(s) \end{bmatrix} \tag{4.3}$$

Without loss of generality, the denominator polynomial $P(s)$ can be computed using any rational function element $H_{ij}(s)$, which is an important property for a common pole system. Hence, the construction time of the macromodel can be reduced by selecting diagonal elements in the rational function matrix $[H(s)]$ since the diagonal elements contain the dominant behavior of the common poles, meaning that the poles of the off-diagonal elements are always a subset of the diagonal elements.

4.9 Model Order Reduction

For fast circuit simulation, it is important to reduce the order of the macromodel. According to the pole-residue representation used in this dissertation, the order of the macromodel used depends on the number of filters in the macromodel. Hence, the reduction in the order of the macromodel depends on the filters that can be eliminated.

In Section 4.2, two known transfer functions were approximated using least squares approximation. In Figure 41(b), residues of two complex conjugate poles have negligible values compared to the other residues, meaning that these two filters are redundant filters, and therefore do not have large effect on the accuracy of the macromodel. Hence, these two poles can be removed to reduce the order of the macromodel. In general, the filters having negligible residue values can be removed to reduce the order. It is important to note that this method does not violate either the stability or passivity condition since each filter in the macromodel satisfies these

Table 9: Output of model order reduction (MOR)

Ratio (percent)	Number of low pass filters	Number of band pass filters
0	3	48
1	3	18
5	3	10
10	2	6

conditions. Hence, the order of the macromodel can be reduced by eliminating filters based on the accuracy required.

4.9.1 Test Case: Frequency response from a power distribution network

The performance of the model order reduction method for reducing the order of the macromodel is demonstrated in this section using the frequency response from the INC board (Intelligent Network Communicator). This board contains a power plane pair, as discussed in the Chapter 5. A total of 1286 uniformly distributed frequency samples from 10KHz to 9GHz was approximated using the methods described in this chapter, which resulted in a two-port macromodel having 48 band pass filters and 3 low pass filters. Then, the magnitude of the frequency response of each filter was computed and the maximum magnitude value (MMV) for 51 filters was stored as a reference. This was required since the ratio of the maximum magnitude of other filters to MMV was used for removing spurious filters. For example, since the magnitude of 38 band pass filters of the 48 band pass filters shown in Table 9 is less than 5 percent of MMV, the 38 band pass filters are filters that can be eliminated. The frequency response of the macromodels in Table 9 is shown in Figure 56.

The macromodels in Table 9 were simulated to obtain the voltage fluctuation on the power plane using HSPICE [61] with the configuration shown in Figure 57. The macromodel was connected to a 3.3V dc source (port 1) and the VDD node (port 2) of a differential driver with 0.5ns rise and fall times, as shown in Figure

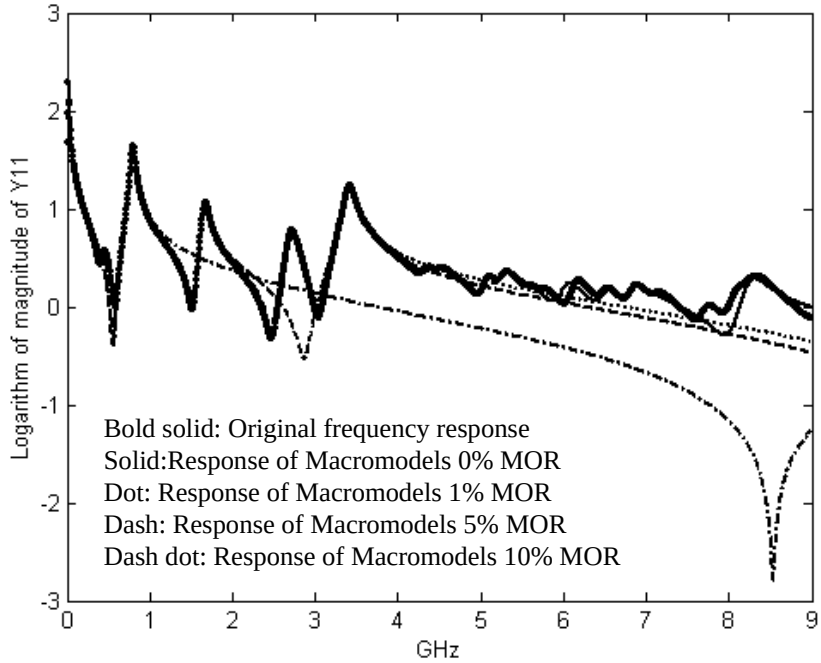

Figure 56: Frequency response after removing spurious filters: original data (bold solid), response of the macromodel with 0 percent MOR (solid), response of the macromodel with 1 percent MOR (dot), response of the macromodel with 5 percent MOR (dash) and response of the macromodel with 10 percent MOR (dash dot)

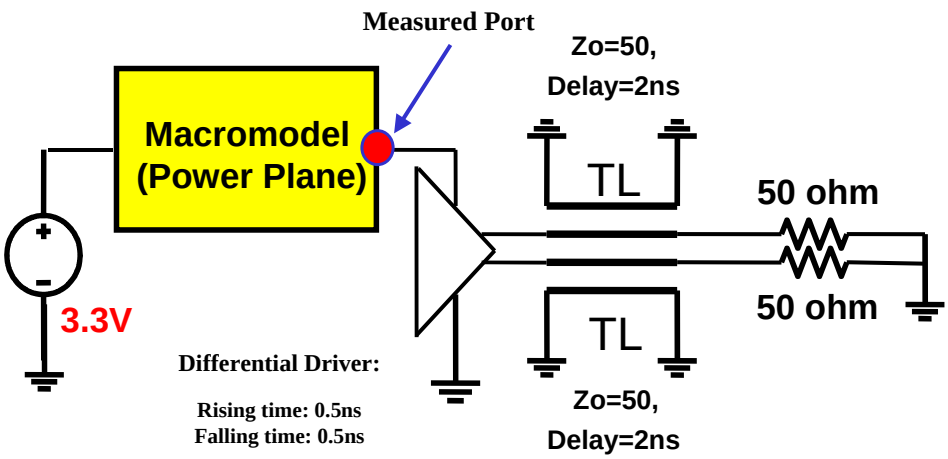

Figure 57: Circuit simulated

57. A transmission line having a 50Ω characteristic impedance and 2ns delay and terminated with a 50Ω resistor was connected to the output of the driver. The time-domain voltage fluctuation at port 2 is shown in Figure 58, which demonstrates that the method for reducing the order of the macromodel does not violate the stability and passivity conditions. Since the waveform of the macromodel with 5 percent MOR at port 2 provides a result similar to the waveform of the macromodel with 0 percent MOR, a 75 percent reduction can be achieved using the method discussed in this section.

4.10 Broadband Efficient Macromodeling Program

The methods discussed in this dissertation have been incorporated into the Broadband Efficient Macromodeling Program (BEMP) developed at Georgia Tech. The program was developed using C++ language (10,000 lines) and is executable on a Windows operating system. The algorithm for BEMP is shown in Figure 59.

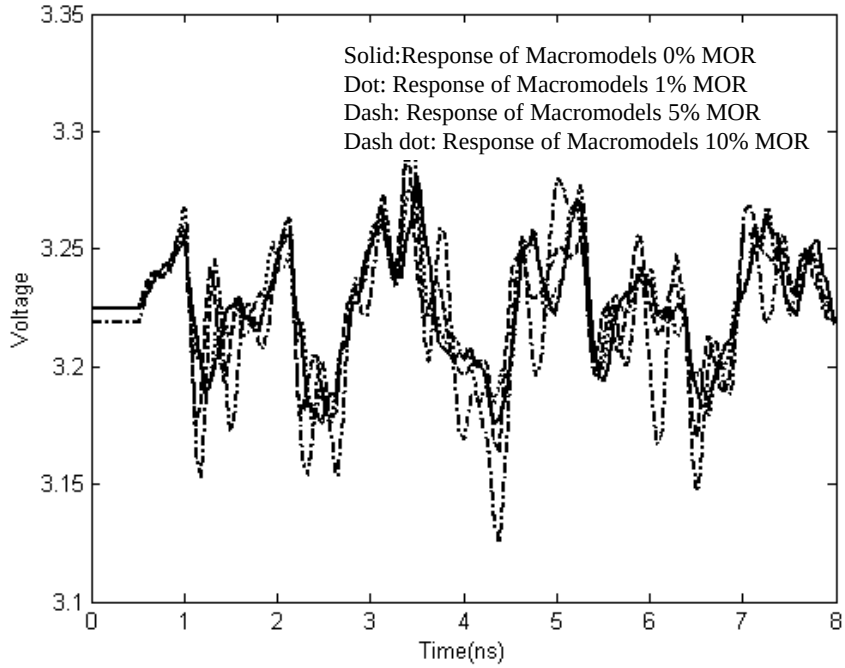

Figure 58: Time-domain simulation

4.11 Summary

For the construction of broadband passive macromodels, efficient methods were developed based on the concept that a passive system can be represented as a summation of passive sub-systems. The methods developed in this chapter are band division, selector, subband reordering, subband dilation, and pole replacement. The major advantage of these methods are that they can be applied to distributed interconnect networks that often require many poles for approximation.

The broadband macromodel was constructed using band division, which divides the entire computational domain into sub-computational domains. Numerically, the band division method alleviates the ill-conditioned matrix problem arising in least squares approximation. In addition, the method reduces the memory requirement. However, there are interactions between subbands since the sub-macromodel from each subband produces a non-zero frequency response in other subbands. This band

INITIALIZATION **:**

load original admittance parameters ***Ho*** and the frequency ***fo***
load subbands ***BD*** (Band Division)
load estimated orders ***NS*** *and* ***DS***
initialize poles and residues

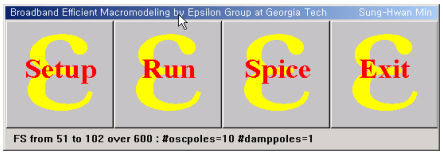

LOCAL LOOP **:**

for n=1 **to** *the number of subbands*
  set sub-computational domain ***SCD*** = ***BD***(n) (Subband Reordering)
  apply the R-type selector on poles and resides
  calculate the frequency response ***Hm*** using poles and residues over the ***SCD***
  calculate ***He*** = ***Ho*** **-** ***Hm*** and **save** ***Hg*** = ***He*** and max***Hg*** over the ***SCD***
  initialize good-sub-poles and good-sub-residues
  for num, den = a range of estimated orders ***NS*** and ***DS***
    initialize sub-poles and sub-residues
    do frequency scaling on ***fo*** (Frequency Scaling)
    calculate the denominator coefficients using least squares approximation
    construct stable sub-poles from the denominator coefficients
    undo frequency scaling on stable sub-poles
    calculate sub-residue matrices of sub-poles
    calculate the residues $[\delta]$ and $[\eta]$
    apply multiport passivity formulae
    if there is a violation, **compensate** negative eigenvalues, **end**
    calculate the frequency response ***Hm*** using sub-poles and sub-residues
    calculate ***Hs*** = ***He*** **-** ***Hm*** over the ***SCD***
    if max***Hg*** > max***Hs*** based on error criterion
      save max***Hg*** = max***Hs***
      save good-sub-poles = sub-poles, good-sub-residues = sub-residues
    end
    apply appropriate selectors on good-sub-poles and good-sub-residues
    add good-sub-poles and good-sub-residues **to** poles and residues
  end
  apply subband dilation and pole replacement methods over the ***SCD***
end

GLOBAL LOOP **:**

for n=1 **to** *the number of global optimization*
  apply the pole replacement method over the entire frequency band
  update the residues $[\delta]$ and $[\eta]$
end
generate SPICE net lists

Figure 59: Flow chart of BEMP

interaction has been solved using selectors, which selects the filters extracted from the subband of interest, subband reordering, which provides a construction sequence for reducing the interaction between subbands, subband dilation, which provides local correction in the boundary region between subbands, and pole replacement, which increases the accuracy of the macromodel.

A method, which automatically determines the boundaries of each subband, has been developed by detecting the resonant peaks and nulls in the frequency response. The construction time of the macromodel has been reduced by using diagonal elements in the rational function matrix since off-diagonal elements are always a subset of the diagonal elements in the common pole system. In addition, a method for reducing the order of the macromodel without affecting the stability and passivity conditions has been developed by removing the filters with negligible residue values.

The performance of the band division and subband reordering methods using selectors was demonstrated through known transfer functions. In addition, the performance of the pole replacement method was demonstrated using the frequency response of a one-port transmission line. Details on the performance of the methods discussed in this chapter using several test cases representative of distributed interconnect networks are discussed in the next chapter.

CHAPTER V

EXAMPLES AND TEST CASES

To demonstrate the validity of the methods discussed in Chapter 4, several test cases representative of distributed interconnect networks have been presented. The macromodels of these test cases have been constructed using BEMP.

5.1 Test Case 1: Four-port lossy coupled transmission line

Figure 60 shows the transmission line with its self and coupling parameters, which was modeled using the W-element transmission lines in HSPICE [61], which is a commercially available circuit simulator.

The frequency response (admittance parameters) for a four-port coupled transmission line with length of 0.43cm, which has uniformly distributed frequency samples from 0.1 MHz to 1.0 MHz (5 samples) and from 10.0 MHz to 10.0 GHz (4000 samples), was generated using HSPICE. Using the band division method, the entire frequency domain was divided into 80 uniform subbands without overlapping subbands. Each subband had 50 frequency samples. The first subband was again divided into two smaller subbands having 10 samples and 40 samples, respectively. The number of local and global iterations for the pole replacement method was 3 and 50, respectively. Using the estimated orders NS of 4 and DS of 5 within each subband, the number of complex conjugate poles and real poles extracted was 240 and 3, respectively. The comparison between original data and the frequency response of the constructed macromodel for Y14 admittance parameter over a bandwidth of 10.0 GHz is shown in Figures 61 and 62.

A Lossy Coupled Transmission Line (W-element model in HSPICE)

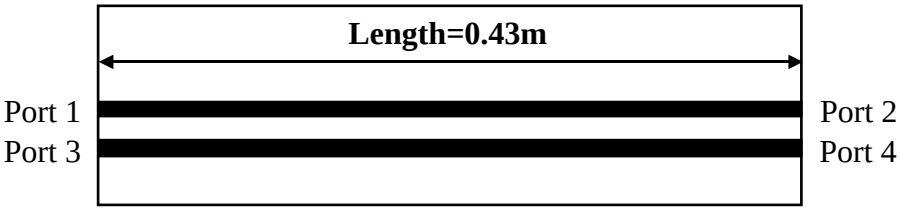

Self and coupling parameters in W-element

$$L_O[\mu H] = \begin{bmatrix} 2.311 & 0.414 \\ 0.414 & 2.988 \end{bmatrix} \qquad R_S[\Omega] = \begin{bmatrix} 0.00135 & 0 \\ 0 & 0.001303 \end{bmatrix}$$

$$C_O[pF] = \begin{bmatrix} 23.92 & -5.41 \\ -5.41 & 21.23 \end{bmatrix} \qquad G_O[\Omega^{-1}] = \begin{bmatrix} 0.000609 & -0.0001419 \\ -0.0001419 & 0.000599 \end{bmatrix}$$

$$R_O[\Omega] = \begin{bmatrix} 42.5 & 0 \\ 0 & 41.0 \end{bmatrix} \qquad G_D[\Omega^{-1}] = \begin{bmatrix} 5.242\times10^{-13} & -1.221\times10^{-13} \\ -1.221\times10^{-13} & 5.164\times10^{-13} \end{bmatrix}$$

Figure 60: Lossy coupled transmission line

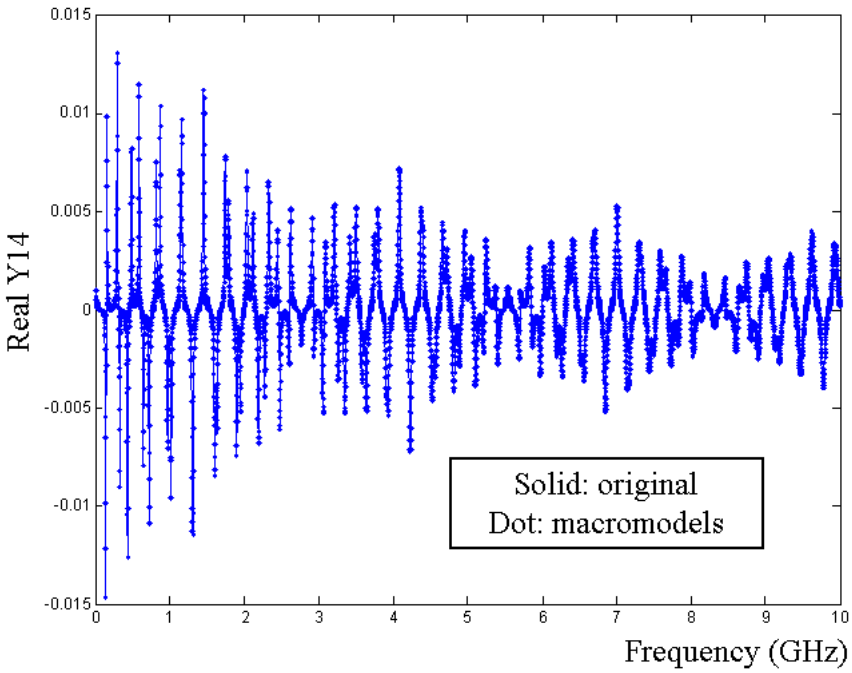

Figure 61: Comparison of the real part of Y14 (admittance)

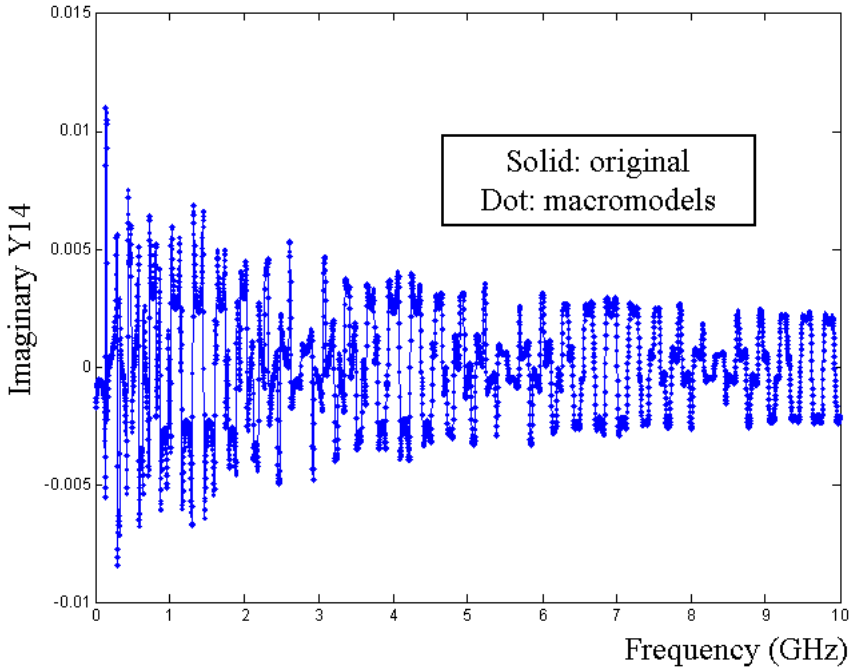

Figure 62: Comparison of the imaginary part of Y14 (admittance)

To demonstrate the passivity of the macromodel, four eigenvalues are shown in Figure 63, which are all greater than zero.

To show the difference between the stable and passive macromodel, the stable macromodel of the transmission line in Figure 60 was constructed without enforcing the passivity condition. Then, the macromodel was synthesized into an equivalent circuit and simulated in HSPICE. A trapezoidal current source with 0.1ns rise and 0.2ns fall times was excited at port 1. Resistors with a 30Ω value were terminated at ports 2 and 4. A 30Ω resistor and a transmission line having a 50Ω characteristic impedance and 1.2ns delay were terminated at port 3 in series, as shown in Figure 64.

During time-domain simulation, the macromodel violated the passivity condition producing a diverging result, as shown in Figure 65. The circles in Figure 65 represent the waveform at the corresponding ports of the macromodel.

Using the passive macromodel constructed using BEMP, the time-domain

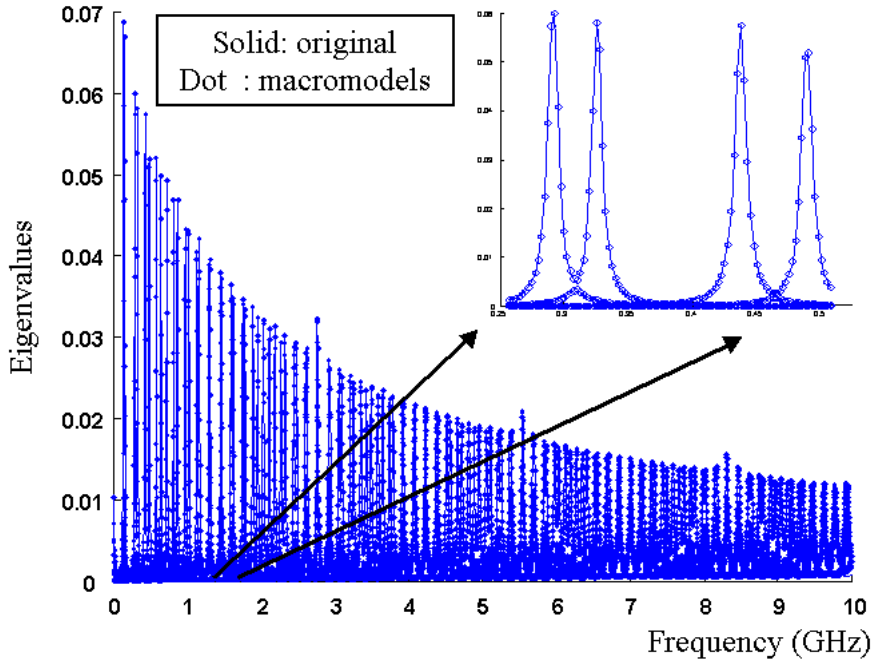

Figure 63: Comparison of four eigenvalues vs. frequency between original data and the frequency response calculated from the macromodel

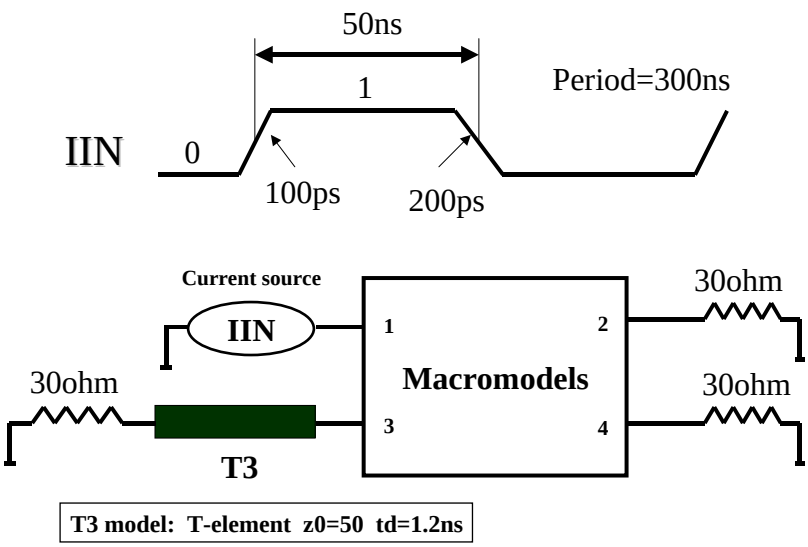

Figure 64: Circuit simulated

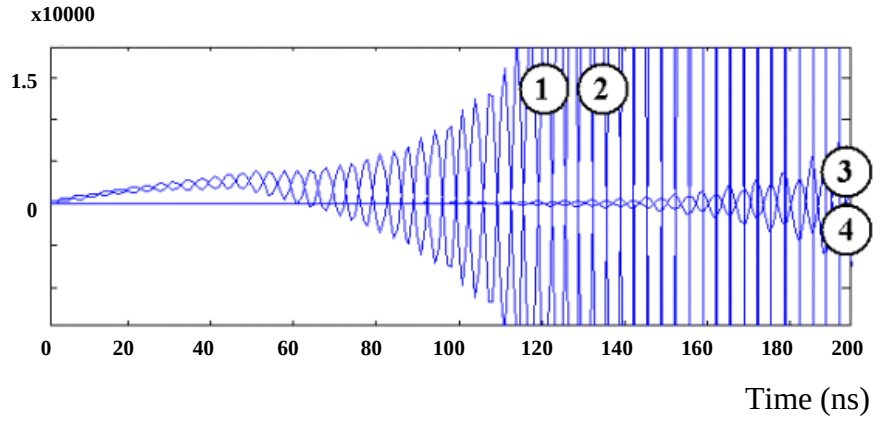

Figure 65: Time-domain simulation of the non-passive macromodel

waveform of the original network and the passive macromodel is compared from 0 to 200ns in Figure 66. The macromodel shows good agreement with the HSPICE result.

5.2 Test Case 2: Four-port transmission line data from measurement

A total of 799 uniformly distributed frequency samples from 50.0 MHz to 20.0 GHz for a 4-port transmission line was measured by Rambus using a vector network analyzer. The entire frequency band was divided into 16 subbands having a bandwidth of 1.25 GHz. The macromodel was constructed from the lower subband using the orders NS of 8 and DS of 9 in all subbands. The number of local and global iterations for the pole replacement method was 2 and 200, respectively. The number of complex conjugate poles and real poles extracted were 224 and 1, respectively. Figures 67 and 68 show the comparison between original frequency data and the response of the constructed macromodel for real (Y11) and imaginary (Y12) admittance parameters, respectively.

The macromodel was connected to a 400mV source having 50ps rise/fall times and a 50Ω termination at port 1. Resistors with a 50Ω value were terminated at ports

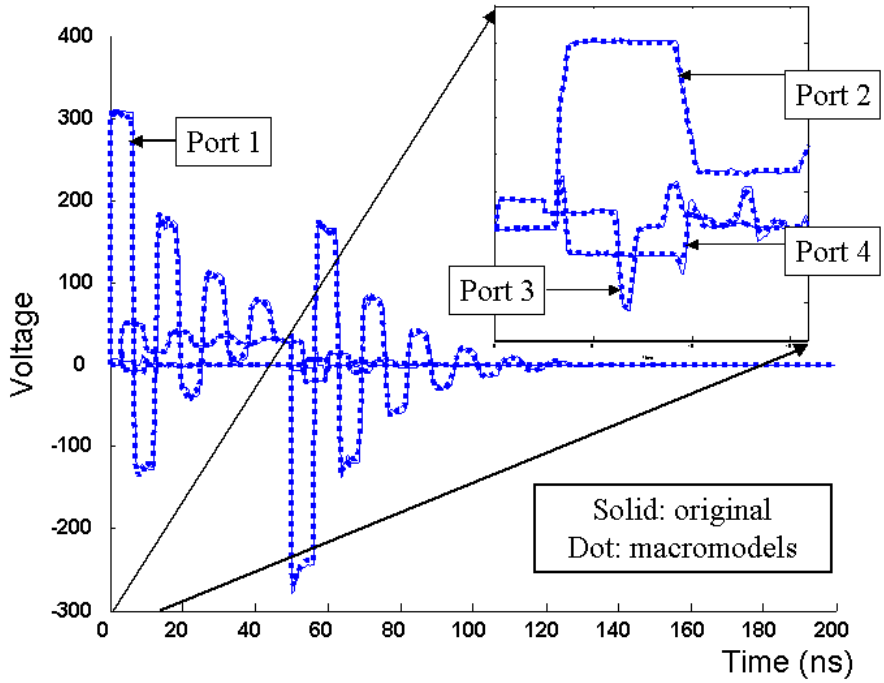

Figure 66: Time-domain comparison between a lossy coupled transmission line and the passive macromodel

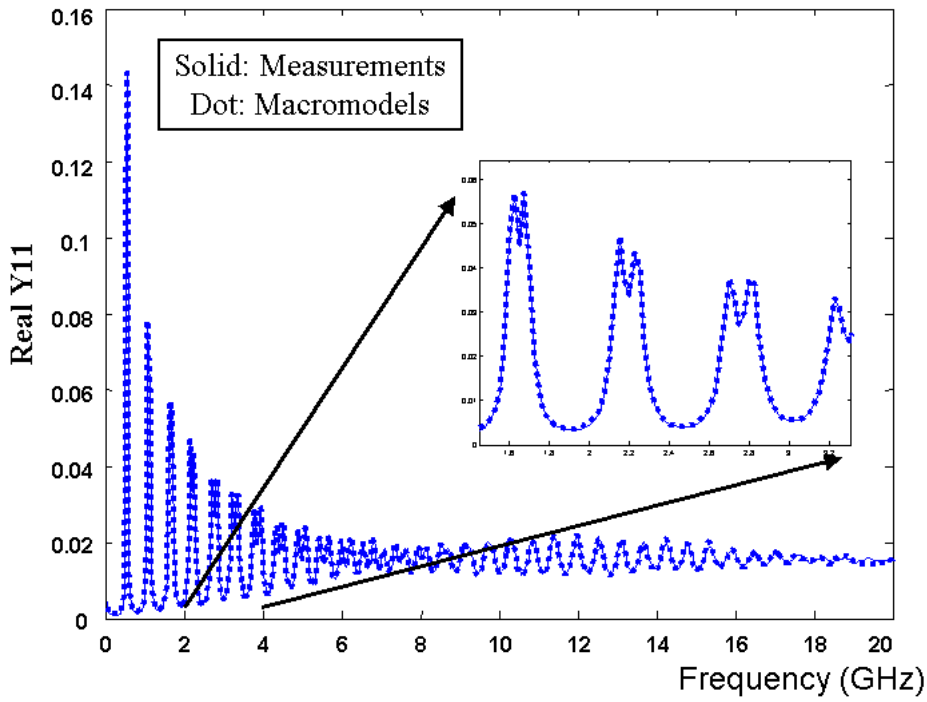

Figure 67: Comparison of real part real of admittance parameter Y11

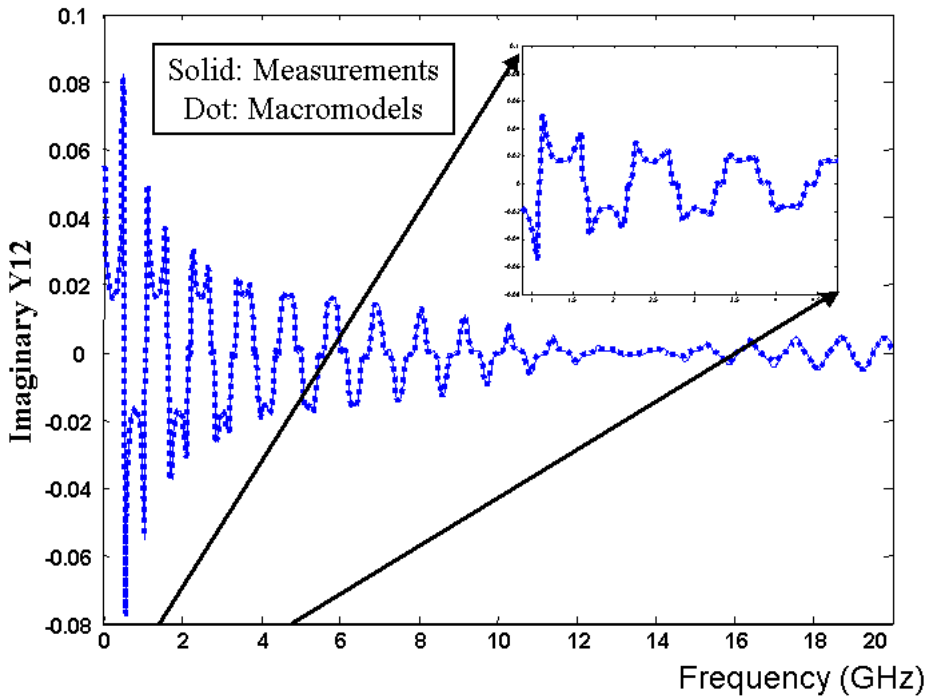

Figure 68: Comparison of imaginary part of admittance parameter Y12

2, 3, and 4, as shown in Figure 69. The time-domain waveform at ports 1 and 2 are shown from 0 to 30ns in Figure 70, demonstrating stability and passivity.

5.3 Test Case 3: Four-port power plane pair with decoupling capacitors

A 4.0in x 6.0in power plane pair with a dielectric thickness of 62mil is shown in Figure 71. Six decoupling capacitors represented as RLC circuit elements, where 'R' and 'L' are the series equivalent resistance and inductance of the capacitor, respectively, were connected to the power plane.

A total of 1000 uniformly spaced samples was generated from 1.0 MHz to 4.0 GHz using the cavity resonator model described in [49]. Although the frequency response of the power plane pair with decoupling capacitors is highly irregular, the entire frequency domain for admittance parameters was divided into 20 uniform subbands having 50 samples per subband without overlapping subbands. The number of local

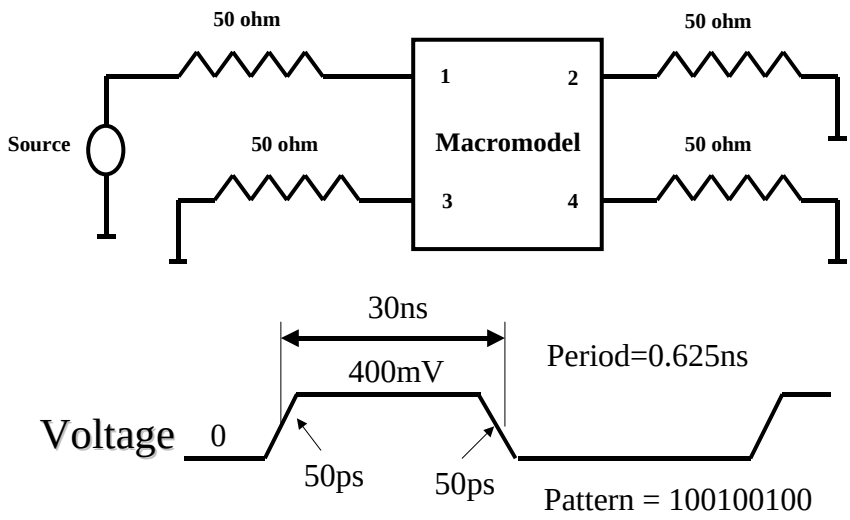

Figure 69: Circuit simulated

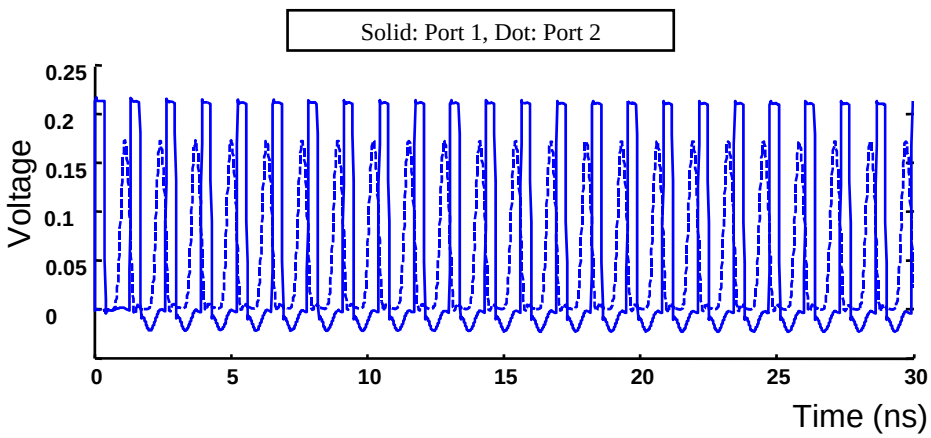

Figure 70: Time-domain waveform

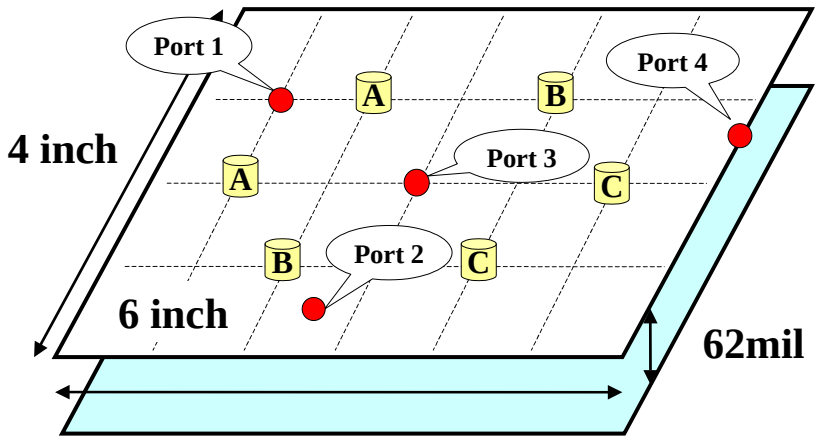

Dielectric Properties: Er=5.05 Loss tangent=0.018 Conductivity=5.7e+7
Decoupling Capacitors:

A:	**C=130.00pF**	**L=0.4580nH**	**R=373.4mOhm**	**Resonant Freq=650MHhz**
B:	**C=304.69pF**	**L=0.4130nH**	**R=148.6182mOhm**	**Resonant Freq=450MHz**
C:	**C=1.3167nF**	**L=0.5093nH**	**R=335.875mOhm**	**Resonant Freq=190MHz**

Figure 71: A power plane pair with decoupling capacitors

and global iterations for the pole replacement method was 1 and 200, respectively. Using the orders NS of 4 and DS of 5 within each subband, the number of complex conjugate poles and real poles extracted was 78 and 1, respectively. The comparison between original data and the frequency response of the constructed macromodel for admittance parameters over a bandwidth of 4.0 GHz is shown in Figures 72 and 73.

The macromodel of the power plane with decoupling capacitors was simulated to obtain the voltage fluctuation on the power plane using the configuration shown in Figure 74. The macromodel was connected to a 2.5V dc source (port 1) and the VDD node (port 4) of a linear driver with 0.7ns rise and 0.3ns fall times. A transmission line having a 50Ω characteristic impedance and 1.2ns delay, and a 50Ω resistor were connected in series between the output of the driver and the common ground of the power plane. The time-domain voltage fluctuations at ports 2 and 4 are shown in Figure 75, which demonstrates that the macromodel is stable and passive.

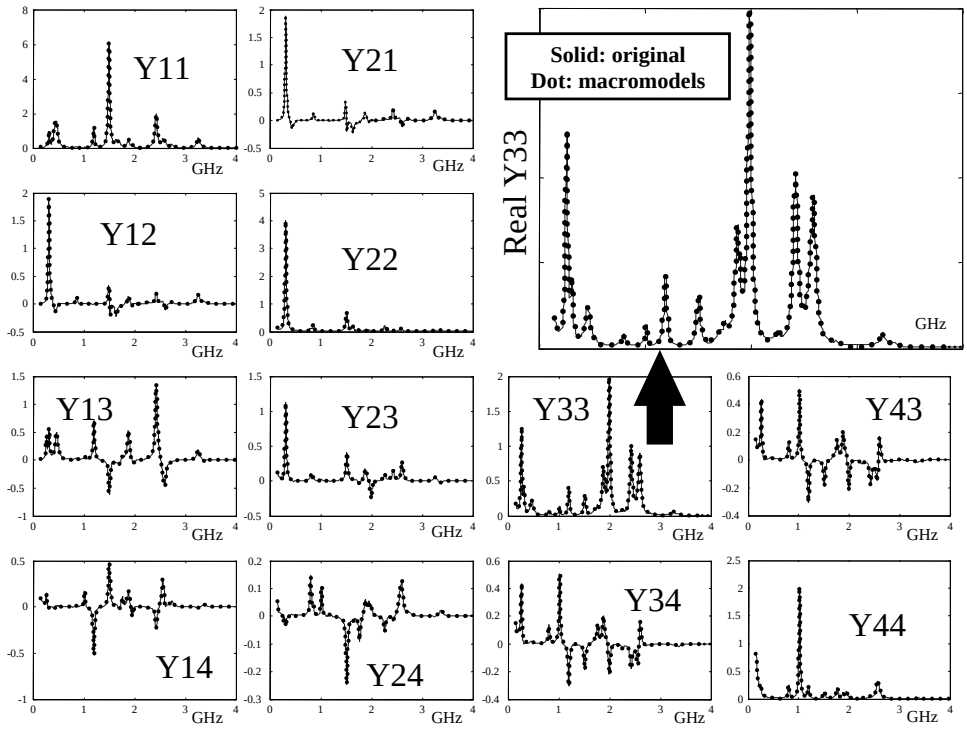

Figure 72: Comparison of real part of admittance parameters for a power plane with decoupling capacitors

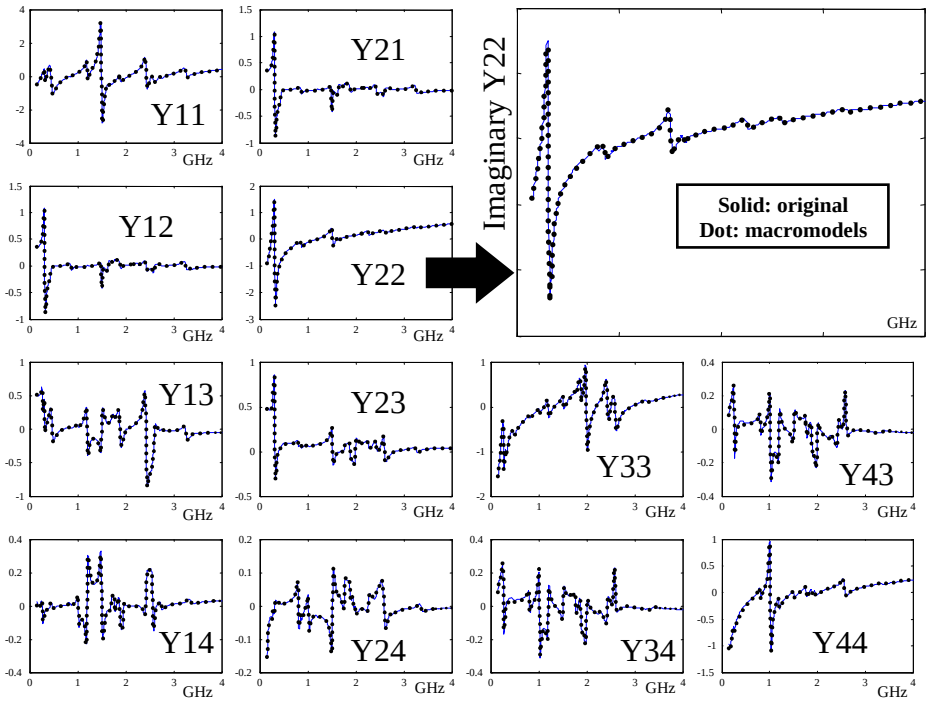

Figure 73: Comparison of imaginary part of admittance parameters for a power plane with decoupling capacitors

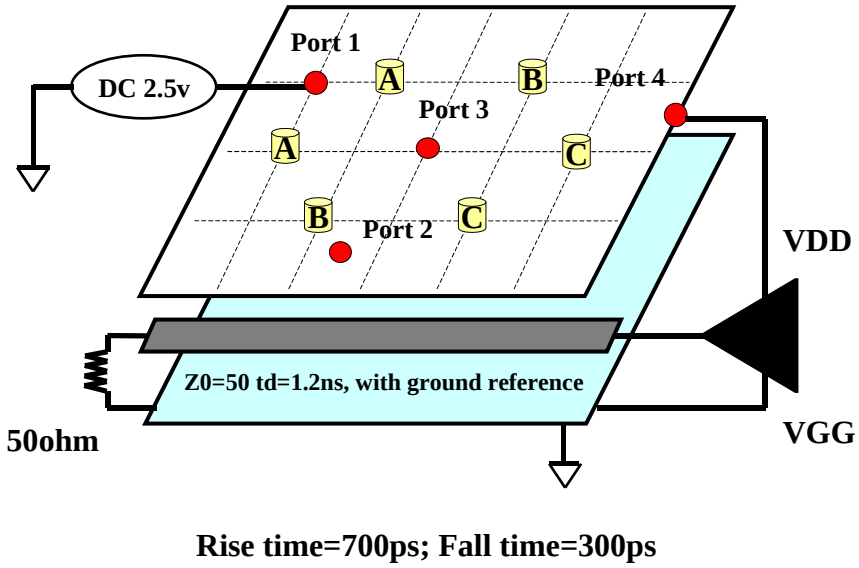

Figure 74: Circuit simulated

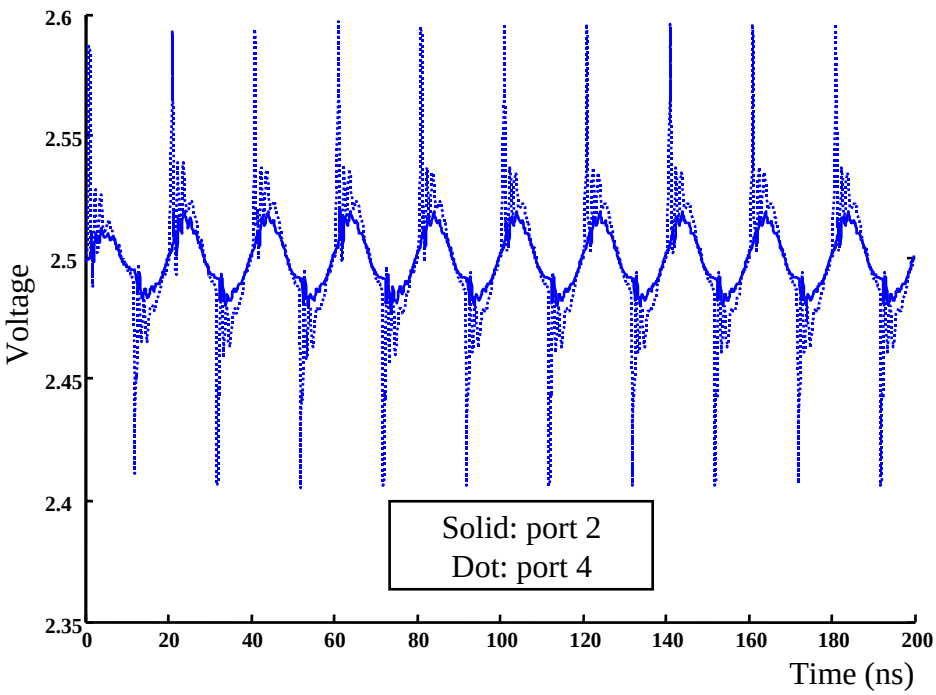

Figure 75: Time-domain simulation of a power plane pair with decoupling capacitors

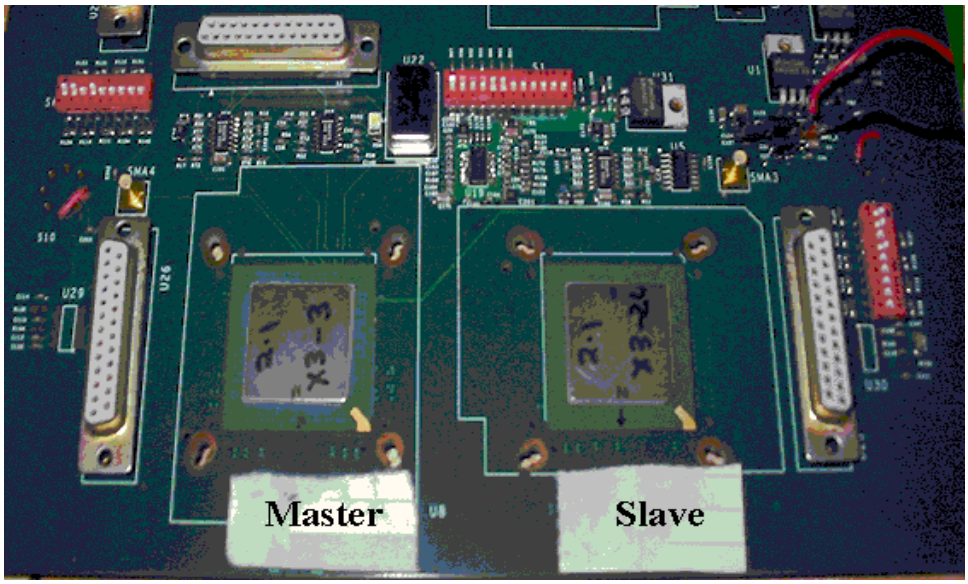

Figure 76: Yellowstone test vehicle from Rambus

5.4 Test Case 4: Power distribution network from Rambus

Figure 76 shows a test board from Rambus, which consists of transmitter and receiver chips placed on a wirebond plastic ball grid array (PBGA) package [71]. This system was designed for chip-to-chip communication at a data rate of 3.2 Gbps. The PBGA package is directly attached to a 12.8in x 9.5in board using solder balls or sockets. The cross section of the board is shown in Figure 77, which has two signal layers, two power planes, and two ground planes. The detail of the board is described as follows:

Layer 1 is a low-speed signal layer. The low-speed signal transmission lines are single ended and their characteristic impedances are designed for 50Ω using trace width of 7.0mil, trace spacing of 18.0mil, and trace thickness 0.75mil.

Layer 2 is a continuous ground plane of thickness 1.5mil.

Layer 3 is a power plane that provides 5.0V to the peripherals on the board. It also has two irregularly shaped power islands of 1.2V, called master and slave

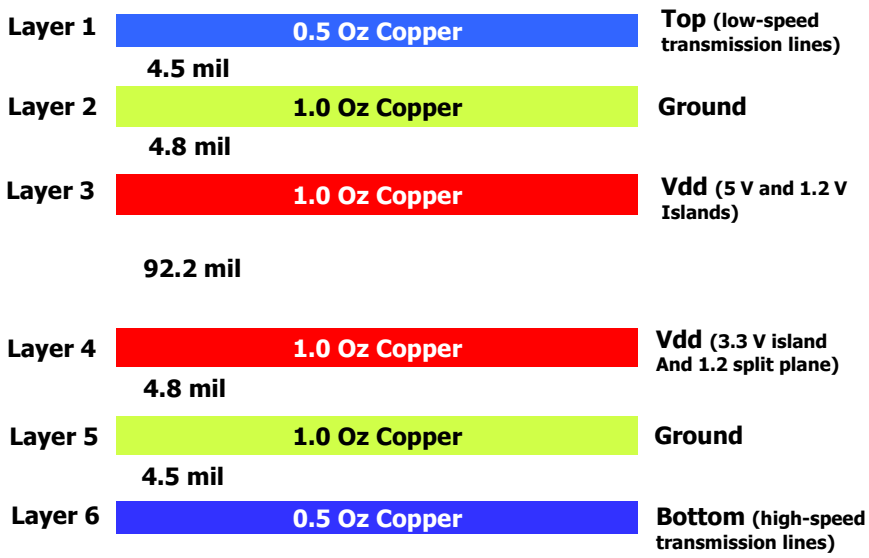

Figure 77: Cross section of the board

islands, to supply voltage to the transmitter and receiver chips on the board, respectively.

Layer 4 is a 1.2V split power plane which serves the master and slave sections and includes a small island at the center with 3.3V to supply voltage to the clock generator chip. These two split planes are connected using a jumper.

Layer 5 is a continuous ground plane. The thickness of the plane is 1.5mil.

Layer 6 is a high-speed signal layer. The high-speed signal transmission lines are differential and their characteristic impedances are designed for 100Ω using trace width of 6.0mil, trace spacing of 11.5mil, and trace thickness of 0.75mil.

The conductor in the six layers is copper with conductivity, $\sigma_c = 5.8 \times 10^7 S/m$. The dielectric material of the board is FR4 with a relative permittivity, $\epsilon_r = 4.5$, and dielectric loss tangent, $tan\delta = 0.02$ at 1.0 GHz.

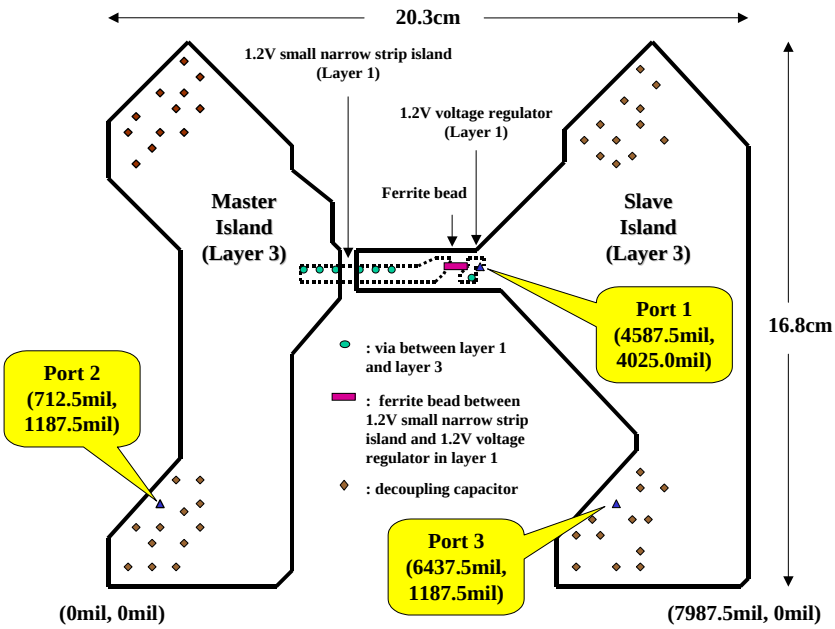

Figure 78: Top view of the test vehicle

Figure 78 shows the top view of the test vehicle, which has two irregularly shaped master and slave islands. The two islands in layer 3 are connected to a small narrow strip power island and a 1.2V voltage regulator in layer 1 through 7 vias. For reducing power supply noise, a ferrite bead of inductance 120nH and 48 decoupling capacitors mounted on layer 1 were used. The power planes were excited and measured at three ports as shown in Figure 78. In the figure, port 1 is the location of the voltage regulator module, and port 2 and port 3 are the locations of the master and slave chips, respectively.

The irregular power plane was discretized as rectangular grids having a unit cell size of 0.385cm x 0.385cm, which corresponds to an electrical size of $\lambda/13$ at 6.0 GHz. This resulted in 1,087 unit cells for approximating the structure, which included the narrow rectangular strip in layer 1, the continuous ground plane in layer 2, and the split power plane in layer 3. The seven vias connecting layers 1 and 3 were represented as short circuits.

Using the transmission matrix method (TMM) [50], three-port impedance parameters of the power plane pair shown in Figure 78 were generated and stored from 10.0 KHz to 6.0 GHz. These were converted into admittance parameters for the construction of the broadband macromodel. Using the band division method, the frequency response was divided into irregular subbands because the admittance parameters had a highly unbalanced amplitude, which varied from 7.4498×10^{-9} to 227.6 [mho] from DC to 6.0 GHz. The number of complex conjugate poles and real poles extracted was 150 and 4, respectively. The comparison between the original frequency response and the response of the macromodel is shown in Figure 79, which shows good agreement between the frequency data and the response of the macromodel. Using the constructed macromodel, the frequency response from DC to 10MHz is shown in Figure 80(a) for Y11, Y12, and Y22. In addition, the extrapolated frequency response from 5GHz to 15GHz is shown in Figure 80(b) for Y11, Y12, and Y22.

The comparison between the three eigenvalues from the original frequency response and the response of the constructed macromodel over a 6.0 GHz bandwidth is shown in Figure 81. The eigenvalues are all greater than or equal to zero, which demonstrates passivity and accuracy of the macromodel.

The time-domain simulation was performed in HSPICE using the three-port macromodel of the power planes, differential drivers, and transmission lines for computing power supply noise, as shown in Figure 82. For representing four differential drivers with 50ps rise and fall times connected to four differential transmission lines with 100Ω characteristic impedance and 1ns delay, the driver model used was a time-dependent resistive switch. A transmission line model available in HSPICE was used to represent the transmission lines. The far ends of the transmission lines referenced to the ground plane were terminated in 50Ω and connected to a 0.3V dc source, which provides the communication path between the master and slave chips. The two ground planes were connected to each other using numerous vias. Port 3 representing a 1.2V

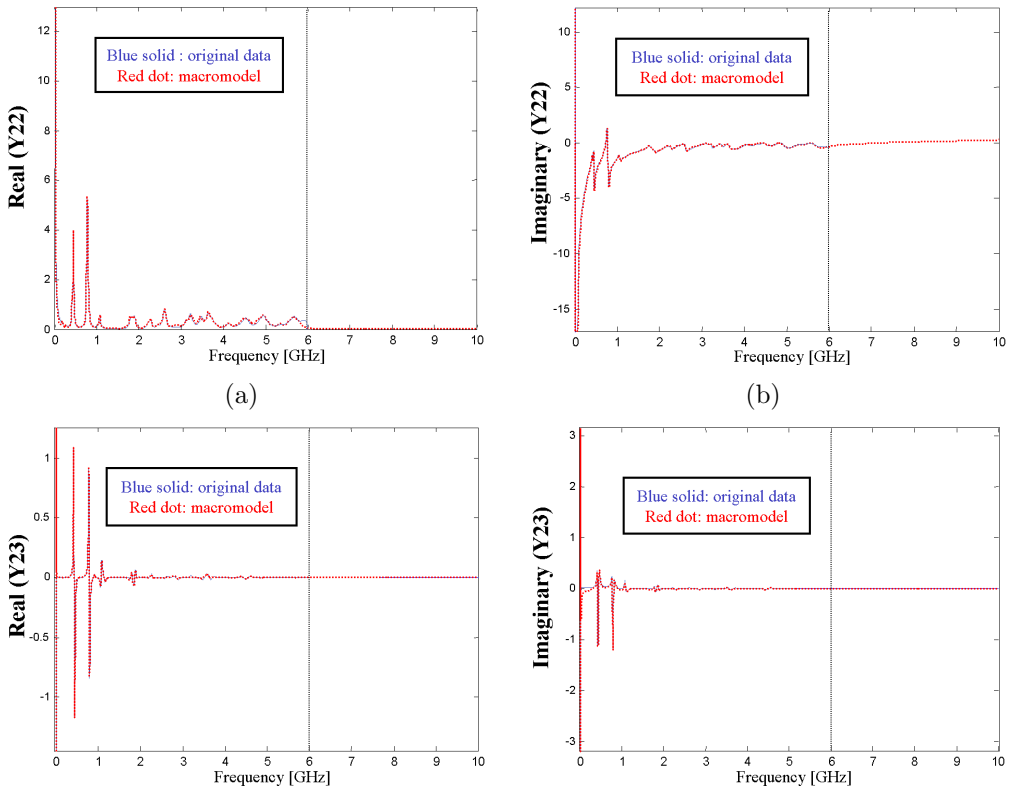

Figure 79: Comparison of admittance parameters: (a) real of Y22, (b) imaginary of Y22, (c) real of Y23 and (d) imaginary of Y23

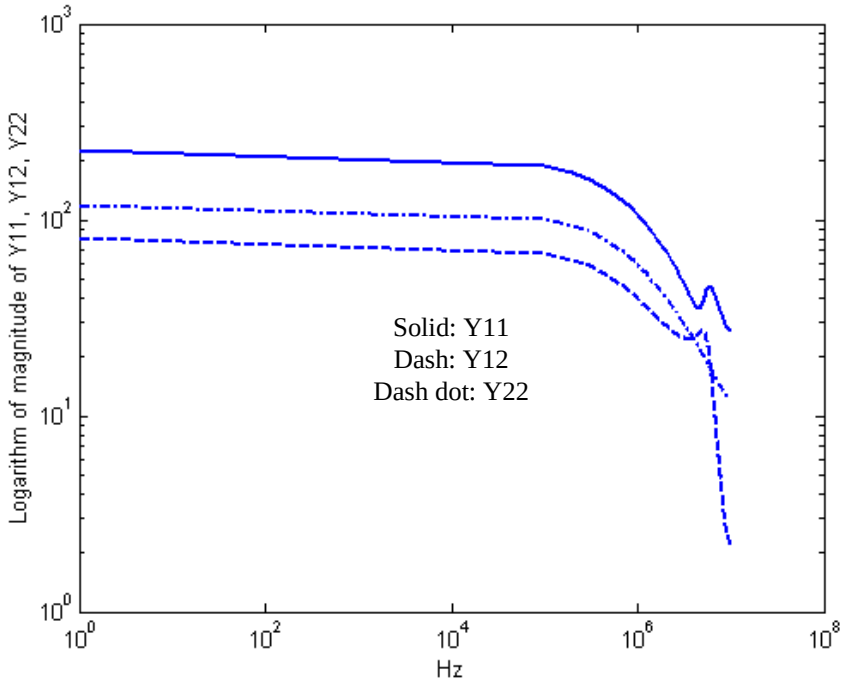

(a)

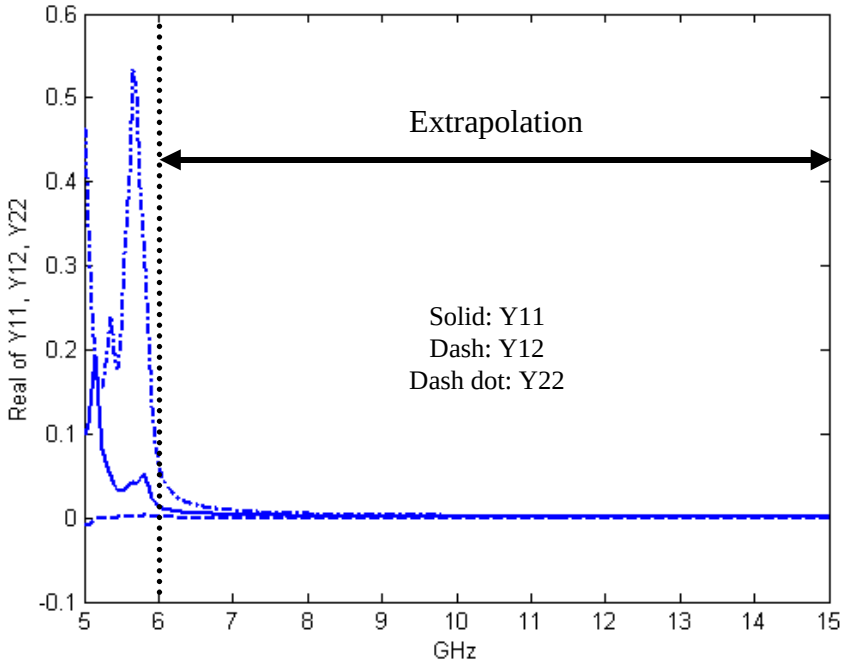

(b)

Figure 80: Admittance parameters (Y11, Y12, Y22) generated from the constructed macromodel: (a) from DC to 10MHz and (b) from 5GHz to 15GHz

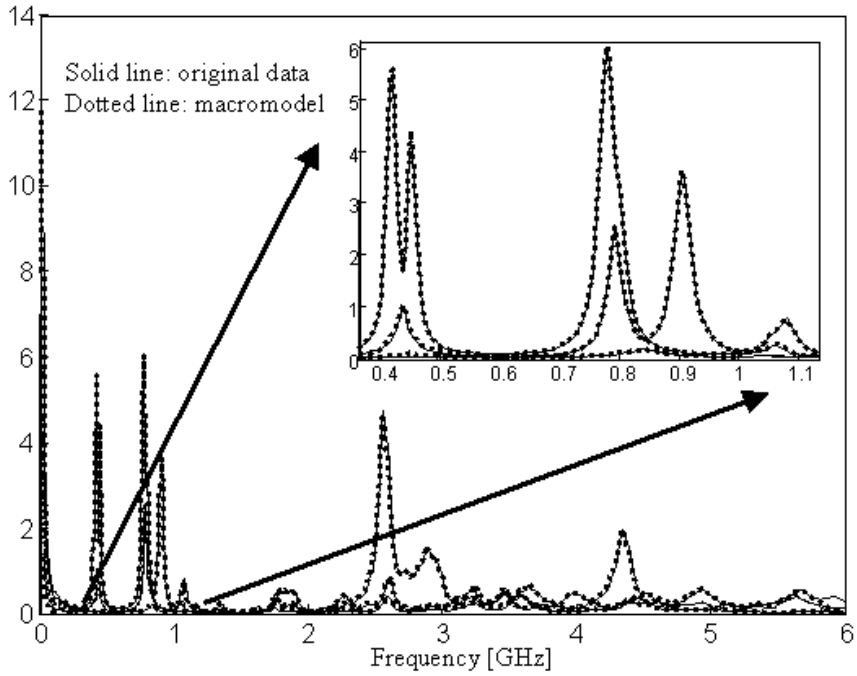

Figure 81: Comparison of three eigenvalues vs. frequency between original data and the frequency response calculated from the macromodel

dc source for the slave chip was left unterminated. The voltage regulator module with 0.6V supply voltage was connected between port 1 and ground.

The time-domain waveform of power supply noise between port 2 and ground is shown in Figure 83. The bit pattern of the waveform is 0000111100001111..., resulting in a data speed of 3.2 Gbps/pair with a voltage swing of 271mV. From Figure 83, a power supply noise of 40mV was measured due to the switching of four differential transmission lines. The power supply noise is uniform over a time duration of 20ns, indicating that the macromodel is stable and passive.

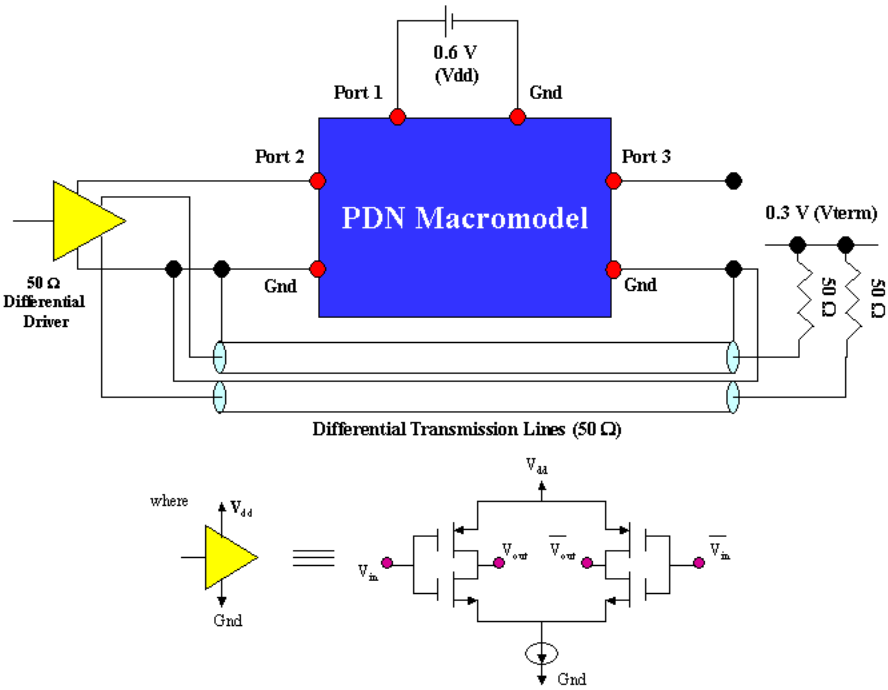

Figure 82: Circuit simulated

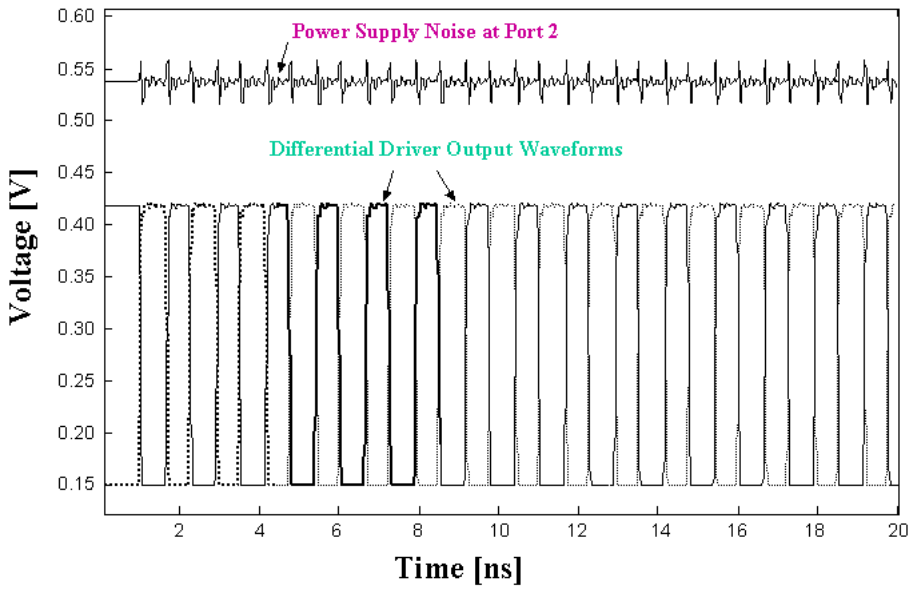

Figure 83: Time-domain simulation for measuring power supply noise

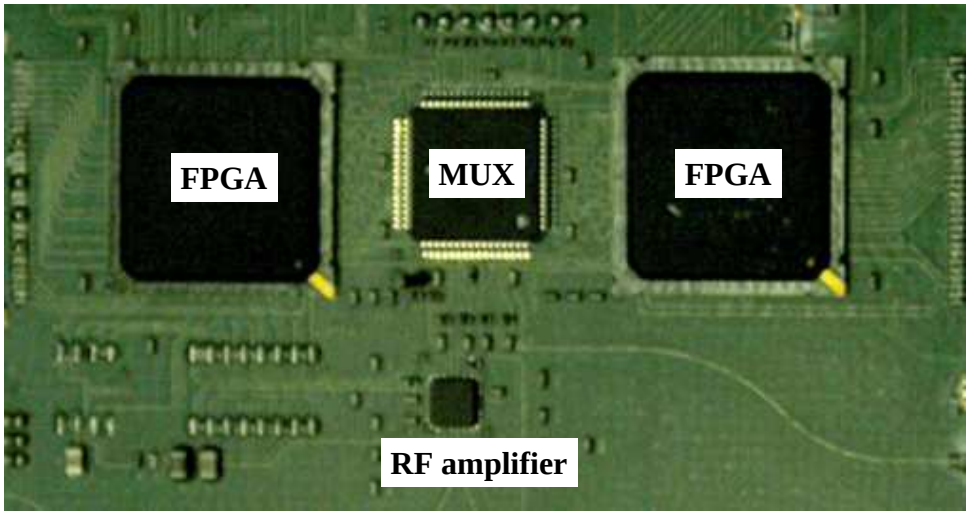

Figure 84: INC board from Packaging Research Center

5.5 Test Case 5: Fourteen-port power distribution network for INC board (Intelligent Network Communicator) from the Packaging Research Center

Figure 84 shows the INC(Intelligent Network Communicator) board developed at the Packaging Research Center. The board incorporates the digital, RF and optoelectronic sections on a 83.31mm x 65.4mm single test bed, which has two FPGA chips, a MUX and a RF amplifier.

The cross section of the board shown in Figure 85 has a signal layer and two plane layers. The first layer is the signal layer and the second and third layers are the irregularly shaped ground and power plane layers, respectively. The dielectric material with thickness of 60um has a dielectric constant, $\epsilon_r = 3.8$, and loss tangent, $tan\delta = 0.02$. The conductor in the three layers with thickness of 12um is copper with conductivity, $\sigma_c = 5.8 \times 10^7 S/m$.

The detailed layout of the three layers is shown in Figure 86. The 16 output ports of the two FPGA chips are connected to the input port of a MUX with a data

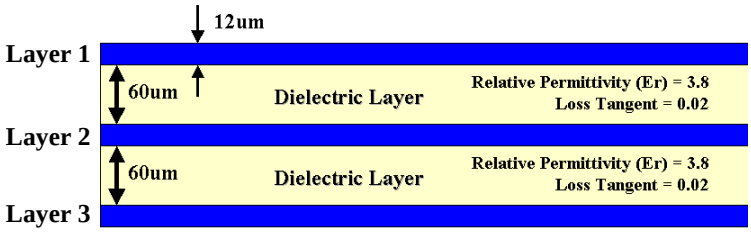

Figure 85: Cross section of the INC board

rate of 155Mbps/channel using 16 single ended transmission lines and the output of the MUX is connected to the input of the RF amplifier with a data rate of 2.4Gbps using a differential transmission line. The FPGA chips and RF amplifier are connected to a 3.3V dc source and the MUX is connected to a 2.5V dc source.

Fourteen port admittance parameters (uniformly distributed 1286 frequency samples from 10KHz to 9GHz per port) of the power plane pair were generated using the transmission matrix method (TMM) [50]. The location of ports depicted in Figure 86 is shown in Table 10. Using the methods discussed in Chapter 4, the macromodel was automatically constructed using BEMP version 3.0. The comparison of the magnitude in logarithm scale between the given frequency response and the response of the macromodel is shown in Figure 87, which shows good agreement between the input data and the macromodel. The frequency response shown in Figure 87 is the response of the bare board.

For design and analysis of the INC board, graduate student Prathap Muthana and Dr. Lixi Wan in the EPSILON group at Georgia Tech have modified the layout of the board to achieve maximum performance by adding decoupling capacitors and embedded capacitors based on the frequency response in Figure 87. The frequency response with the decoupling capacitors and/or embedded capacitors has been approximated by following the same procedure for the construction of the macromodel for the bare board. Then, time-domain simulation was performed in HSPICE using

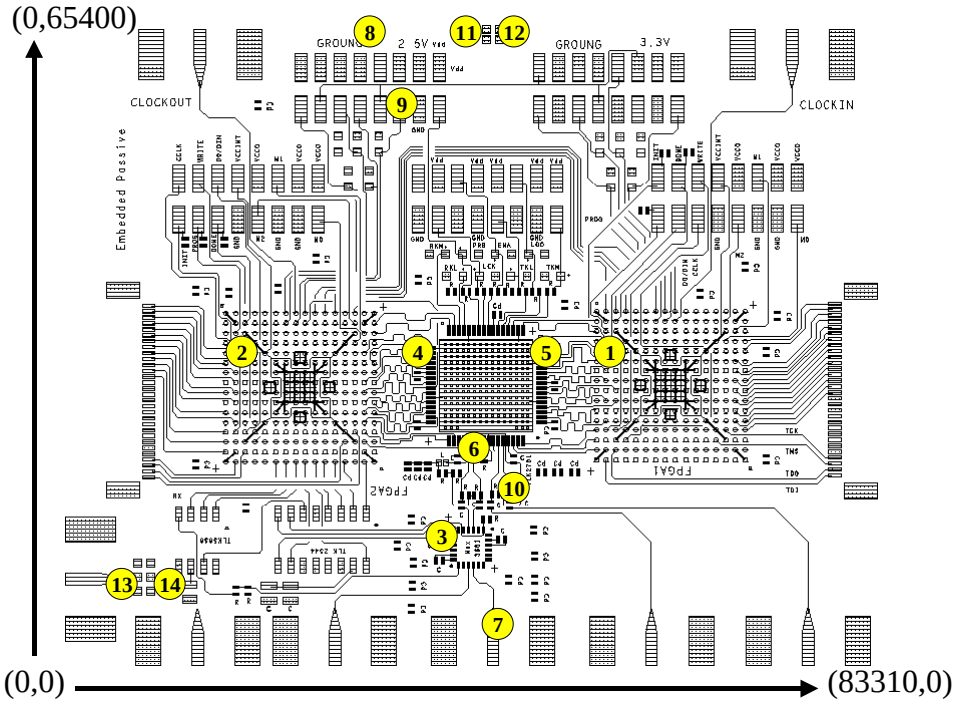

(a)

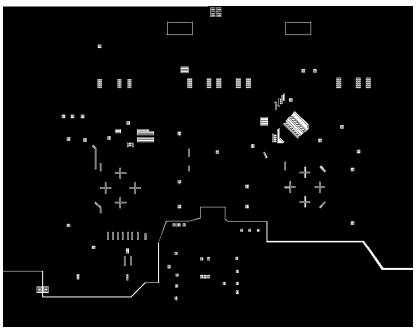

(b)

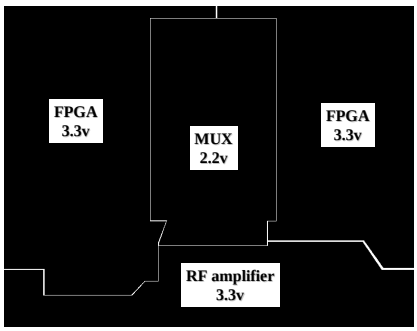

(c)

Figure 86: Layout of the layers (a) signal layer, (b) ground plane layer and (c) power plane layer

Table 10: Location of 14 ports

port	x(um)	y(um)
1	61080	28320
2	23740	28320
3	41140	12060
4	35810	28320
5	49650	28320
6	42290	21460
7	50000	1240
8	41300	64240
9	35900	60870
10	44191	19540
11	43090	64440
12	49610	64440
13	7600	8440
14	9300	8440

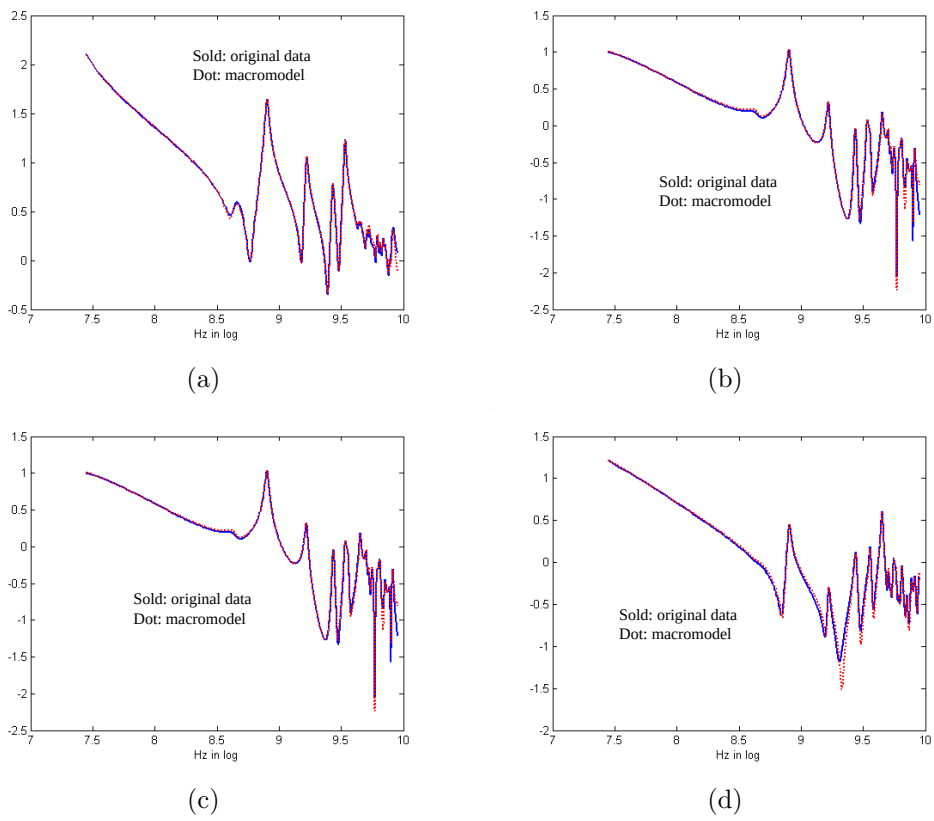

Figure 87: Comparison of admittance parameters: (a) magnitude of Y(1,1), (b) magnitude of Y(1,12), (c) magnitude of Y(12,1) and (d) magnitude of Y(12,12)

three sets of 14-port macromodels of the power planes for computing power supply noise, as shown in Figure 88. In Figure 88, the macromodel capturing the frequency response with the decoupling capacitors and embedded capacitors present provides the smallest noise fluctuation in the time-domain simulation.

5.6 Test Case 6: 32-bit bus from HRL

Figure 89(a) shows the interconnects (32-bit bus) on a Delta-Sigma modulator chip designed by HRL. The 32-bit bus shown in Figure 89(b) was modeled using an EM simulator that is proprietary to HRL. Therefore, only the frequency response of the bus was provided. Using this information, a macromodel of the 32-bit bus was developed. The comparison of the magnitude in logarithm scale between the given frequency response of the bus and the frequency response of the macromodel using BEMP version 3.0 is shown in Figure 90. This result in Figure 90 is for Y(1,19), which was screen-captured when BEMP version 3.0 was run on Windows. The deviation (RMS error) in Figure 90 shows the accuracy of the macromodel. For this test case, it is important to note that only diagonal elements were used for the approximation of 32-port admittance parameters. Hence, as compared to an original computation time of $C = O(K \times N^6) = O(K \times 1.0737 \times 10^9)$ in Section 4.8, where $N = 32$ and K is a constant, a computation time of $C = O(K \times N^3) = O(K \times 32768)$ was achieved, which resulted in a speed up of 32767.

The 32-port macromodel was connected to a 3.3V dc source having 100ps rise and 200ps fall times at port 1, as shown in Figure 91. Figure 92 show the time-domain waveform when all the ports were terminated with 30Ω resistors, which was used to simulate the crosstalk between ports 1 and 9.

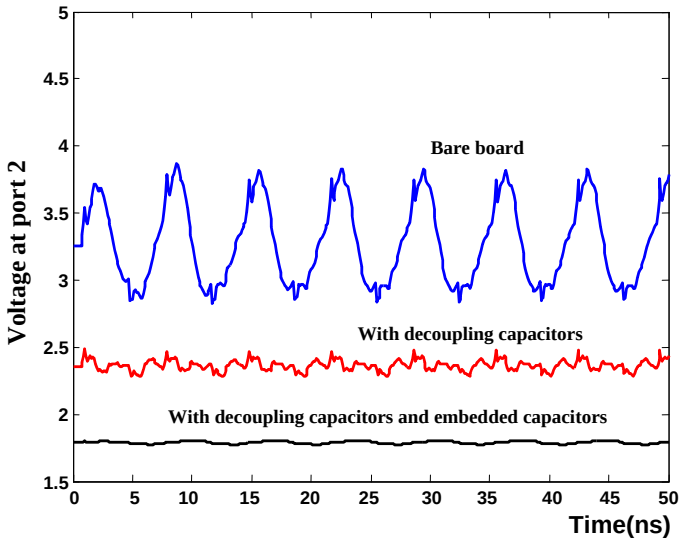

(a)

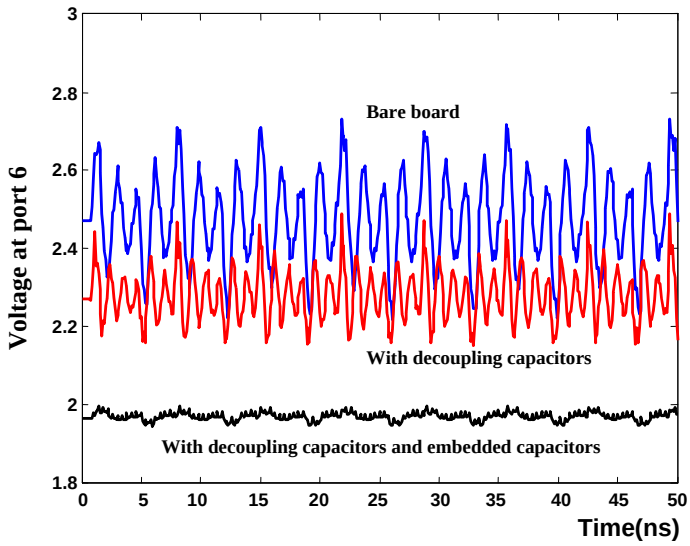

(b)

Figure 88: Time-domain simulation for evaluating the performance of the power distribution network with decoupling capacitors and embedded capacitors: (a) voltage at port 2 and (b) voltage at port 6

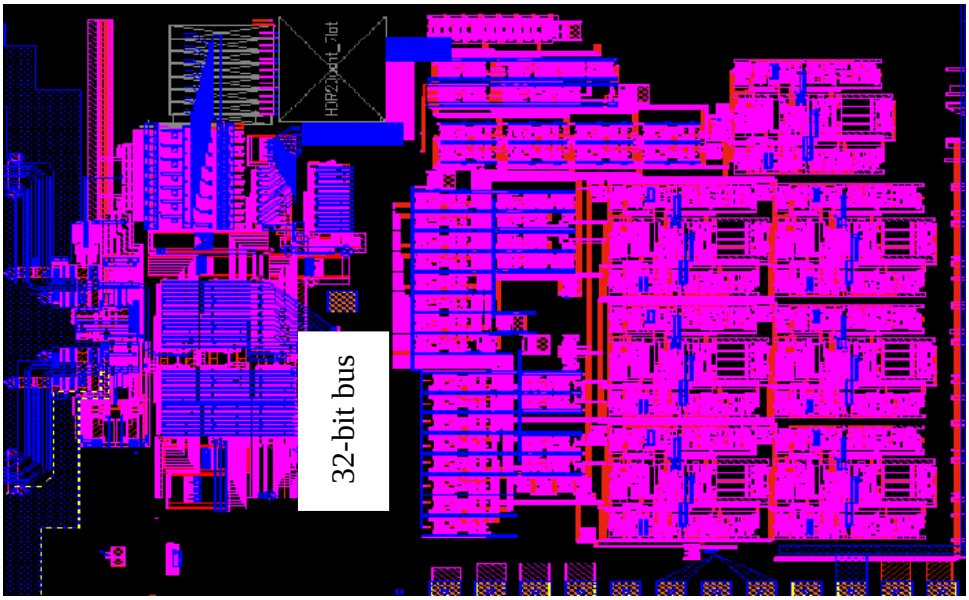

(a)

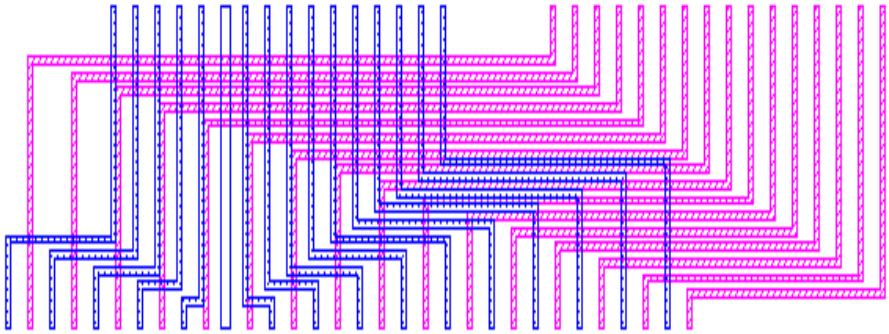

(b)

Figure 89: (a) Layout of Delta-Sigma modulator from HRL and (b) layout of 32-bit bus

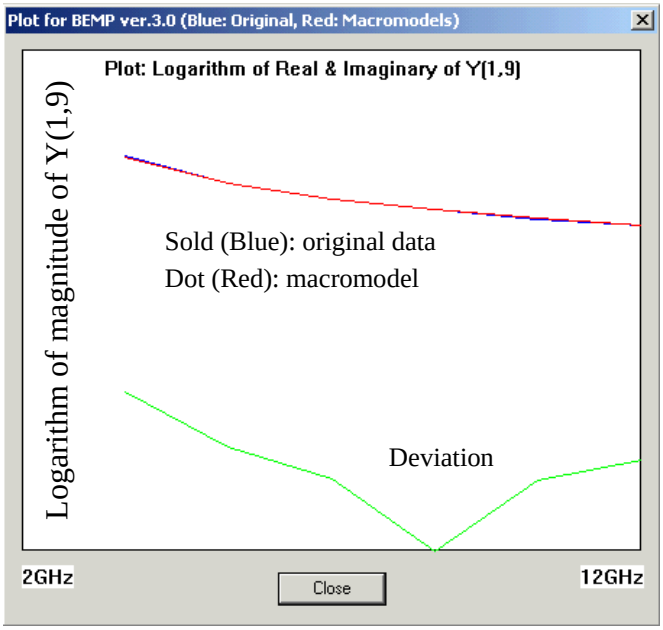

Figure 90: Comparison of admittance parameter Y(1,9)

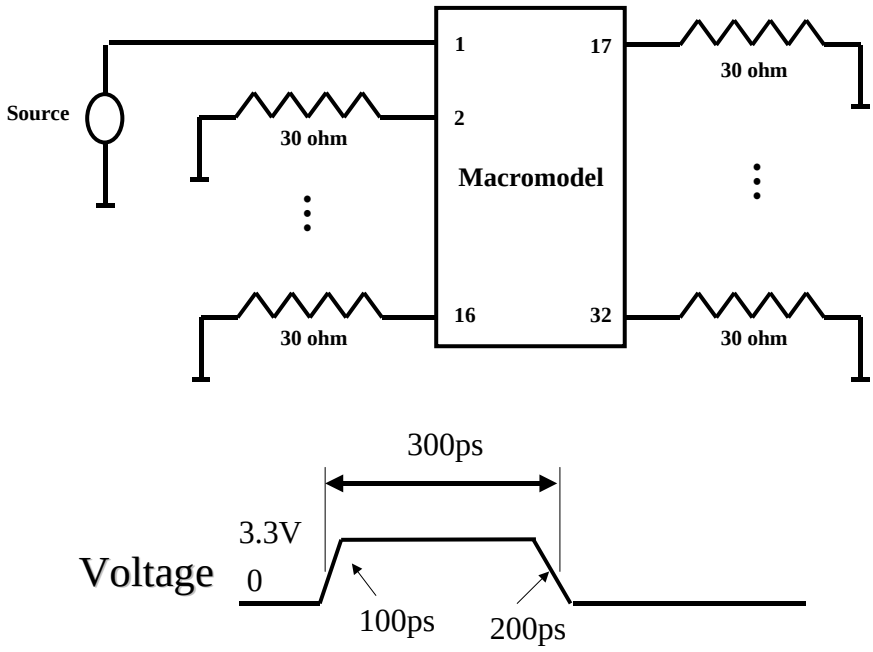

Figure 91: Circuit simulated

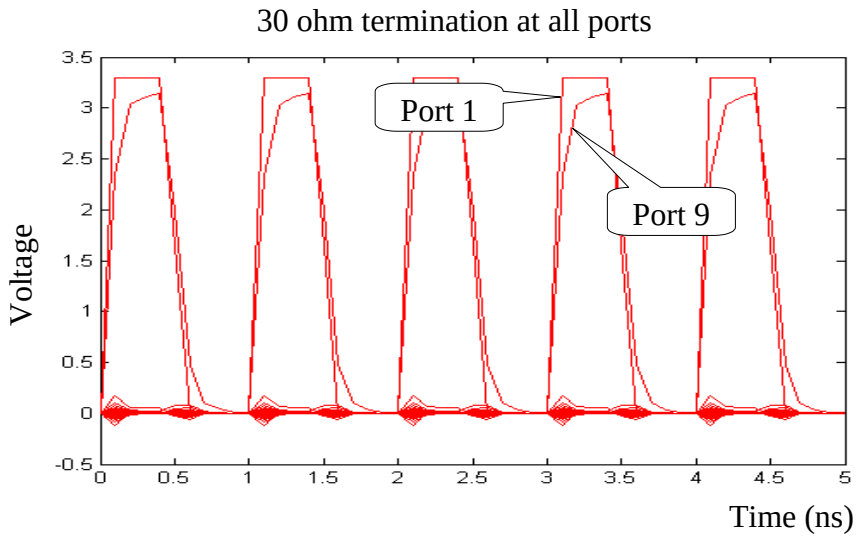

Figure 92: Crosstalk between ports 1 and 9

5.7 Summary

In this chapter, the Broadband Efficient Macromodeling Program, which implemented the methods in Chapter 4, was used for the construction of the broadband macromodel. Using BEMP, the efficiency of the methods developed was demonstrated through six test cases representative of distributed interconnect networks such as the lossy coupled transmission lines (simulation and measurement), a rectangular power plane with decoupling capacitors, realistic irregular power distribution networks and a 32-bit bus for gigabit data transmission.

CHAPTER VI

CONCLUSION AND FUTURE WORK

The goal of this dissertation was to construct macromodels from frequency data for simulation of distributed interconnect networks. Using the constructed macromodels, the electromagnetic behavior of distributed networks can be successfully integrated into circuit simulators for design and analysis of gigabit systems. In this dissertation, these macromodels have been categorized as scalable, passive and broadband macromodels. The scalable macromodels can be used to implement design libraries of passive devices; the passive macromodels can be used to integrate the black box representation of frequency responses into time-domain simulators; the broadband macromodels can be used to capture hundreds of resonant peaks over a broad frequency range.

Scalable macromodels for building design libraries of embedded passive devices have been constructed using multidimensional rational functions, orthogonal polynomials and selective sampling. The multidimensional rational functions were implemented as a multiplication of one-dimensional rational functions with frequency and design parameters to construct a mapping between the frequency response and physical parameters of the device. Orthogonal polynomials such as Legendre, Chebyshev I, and Chebyshev II polynomials were used in the multidimensional rational functions for increasing the accuracy of the macromodel. The selective sampling method reduced the number of frequency samples and increased the accuracy of the scalable macromodel. The performance of the above methods was demonstrated through the rectangular power plane structure with two design variations. Subsequently, the methods were successfully applied to build design libraries of embedded

spiral inductors in multilayer configurations.

Passive macromodels have been constructed using filter theory, the pole-residue form of the rational function, and multiport passivity formulae. The filter theory and pole-residue form of the rational function enabled any transfer function of a passive network to be represented as a summation of low pass, band pass, high pass and all pass filters. The relationship between the frequency response and coefficients of filters has been identified. The multiport passivity formulae using the maximum modulus theorem and Hurwitz test were derived for checking and enforcing passivity of the macromodel. The passivity formulae derived were sufficient but not a necessary condition. If the macromodel violated the multiport passivity formulae, negative eigenvalues in the residue matrix were set equal to zero or changed to a small positive value to ensure passivity of the macromodel and then the residue matrix was reconstructed. The passive macromodels were synthesized into equivalent circuit elements, which always had positive values due to the application of the passivity formulae derived.

Broadband macromodels have been constructed using the band division method, which divides the entire computational domain into sub-computational domains. The band division method alleviated the ill-conditioned matrix problem during least squares approximation and reduced the memory requirement. To solve the interaction problem between subbands arising when the band division method is used, methods such as selector, which selects the filters constructed from the subband of interest, subband reordering, which provides a construction sequence for reducing the interaction between subbands, subband dilation, which provides local correction in the boundary region between subbands, and pole replacement, which increases the accuracy of the broadband macromodel, have been developed.

During the construction of the macromodels, several issues have been solved

Version	Release Date	Details
BEMP 1.0	**Feb. 2002**	**• Generate transfer function-based model order reduction technique** **• Multiport passivity formulae (MPF) ➔Passive macromodels** **• Band division ➔ Broadband macromodels** **• Limited model accuracy in the low frequency band**
BEMP 2.0	**Oct. 2002**	**• Pole replacement method (DP) ➔ Improved macromodel accuracy** **• Successfully tested on digital and RF circuits (drivers, LNA, filters,…)** **• Improved model accuracy in the low frequency band**
BEMP 3.0	**Sep. 2003**	**• High pass macromodels ➔Ultra wideband macromodels** **• Improved model accuracy compared to that of Release 2.0 (Vector fitting)** **• Model order reduction (MOR) based on user's opinion** **• Automated construction of macromodels ➔Click and run** **• Successfully tested on multiport networks (32-bit bus, 14-port power planes,…)** **• Reduced amount of user interaction (GUI, touchstone file, MOR)**
BEMP 4.0	**June 2004**	**• Fast multiport construction of broadband macromodels** **• Scalable macromodels for building design libraries (orthogonal polynomials)** **• Delay extraction of distributed interconnects (model order reduction)**

Figure 93: Evolution of BEMP

using the properties of the rational function. Since each resonant peak in the frequency response can be represented as a filter, an automated construction method, which automatically determines the boundaries of each subband, has been developed by detecting the resonant peaks and nulls in the frequency response. Also, since off-diagonal elements are always a subset of the diagonal elements in the rational function matrix, the construction time of the multiport macromodel has been reduced by using diagonal elements in the common pole system. Using the property that the spurious filters can be detected by measuring the magnitude of resonant peaks, a method for reducing the order of the macromodel without affecting the stability and passivity conditions has been developed by removing the filters with negligible residue values.

These methods have been realized into the Broadband Efficient Macromodeling Program (BEMP) developed at Georgia Tech. The evolution of BEMP is shown in Figure 93.

Using BEMP, the efficiency of the methods developed in this dissertation was demonstrated through embedded passive devices and known transfer functions. The

methods have been successfully applied to test cases representative of distributed interconnect networks such as lossy coupled transmission lines, irregular power planes, and an on-chip bus.

As an extension to the methods described in this dissertation, the following research needs to be investigated:

Construction of causal macromodels: As described in this dissertation, the broadband macromodels capturing the frequency response of long transmission lines require hundreds of poles. Even if the macromodels accurately captured the frequency response of distributed circuits, small glitches prior to signal arrival have been observed, meaning that the macromodels violate the causality condition during time-domain simulation. Hence, delay and causality are important considerations especially for timing and false transitioning of circuits. Hence, macromodels need to be constructed after extracting the delay of the distributed interconnect network.

Construction of non-linear macromodels for I/O drivers: This dissertation is limited to the development of macromodels for capturing the behavior of passive networks. However, design and analysis of gigabit systems require not only a macromodel for capturing the behavior of passive devices but also a macromodel that captures the behavior of non-linear circuits for the simulation of accurate waveforms on interconnect networks. Hence, macromodels capturing the static and dynamic behavior of non-linear devices need to be investigated.

Construction of orthogonal macromodels for passive networks: In this dissertation, the macromodels have been constructed using filters. However, due to the non-orthogonality of filters, an interaction problem between subbands exists when the band division method is used. This interaction can be removed

if the basis functions of the macromodels are orthogonal in the frequency response. The basis functions can be wavelets or orthogonal polynomials.

Optimum order tracking method: As discussed in this dissertation, the minimum eigenvalue tracking method is limited to low order systems due to the ill-conditioned matrix problem. Hence, this dissertation alleviated the problem using the band division method, which decreases the required order of the macromodel. However, since the order of the macromodel sometimes resulted in the addition of spurious filters with negligible frequency response, it is important to develop an order tracking method for estimating the optimum order of the macromodel.

REFERENCES

[1] R. R. Tummala, *Foundations of Microsystems Packaging*, McGraw-Hill, 2001

[2] T. C. Edwards and M. B. Steer, *Foundations of Interconnect and Microstrip Design*, John Wiley & Sons, 3rd, 2000.

[3] R. Ho, K. W. Mai, and M. A. Horowitz, "The future of wires," *Proceedings of IEEE*, vol. 89, no. 4, April 2001.

[4] A. Deutsch et al., "On-chip wiring design challenges for gigahertz operation," *Proceedings of IEEE*, vol. 89, no. 4, April 2001.

[5] R. W. Keyes, "Fundamental limits of silicon technology," *Proceedings of IEEE*, vol. 89, no. 3, March 2001.

[6] D. J. Frank et al., "Device scaling limits of Si MOSFETs and their application dependencies," *Proceeding of IEEE*, vol. 89, no. 3, March 2001.

[7] J. D. Plummer, "Material and process limits in silicon VLSI technology," *Proceedings of IEEE*, vol. 89, no. 3, March 2001.

[8] D. Sylvester and K. Keutzer, "Impact of small process geometries on microarchitectures in systems on a chip," *Proceedings of IEEE*, vol. 89, no.4, April 2001.

[9] H. Johnson and M. Graham, *High-Speed Digital Design: A Handbook of Black Magic*, Prentice-Hall, 1993.

[10] B. Young, *Digital Signal Integrity: Modeling and Simulation with Interconnects and Packages*, Prentice-Hall, 2001.

[11] A. K. Goel, *High-Speed VLSI Interconnections*, John Wiley & Sons, 1994.

[12] S. G. Konsowski and A. R. Helland, *Electronic Packaging of High Speed Circuitry*, McGraw-Hill, 1997.

[13] V. Litovski and M. Zwolinski, *VLSI Circuit Simulation and Optimization*, Chapman & Hall, 1997.

[14] J. Ogrodzki, *Circuit Simulation Methods and Algorithms*, CRC Press, 1994.

[15] A. Loinvici, *Computer-Aided Analysis of Active Circuits*, Marcel Dekker, 1990.

[16] C. Ho, A. Ruehli, and P. Brennan, "The modified modal approach to network analysis," *IEEE Trans. Circuits System*, pp. 504, June 1975.

[17] A. F. Peterson, S. L. Ray, R. Mittra, *Computational Methods for Electromagnetics*, IEEE Press, 1998.

[18] A. E. Ruehli and A. C. Cangellaris, "Progress in the methodologies for the electrical modeling of interconnects and electronic packages," *Proceedings of the IEEE*, vol. 89, no. 5, May 2001.

[19] R. Achar and M. S. Nakhla, "Simulation of high-speed interconnects," *Proceedings of the IEEE*, vol. 89, no. 5, May 2001.

[20] A. Taflove and S. C. Hagness, *Computational Electrodynamics: The Finite-Difference Time-Domain Method*, Artech House, 2000.

[21] M. Sadiku, *Numerical Techniques in Electromagnetics*, CRC Press, 2001.

[22] A. E. Ruehli, "Equivalent circuit models for three dimensional multiconductor systems," *IEEE Trans. on Microwave Theory and Tech.,* pp. 216-221, March 1974.

[23] L. T. Pillage and R. A. Rohrer, "Asymptotic waveform evaluation for timing analysis," *IEEE Trans. Computer-Aided Design*, vol. 9, no. 4, pp. 352-366, April 1990.

[24] T. K. Tang and M. S. Nakhla, "Analysis of high-speed VLSI interconnects using the asymptotic waveform evaluation technique," *IEEE Trans. Computer-Aided Design*, vol. 11, no. 3, March 1992.

[25] J. E. Bracken, V. Raghavan, and R. A. Rohrer, "Interconnect simulation with asymptotic waveform evaluation (AWE)," *IEEE Trans. Circuits and Sys. I*, vol. 39, no. 11, Nov. 1992.

[26] D. F. Anastasakis, N. Gopal, S. Y. Kim, and L. T. Pillage, "Enhancing the stability of asymptotic waveform evaluation for digital interconnect circuit applications," *IEEE Trans. Computer-Aided Design*, vol. 13, no. 6, June 1994.

[27] E. Chiprout and M. S. Nakhla, "Analysis of interconnect networks using complex frequency hopping (CFH)," *IEEE Trans. Computer-Aided Design*, vol. 14, no. 2, Feb. 1995.

[28] P. Feldmann and R. W. Freund, "Efficient linear circuit analysis by Pade approximation via Lanczos process," *IEEE Trans. Computer-Aided Design*, vol. 14, no. 5, May 1995.

[29] K. J. Kerns and A. T. Yang, "Preservation of passivity during RLC network reduction via split congruence transformation," *IEEE Trans. Computer-Aided Design*, vol. 17, no. 7, July 1998.

[30] A. Odabasioglu, M. Celik, and L. T. Pileggi, "PRIMA: Passive reduced-order interconnect macromodeling program," *IEEE Trans. Computer-Aided Design*, vol. 17, no. 8, Aug. 1998.

[31] Q. Yu, J. Wang, and E. S. Kuh, "Passive multipoint moment matching model order reduction algorithm on multiport distributed interconnect networks," *IEEE Trans. Circuits and Sys. I*, vol. 46, no. 1, Jan. 1999.

[32] R. Achar, P. K. Gunupudi, M. Nakhla, and E. Chiprout, "Passive Interconnect reduction algorithm for distributed/measured networks," *IEEE Trans. Circuits and Sys. II*, vol. 47, no. 4, pp. 287-301, April 2000.

[33] D. B. Kuznetsov and J. E. Schutt-Aine, "Optimal transient simulation of transmission lines," *IEEE Trans. Circuits and Sys. I*, vol. 43, no. 2, Feb. 1996.

[34] W. T. Beyene and J. E. Schutt-Aine, "Accurate frequency-domain modeling and efficient circuit simulation of high-speed packaging interconnects," *IEEE Trans. Microwave Theory and Tech.*, vol. 45, no. 10, Oct. 1997.

[35] W. T. Beyene and J. E. Schutt-Aine, "Efficient transient simulation of high-speed interconnects characterized by sampled data," *IEEE Trans. Components, Packaging, and Manufacturing Tech.*, vol. 21, no. 1, Feb. 1998.

[36] K. L. Choi and M. Swaminathan, "Development of model libraries for embedded passives using network synthesis," *IEEE Trans. on Analog and Digital Signal Processing*, vol. 47, no. 4, April 2000.

[37] M. Elzinga, K. L. Virga, and John L. Prince, "Improved global rational approximation macromodeling algorithm for networks characterized by frequency-sampled data," *IEEE Trans. Microwave Theory and Tech.*, vol. 48, no. 9, Sep. 2000.

[38] W. T. Beyene, "Improving time-domain measurements with a network analyzer using a robust rational interpolation technique," *IEEE Trans. Microwave Theory and Tech.*, vol. 49, no. 3, pp. 500-508, March 2001.

[39] S. Chakravorty, S. H. Min, and M. Swaminathan, "Comparison between Chebyshev and power series expansion for interpolating data," *IEEE 10th Topical Meeting on Electrical Performance of Electronic Packaging*, pp. 153-156, Oct. 2001.

[40] S. H. Min and M. Swaminathan, "Efficient construction of two-port passive macromodels for resonant networks," *IEEE 10th Topical Meeting on Electrical Performance of Electronic Packaging*, pp. 229-232, Oct. 2001.

[41] S. H. Min and M. Swaminathan, "Construction of broadband passive macromodels from frequency data for simulation of interconnect networks," *IEEE EMC-Zurich*, Feb. 2003.

[42] B. Gustavsen and A. Semlyen, "Simulation of transmission line transients using vector fitting and modal decomposition," *IEEE Trans. Power Delivery*, vol. 13, no. 2, April 1998.

[43] B. Gustavsen and A. Semlyen, "Combined phase and modal domain calculation of transmission line transients based on vector fitting," *IEEE Trans. Power Delivery*, vol. 13, no. 2, April 1998.

[44] B. Gustavsen and A. Semlyen, "Application of vector fitting to state equation representation of transformers for simulation of electromagnetic transients," *IEEE Trans. Power Delivery*, vol. 13, no. 3, July 1998.

[45] B. Gustavsen and A. Semlyen, "Rational approximation of frequency domain responses by vector fitting," *IEEE Trans. Power Delivery*, vol. 14, no. 3, July 1999.

[46] B. Gustavsen and A. Semlyen, "Enforcing passivity for admittance matrices approximated by rational functions," *IEEE Trans. Power Systems*, vol. 16, no. 1, pp. 97-104, Feb. 2001.

[47] D. Saraswat, R. Achar, and M. Naklar, "A fast algorithm and practical considerations for passive macromodeling of measured/simulated data," *IEEE 11th Topical Meeting on Electrical Performance of Electronic Packaging*, Oct. 2002.

[48] K. L. Choi, *Modeling and Simulation of Embedded Passives Using Rational functions in Multi-layered Substrates*, Ph.D. Thesis, Georgia Institute of Technology, Aug. 1999.

[49] N. Na, *Modeling and Simulation of Planes in Electronic Packaging*, Ph.D. Thesis, Georgia Institute of Technology, Jan. 2001.

[50] J. Kim, *Modeling of Package and Board Power Distribution Networks Using Transmission Matrix and Macro-modeling Methods*, Ph.D. Thesis, Georgia Institute of Technology, Sep. 2002.

[51] M. J. Choi and A. C. Cangellaris, "A quasi three-dimensional distributed electromagnetic model for complex power distribution networks," *IEEE 51st ECTC*, pp. 1111-1116, May 2001.

[52] P. Pieters, K. Vaesen, S. Brebels, S. F. Mahmoud, W. D. Raedt, E. Beyne, and R. P. Mertens, "Accurate modeling of high-Q spiral inductors in thin-film multilayer technology for wireless telecommunication applications," *IEEE Trans. Microwave Theory and Tech.*, vol. 49, no. 4, April 2001.

[53] I. J. Bahl, "High-performance inductors," *IEEE Trans. Microwave Theory and Tech.*, vol. 49, no. 4, April 2001.

[54] S. F. Peik, R. R. Mansour, and Y. L. Chow, "Multidimensional Cauchy method and adaptive sampling for an accurate microwave circuit modeling," *IEEE Trans. Microwave Theory and Tech.*, vol. 46, no. 12, Dec. 1998.

[55] S. H. Min, S. Dalmia, and M. Swaminathan, "Development of scalable models for embedded passive devices using selective sampling," *IEEE Workshop on Signal Propagation on Interconnects-Italy*, May 2001.

[56] S. H. Min, S. H. Lee, W. Kim, S. Dalmia, M. Swaminathan, F. Liu, and R. R. Tummala, "Design, fabrication, measurement, and modeling of embedded inductors in laminate technology," *IEEE InterPACK2001*, July 2001.

[57] S. Dalmia, S. H. Min, and M. Swaminathan, "Modeling RF passive circuits using coupled lines and scalable models," *IEEE Electronic Components and Technology Conference*, pp. 816-823, June 2001.

[58] S. H. Lee, S. H. Min, D. S. Kim, S. Dalmia, W. Kim, V. Sundaram, S. Bhattacharya, G. White, R. R. Tummala, M. Swaminathan, F. Ayazi, and J. S. Kenney, "High performance spiral inductors embedded on organic substrate for SOP applications," *IEEE MTT-S*, pp. 2229-2232, Aug. 2002.

[59] F. F. Kuo, *Network Analysis and Synthesis*, John Wiley & Sons, 1962.

[60] S. Kami, *Network Theory: Analysis and Synthesis*, Allyn and Bacon, 1966.

[61] Star-HSPICE Manual, Release 1999.2, June 1999.

[62] SONNET, Release 8.53.

[63] HP-ADS, Release 2002.

[64] P. Borwein and T. Erdelyi, *Polynomials and Polynomial Inequalities*, Springer-Verlag, 1995.

[65] G. Arfken, *Mathematical methods for physicists*, Harcout / Academic Press, pp. 500, pp. 521, pp.646, pp. 724, pp. 733, 1985.

[66] G. H. Golub and C. F. Van Loan, *Matrix Computation*, Baltimore, MD: The Johns Hopkins Press, 1996.

[67] R. N. Bracewell, *The Fourier Transform and Its Applications*, McGraw-Hill, Inc., pp. 17, 1986.

[68] W. H. Press, S. A. Teukolsky, W. T. Vetterling, and B. P. Flannery, *Numerical Recipes in C: The Art of Scientific Computing*, 2nd Ed. Oxford, U.K.: Cambridge Univ. Press, 1992.

[69] S. Grivet-Talocia, "Enforcing passivity of macromodels via spectral perturbation of Hamiltonian matrices," *IEEE SPI*, May 2003.

[70] B. Mutnury, M. Swaminathan, and J. Libous, "Macro-Modeling of Non-Linear I/O Drivers using Spline Functions and Finite Time Difference Approximation", *IEEE 12th Topical Meeting on Electrical Performance of Electronic Packaging*, Oct. 2003.

[71] J. Choi, S. H. Min, J. Kim, M. Swaminathan, W. Beyene, and C. Yuan, "Modeling and Analysis of Power Distribution Networks for Gigabit Applications", *IEEE Trans. Mobile Computing*, vol. 2, no. 4, pp. 299-313, Oct.-Dec. 2003.

PUBLICATIONS GENERATED

1. **S. H. Min** and M. Swaminathan, "Construction of broadband passive macromodels from frequency data for simulation of distributed interconnect networks," accepted for publication of *IEEE Trans. on Electromagnetic Compatibility*, 2004.

2. **S. H. Min** and M. Swaminathan, "Construction of broadband passive macromodels from frequency data for simulation of interconnect networks," *IEEE Electromagnetic Compatibility-Zurich*, Feb. 2003.

3. J. Choi, **S. H. Min**, J. Kim, M. Swaminathan, W. Beyene, and C. Yuan, "Modeling and Analysis of Power Distribution Networks for Gigabit Applications", *IEEE Trans. Mobile Computing*, vol. 2, no. 4, pp. 299-313, Oct.-Dec. 2003.

4. J. Choi, **S. H. Min**, S. Dalmia, M. Swaminathan, J. Kim, W. Beyene, and C. Yuan, "Efficient hybrid methodology for analyzing power distribution networks in high-speed systems," *Progress in Electromagnetics Research Symposium*, Oct. 2003.

5. W. Kim, **S. H. Min**, S. Choi, and M. Swaminathan, "Measurement-based modeling and test methodology for integrated substrates," *IEEE Automated RF Techniques Group*, pp. 29-38, Dec. 2002.

6. J. Kim, J. Choi, J. Choi, S. Chun, **S. H. Min**, W. Kim, and M. Swaminathan, "Electromagnetic modeling and hardware measurements of simulations of switching noise in high speed systems," *Proceedings of the International Symposium on EMC*, vol. 2, pp. 748-754, Aug. 2002.

7. **S. H. Min** and M. Swaminathan, "Efficient construction of two-port passive macromodels for resonant networks," *IEEE 10th Topical Meeting on Electrical Performance of Electronic Packaging*, pp. 229-232, Oct. 2001.

8. **S. H. Min**, S. Dalmia, and M. Swaminathan, "Development of scalable models for embedded passive devices using selective sampling," *IEEE Workshop on Signal Propagation on Interconnects*, May 2001.

9. S. Chakravorty, **S. H. Min**, and M. Swaminathan, "Comparison between Chebyshev and power series expansion for interpolating data," *IEEE 10th Topical Meeting on Electrical Performance of Electronic Packaging*, pp. 153-156, Oct. 2001.

10. S. H. Lee, **S. H. Min**, D. S. Kim, S. Dalmia, W. Kim, V. Sundaram, S. Bhattacharya, G. White, R. R. Tummala, M. Swaminathan, F. Ayazi, and J. S. Kenney, "High performance spiral inductors embedded on organic substrate for SOP applications," *IEEE MTT-S*, pp. 2229-2232, Aug. 2002.

11. S. Dalmia, F. Ayazi, M. Swaminathan, **S. H. Min**, S. H. Lee, W. Kim, D. Kim, S. Bhattacharya, V. Sundaram, G. White, and R. R. Tummala, "Design of inductors in organic substrates for 1-3GHz wireless applications," *IEEE MTT-S*, pp. 1405-1408, June 2002.

12. **S. H. Min**, S. H. Lee, W. Kim, S. Dalmia, M. Swaminathan, F. Liu, and R. R. Tummala, "Design, fabrication, measurement, and modeling of embedded inductors in laminate technology," *IEEE InterPACK*, July 2001.

13. S. Dalmia, S. H. Lee, V. Sundaram, **S. H. Min**, M. Swaminathan, and R. R. Tummala, "CPW high Q inductors on organic substrates," *IEEE 10th Topical Meeting on Electrical Performance of Electronic Packaging*, pp. 105-108, Oct. 2001.

14. S. Dalmia, **S. H. Min**, and M. Swaminathan, "Modeling RF passive circuits using coupled lines and scalable models," *IEEE Electronic Components and Technology Conference*, pp. 816-823, June 2001.

15. S. Dalmia, **S. H. Min**, S. H. Lee, V. Sundaram, and M. Swaminathan, "Design and optimization of embedded RF filters using a hybrid approach," *IEEE Radio & Wireless Conference*, pp. 145-148, Aug. 2001.

16. S. Dalmia, W. Kim, **S. H. Min**, M. Swaminathan, V. Sundaram, F. Liu, G. White, and R. R. Tummala, "Design of embedded high Q-inductors in MCM-L Technology," *IEEE MTT-S*, pp. 1735-1738, May 2001.

AWARDS / PATENTS

1. 1st Place, Poster Contest, Annual NSF-PRC meeting, Georgia Tech, 1999.

2. 2st Place, Poster Contest, Annual NSF-PRC meeting, Georgia Tech, 2003.

3. **S. H. Min** and M. Swaminathan, "Efficient construction of passive macromodels for resonant networks," U.S. Patent Application Number 20030088394 on May 8, 2003.

4. S. Dalmia, **S. H. Min**, S. H. Lee, V. Sundaram, F. Ayazi, G. White, M. Swaminathan, and W. Kim, "Organic substrate having integrated passive components," U.S. Patent Application Number 20020158305 on Oct. 31, 2002.

VITA

Sung-Hwan Min was born in Pohang, Korea on September 27, 1970. He received the B.S. degree in electronic engineering in 1996 from Hanyang University, Ansan, Korea, the M.S. degree in electrical and computer engineering in 2001 and the Ph.D. degree in 2004 from Georgia Institute of Technology, Atlanta, Georgia.

To pursue his Ph.D. in electrical and computer engineering, he began his research with Professor Madhavan Swaminathan in 1999 as a Graduate Research Assistant in Packaging Research Center, Georgia Institute of Technology. In the summer of 2000, he interned at Cadence, Chemsford. His major research topic supported by Yamacraw, Georgia and NEOCAD, DARPA was in the area of modeling and simulation of embedded passive devices and distributed interconnect networks using macromodels. He has contributed to several publications and software in the macromodeling area. His current research interests are in the area of design and modeling of active and passive devices in gigahertz mixed signal systems.